Ⅲ-2

Materials Sciences

Highlight

BL7U

Electronic Structure of $Sr_{1-x}Ca_xFe_2(As_{1-x}P_x)_2$ Revealed by Angle Resolved Photoemission Spectroscopy II

T. Adachi[1], S. Ideta[2, 3], K. Tanaka[2, 3], T. Z. How[1], S. Miyasaka[1] and S. Tajima[1]

[1]*Department of Physics, Graduate school of Science, Osaka University, Toyonaka 560-0043, Japan*

[2]*UVSOR Synchrotron Facility, Institute for Molecular Science, Okazaki 444-8585, Japan*

[3]*School of Physical Sciences, The Graduate University for Advanced Studies (SOKENDAI), Okazaki 444-8585, Japan*

It is well known that there is a remarkable correlation between a crystal structure and T_c in iron based superconductor. Thus, it is essential for unraveling the superconducting (SC) mechanism in this system to clarify how the electronic structure (the topology of a Fermi surface (FS) and the SC gap structure) changes with the crystal structure. Recently we have performed ARPES measurements on $Sr_{1-x}Ca_xFe_2(As_{1-y}P_y)_2$ (x = 0.25, y = 0.08) whose c/a (the ratio of a- and c-axes lattice constants), which is index of structural anisotropy, is smaller than that of $BaFe_2(As_{1-y}P_y)_2$. We have revealed two salient features of this compound. First, the innermost d_{xy} hole band is below E_F around the Γ point, while in $BaFe_2(As_{1-y}P_y)_2$, all the hole bands are above E_F in the entire k_z region [1]. Second, there is a gap minimum on one of the electron FS.

In this measurement, we have performed the ARPES measurement on $Sr_{1-x}Ca_xFe_2(As_{1-y}P_y)_2$ (x = 0.25, y = 0.08) to confirm the gap minimum on one of the electron FSs and clarify the momentum dependences of the SC gaps around all the high symmetry points. Figure 1 shows the SC gaps on the electron FSs around the X point. One can see the gap minimum around 40 degrees on the δ electron FS in Fig. 1 (a). This feature has been confirmed by measurements for other 4 samples summarized in Fig. 1 (c). Therefore, we conclude that there exists the gap minimum on the δ electron FS, indicating the existence of a node. All results about the SC gaps are summarized in Fig. 2. There is weak anisotropy of the SC gap on the γ hole FS around the Z point, implying the contribution of the spin fluctuation to the SC mechanism [2]. On the other hand, other gaps on the hole FSs are nearly isotropic. As discussed above, there exist the gap minima or nodes on the δ electron FS while the SC gap on the ε electron FS is almost isotropic. This result indicates the orbital fluctuation plays an important role on the SC mechanism [3].

[1] T. Yoshida, I. Nishi, S. Ideta, A. Fujimori, M. Kubota, K. Ono, S. Kasahara, T. Shibauchi, T. Terashima, Y. Matsuda, H. Ikeda and R. Arita, Phys. Rev. Lett. **106** (2011) 117001.

[2] K. Suzuki, H. Usui and K. Kuroki, J. Phys. Soc. Jpn **80** (2011) 013710.

[3] T. Saito, S. Onari and H. Kontani, Phys. Rev. B **88** (2013) 045115.

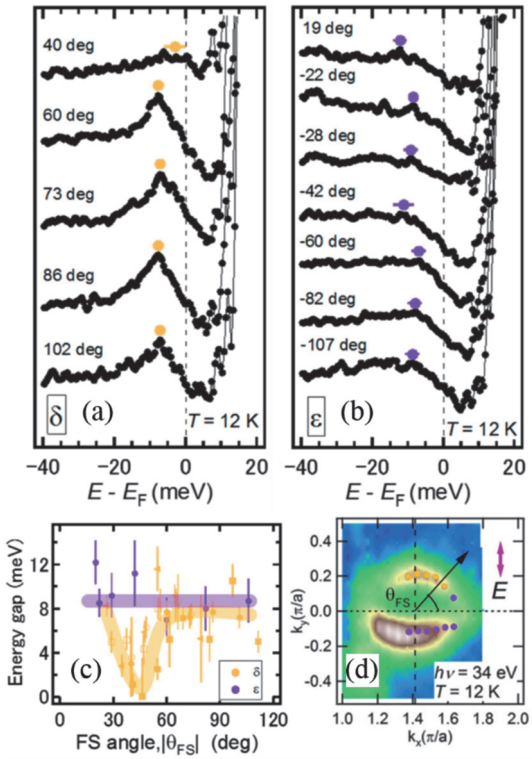

Fig. 1. (a), (b) The photoemission spectra divided by Fermi-Dirac function at various Fermi surface angles θ_{FS} for electron FSs. (c) Energy gap as a function of θ_{FS}. (d) In-plane FS mapping around the X point.

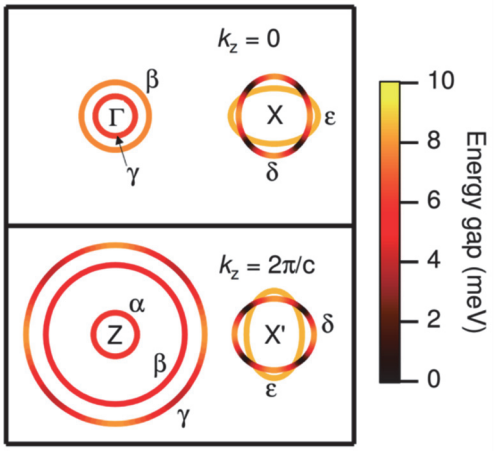

Fig. 2. Color plots of the SC gap distribution on the FSs of $Sr_{1-x}Ca_xFe_2(As_{1-y}P_y)_2$ (x = 0.25, y = 0.08).

BL1B

Terahertz Spectroscopy of Ionic Liquids

T. Awano
Faculty of Engineering, Tohoku Gakuin University, Tagajo 985-8537, Japan

Terahertz absorption bands had been observed in superionic conductors of crystals and glasses[1]. These bands seems to be due to collective motion of conductive ions, although the correlational dynamics of mobile ions is not clear.

Ionic liquid (IL) is molten salt at room temperature because of large radius of component ions. Figure 1 shows molecular structures of 1-Ethyl-3-methylimidazolium [C_2min] cation and bis (trifluoro-methyl) sulfonyl imide [Tf_2N] anion. It is interesting to compare ionic motion in ionic liquids with those in superionic conductor for investigation of dynamics of mobile ions. In superionic conducting glasses, only cation is mobile.

Temperature dependence of absorption spectra of ionic liquids in spectral range between 20 to 60 cm^{-1} have measured to investigate change of dynamics of mobile ions. Transmittance spectra of one and two filter papers with the ionic liquid of the same quantity per the paper were measured. Absorption spectra were obtained by subtracting each other. To eliminate interference fringe remaining in the spectra, absorption difference spectra of each spectrum from that at 78 K are shown in Fig. 2. Molecular dynamics (MD) simulation was excuted using GROMACS5.0.

There observed some structures in the absorption spectra in terahertz region contrary to the previously reported THz-TDS result[2]. Temperature dependence of the absorption spectra showed similar tendency as the results in millimeter wave region [3]. Four types of the spectral change occurred at temperature above melting point or glass transition temperature. The intensities of the absorption bands in the ILs which are crystal in the solid state showed rapid decrease at their melting points. On the other hand, those in ILs which are vitreous in the solid state weakened and shifted gradually. Some others showed complicated change. The other type showed no absorption band in this spectral range.

Figure 3 shows MD simulation spectra of each ion in [C_2min] [Tf_2N] at 300 K. Terahertz absorption bands are coincident with those in observed spectra in Fig. 2.

Figure 4 shows contribution of rotation of molecules (a) and temperature dependence of that of the anion (b). A part of the observed spectral change seems to be due to the rotation of ions.

[1] T. Awano and T. Takahashi, J. Phys. Soc. Jpn. **79** (2010) Suppl. A 118.
[2] T. Yamada, Y. Tominari, A. Tanaka and M. Mizuno, J. Phys. Chem. B **119** (2015) 15696.
[3] T. Awano and T. Takahashi, KURRI rep. 2016.

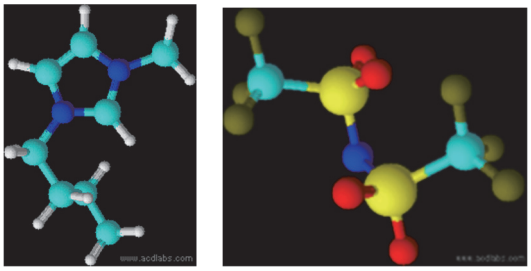

(a) (b).

Fig. 1. Ionic structures of [C_2min] (a) and [Tf_2N]

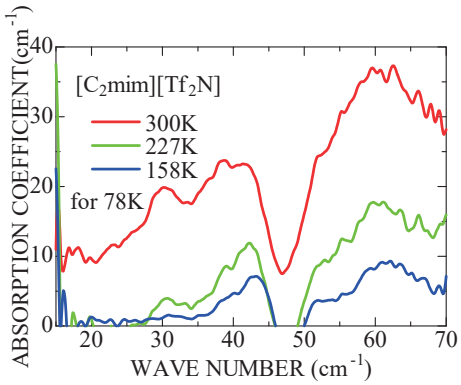

Fig 2. Absorption increment spectra of [C_2min] [Tf_2N] against the absorption spectrum at 78 K.

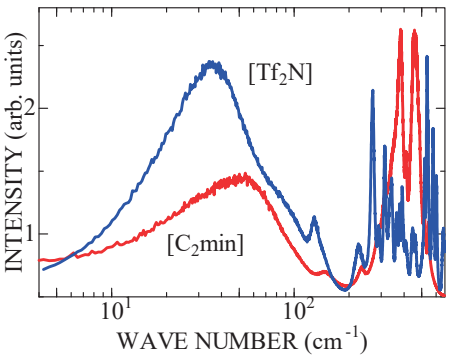

Fig. 3. Autocorrelation function of velocity of ions in [C_2min] [Tf_2N] at 300 K.

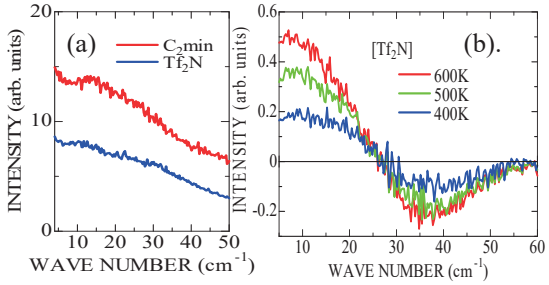

Fig. 4. (a) Rotational velocity autocorrelation function of the cation and anion at 300 K. (b) Increment spectra of anion against that at 300 K.

BL2A

XAFS Measurement for Alloying Element in Tempered Nitrogen Martensite

M. Sato and S. Shimaya
Institute for Materials Reseach, Tohoku University, Sendai 980-8577, Japan

It is well known that the martensite phase obtained by quenching is hard but brittle. Therefore the balance between hardness and toughness is adjusted by the subsequent tempering treatment. At that time, cementite is precipitated in case carbon steel, and Fe_4N is precipitated in case of nitrogen steel [1, 2].

Although it is known that alloying elements partially dissolve as solid solution in these precipitates, there is a little knowledge on the chemical state of these substitution elements in the precipitates. In this study, changes in the chemical state of the substitutional elements such as Si and Mo before and after tempering treatment were investigated by XAFS measurement.

Fe-1mass%Si and Fe-1mass%Mo alloys were used as starting materials. They were homogenized at 1523 K for 24h and furnace-cooled until room temperature. The Fe-1Si alloys were prepared by nitriding and quenching (N-Q) process using NH_3/H_2 mixed gas at 1273 K for 1 h. Then obtained Fe-1Si-0.3N alloys were tempered at 773 K. and precipitates generated during tempering were extracted using Iodine-alcohol procedure. The Si K-edge XANES spectra were corrected by fluorescence method using InSb double crystal monochrometer and silicon drift detector (SDD) at BL2A in UVSOR, respectively. Obtained data were analyzed using Athena software.

Figure 1 shows Si K-edge XANES spectra of Fe-1Si-0.3N samples before and after tempering. The XANES spectrum of the as-quenched sample showed similar spectrum to that previously reported. the spectrum shape changed at tempering above 400°C, and the peak at 1840 eV decreased and that at 1845 and 1850 eV increased. These peaks at 1845 and 1850 eV are the same as the peak positions obtained from Si_3N_4 and SiO_2 reference samples [3]. Therefore, it is thought that Si kept a solid solution state in Fe at low tempering temperature below 300°C and it precipitated as Si_3N_4 or made a solid solution in Fe_4N precipitates at the tempering temperature above 400 °C. In addition, it is considered that the component of SiO_2 is the oxidation of the surface.

XANES spectra of Mo alloy slightly changed by tempering only at 500°C, implying the precipitation of Mo compounds, or it made a solid solution in Fe_4N precipitates. In the future, detailed examination should be carried out by analysis of the EXAFS region and calculation using FEFF code.

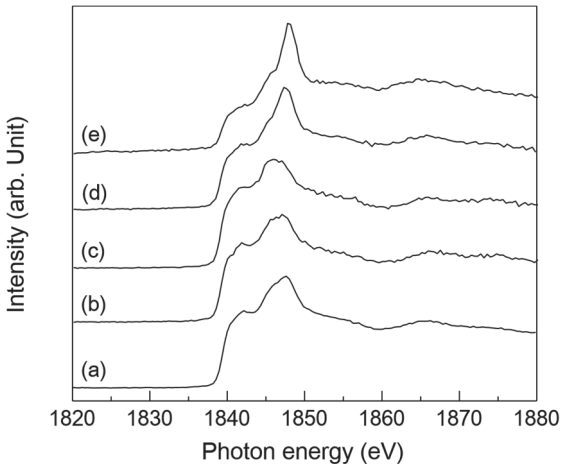

Fig. 1. Si K-edge XANES spectra of Fe-1Si-0.3N samples. (a) as-quenched sample and tempered at (b) 100°C (c) 200°C (d) 400°C and (e) 500°C for 1 hour.

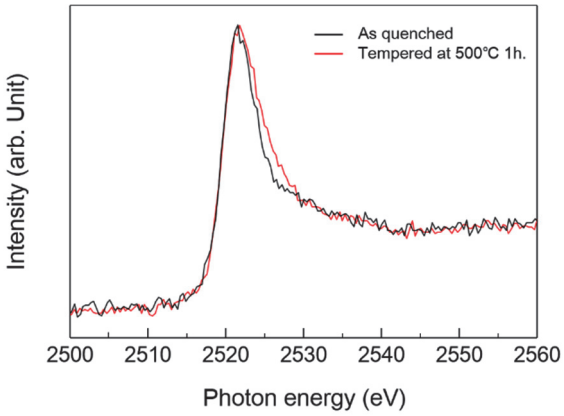

Fig. 2. Mo L-edge XANES spectra of Fe-1Mo-0.3N samples. (a) as-quenched and (b) tempered at 500 °C for 1 hour.

[1] L. Cheng and E. J. Mittemeijer, Met. Trans. A **21A** (1990) 13.
[2] L. Cheng, A. Bottger and E. J. Mittemeijer, Met. Trans. A **23A** (1992) 1129.
[3] M. Sato, UVSOR Activity Report **44** (2016).

BL2A

Catalytically Active Mo_2C Species on H-MFI Zeolites for Methane Dehydroaromatization with Hydrogen

H. Aritani[1], R. Yamazaki[2], M. Tsutsumi[1], H. Miyanaga[1], M. Akutsu[2], S. Mogi[2], K. Ogasawara[2], K. Kuramochi[2] and A. Nakahira[3]

[1]*Graduate School of Engineering, Saitama Institute of Technology, Fukaya 369-0293, Japan*
[2]*Advanced Science Research Laboratory, Saitama Institute of Technology, Fukaya 369-0293, Japan*
[3]*Graduate School of Engineering, Osaka Prefecture University, Sakai 599-8531, Japan*

MoO_3-modified H-MFI (Mo/H-MFI) is a noted typical catalyst for methane dehydroaromatization, which is an important reaction for direct GTL (Gas To Liquid) processes. Since detail of the MTB reaction process is still unknown, It has been accepted that the activity is based on strong acidity and sieving effects onto MFI zeolite support. During the reaction, MoO_x species must be reduced and carbonized to form carbide-like species[1]. At the same time, catalytic deactivation is brought about by carbon contamination on MFI. The deactivation strongly depends on the strong acidity on H-MFI, and excess carbonization Mo species also affect the lowering of methane conversion. In our previous study, Mo/GaAl-MFI (using Ga-contained H-MFI) catalysts employed to MTB reaction[2]. In these cases, formation of Mo-carbide species with durable MTB activity is different from those of Mo/H-MFI catalysts. Since H_2 co-feed with CH_4 reactant is effective for suppression of carbon coking on H-MFI, reduction of active Mo species can proceeds. It is concluded that formation of active Mo carbide-like species, as well as restraint of the carbon deposits on H-MFI supports, may become the breakthrough for the design of high and durable MTB catalysts[3]. In the present report, Mo L_{III}-edge XANES study is applied to characterize the Mo/H-MFI catalysts to evaluate the Mo species after the MTB reaction with H_2.

Catalysts were prepared by impregnation of H-MFI support with $MoO_2(acac)_2$–$CHCl_3$ solution (5.0wt% as MoO_3) , and followed by drying overnight and calcination at 773 K for 3 h. H-MFI supports (SiO_2/Al_2O_3 ratio is 27 or 40) were synthesized hydrothermally at 413 K for a week, and followed by ion-exchanging with NH4Cl and calcination at 873 K. The catalytic activity of MTB was evaluated by means of fixed bed flow reaction, as described in a separate paper[1]. The reactant gas is CH_4(20%)+H_2 (0-3%)+He(base) at the flow rate of 30 mL/min, and the reactivity was evaluated at 1023 K by using the 0.25 g of each Mo/H-MFI catalyst. Mo L_{III}-edge XANES spectra were obtained in BL2A of UVSOR-IMS in a total-electron yield mode using InSb double-crystal monochromator. Photon energy was calibrated by using Mo metal-foil at Mo L_{III}-edge, and normalized XANES spectra are presented by using REX-2000 (Rigaku) software.

Figure 1 shows the XANES spectra of Mo/H-MFI after MTB reaction with H_2. In case of the H-MFI (Si/Al_2=28) support, it is definitely that metallic Mo species are formed after the reaction with/without H_2. These catalysts shows durable reactivity, and thus, excess reduction to form the metallic Mo species act as the highly reactive sites. For the H-MFI (Si/Al_2=40) support, reduction of Mo species are slightly and almost as similar as α-Mo_2C. On these catalysts, suppressing effect for deactivation was shown by addition of H_2. However, highly reduced Mo ions are not formed on H-MFI (Si/Al_2=40) support. The relation between the reduction of Mo species and the catalytic activity and its durability for MTB is now in progress.

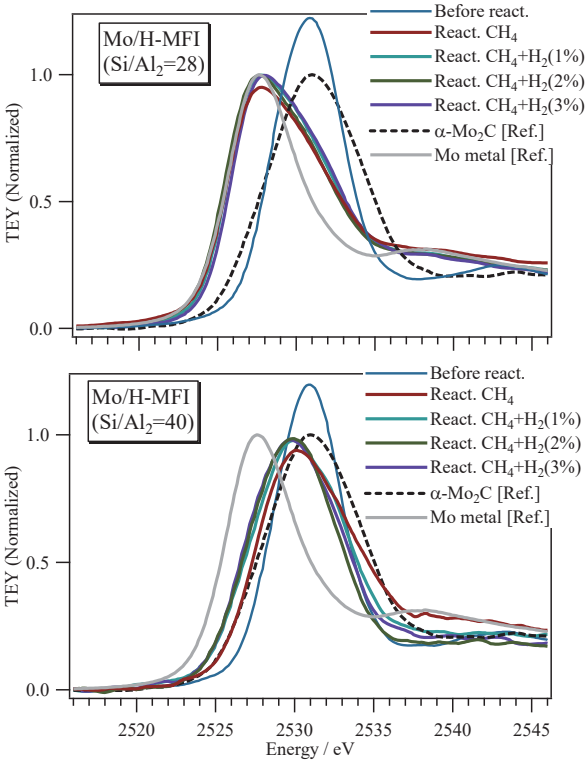

Fig. 1. Mo L_{III}-edge XANES over Mo/H-MFI [Si/Al_2 ratios are 28 (top) and 40 (bottom)] catalysts after the MTB reaction with H_2.

[1] H. Aritani *et al.*, J. Environm. Sci. **21** (2009) 736.
[2] H. Aritani *et al.*, UVSOR Activity Report, **43** (2016) 49.
[3] H. Aritani *et al.*, UVSOR Activity Report, **44** (2017) 52.

BL2A

Mg K-edge XANES of MgO Single Crystal

K. K. Okudaira[1], S. Yoshioka [2] and E. Kobayashi[3]

[1] *Graduate School of Science and Engineering, Chiba University, Chiba 263-8522, Japan*
[2] *Gradiate School of Engineering, Kyushu University, Fukuoka 819-0395, Japan*
[3] *Kyushu Synchrotron Light Research Center, Tosu 841-0005, Japan*

A large number of applications have lead to the study of magnesium oxide in recent years. In the field of organic electronics, magunesium oxides (MgOs) are used as encaplation, high-k substrate, and insulating material deposited between the organic layer and the metal cathode for organic light emitting diode (OLED), organic thin film transistor (OTFT), and organic photovoltaic solar cell (OPV), respectively[1-3]. Particularly, MgOs are used as insulating barriers and play an essential role in state of the organic devices. In this context the electronic structure MgO has been widely studied. Furthermore, MgO single crystal has attracted attentiondue to its simple electronic structure, giving rise to a series of very interesting basic physics questions. In general, to obtain the information on electronic strucuture of valence band and conduction band, UPS and XANES or IPES are used, respectiveity [4]. The photoelectron spectroscopy such as UPS and XANES using electron yield method are not available due to low conductivity (high insulation) of MgO single crystal.

In this report, we investigated the electronic structure of MgO single crystal by means of XANES using fluorescence yield method.

Mg *K*-edge XANES measurements were performed at the BL2A of UVSOR Okazaki, Japan, using the partial fluorescence yield method (PFY). A $KTiOPO_4$ (KTP) double crystal monochromator defined Mg *K* absorption edges in the energy region from 1290 to 1340 eV. The samples were set with their surface perpendicular to the incident X-ray beam. Fluorescence X-rays of Mg *K*α were collected using an energy dispersible silicon drift detector (SDD). All measurements of XANES spectra were carried out in vacuum of 1×10^{-5} Pa at room temperature. To interpret the local structure from the experimental spectra, we used theoretical spectra by the full-potential linearized augmented plane wave (APW) plus local orbitals technique as implemented in WIEN2k code[5].

Firstly, magnesium oxide (MgO), which is typical insulating material for electronic devices, was measured. Fine structures of Mg *K*-edge XANES were observed in MgO, as shown in Fig. 1. Theoretical spectra of rock salt-type MgO was performed with 216 atoms supercell. The calculation of MgO successfully reproduced the major peaks (a, b, c and d) and shoulders of the experimental spectrum with respect to relative energy and intensity. In XANES experiments with fluorescence mode for highly concentrated sample, the peak intensities sometime do not be observed correctly due to thickness effect. However, the degree of distortion in MgO spectrum in this study was improved by devising the sample-detector arrangements. We will study the interaction between MgO and organic molecules by this method.

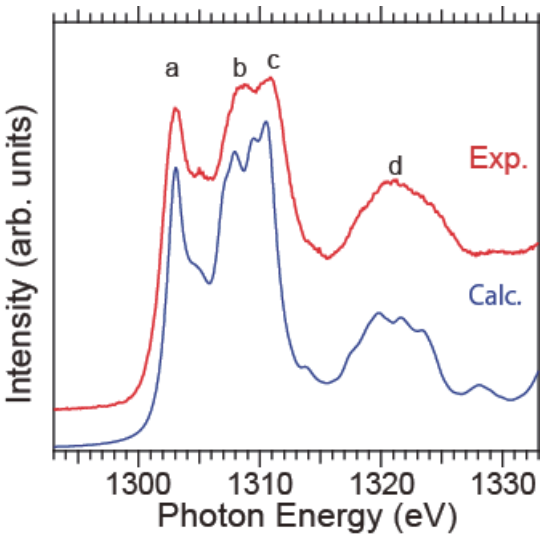

Fig. 1. Mg *K*-edge XANES spectra of MgO. Experimental (red) and calculated (blue) spectrum.

[1] Y. C. Han, C. Jang, K. J. Kim, K. C. Choi, K. H. Jung, B. –S. Bae, Org. Electron **12** (2011) 609.
[2]1 S.-S. Cheng, C.-Y. Yang, C.-W. Ou, Y.-C. Chuang, M.-C. Wu, and C.-W. Chu, Electrochem. Solid State Lett. **11** (2008) H118.
[3] 1 D.-H. Kim, J.-H. Kim, Y.-H. Hwang, J.-W. Shin, and J.-G. Park, J. Korean Phys. Soc. **3** (2013) 490.
[4] NEXAFS J Stöhr Springer-Verlag Berlin 1992.
[5] P. Blaha, K. Schwarz, G.K.H. Madsen, D. Kvasnicka, and J. Luitz, WIEN2K: An Augmented Plane Wave plus Local Orbitals Program for Calculating Crystal Properties (Vienna: Vienna University of Technology, 2001).

BL2A

Structural Evaluation and Synthesis of Various Hydroxyapatite Doped with Al Ion

A. Nakahira[1], M. Togo[1], M. Sato[2], T. Ujike[1], T. Sakuma[1], T. Moriya[1], M. Minami[1] and H. Aritani[3]

[1] *Faculty of Engineering, Osaka Prefecture University, Sakai 599-8531, Japan*
[2] *Industrial Materials Research (IMR), Tohoku University, Sendai 980-8577, Japan*
[3] *Saitama Institute of Technology, Fukaya 369-0293, Japan*

Hydroxyapatite, $Ca_{10}(PO_4)_6(OH)_2$, similar to the inorganic components of bone and teeth, is one of most attractive bioceramics (calcium phosphate) for implants and replacements in orthopedics fields. At the same time hydroxyapatite possesses the excellent biologically active properties and the high biocompatibility. It is well-known that natural bones have higher osteoconductive activities, because these natural bones contain generally some cations in the hydroxyapatite structure. However, the biocompatibility strongly depends on the nature and amount cation. Especially, it is inexplicit on the behaviors of aluminum ion for biocompatibility and osteoconductive activities.

The purpose in this study was to evaluate the local structure of aluminum ion for hydroxyapatite added with aluminum ion synthesized by the solution-precipitation method such as static hydrothermal process. The effect of aluminum ion amount on the microstructure for various hydroxyapatite added with aluminum ion was specially investigated.

All chemicals were analytical reagent-grade, and they used without further purification. Undoped and Al-doped hydroxyapatite samples were synthesized using the static hydrothermal process as a solution-precipitation method. Starting aqueous solutions were 0.1 mol/L solutions with $Ca(NO_3)_2{\cdot}4H_2O$, $Al(NO_3)_3{\cdot}6H_2O$ and $(NH_4)_2HPO_4$. Precipitations were matured at 353 K for 5 hours in air atmosphere and subsequently synthesized at 423 K for 12h to 24h by the static hydrothermal process. Nominal Al/(Ca+Al) ratio was set to 0, 1, 3, 5 and 10 at%. The samples prepared through this process were characterized with X-ray diffraction technique. The microstructures were observed by SEM.

Al-*K* XANES was measured at BL2A in UVSOR. The pellets of samples were mounted on carbon tapes. The incident X-ray beam was monochromatized with using beryl double crystals. Al-*K* XANES signals were collected with GaAsP photo-diodes (Hamamatsu: G-1127-02).

Theoretical spectra were obtained by the first-principles supercell method with a core-hole effect and evaluated for a detailed analysis of Al-*K* XANES.

According to the XRD results, all samples were identified to hydroxyapatite structure without another phase. In especial, aluminium phosphate and calcium phosphate were not contained for Al-doped hydroxyapatite samples synthesized using the static hydrothermal process.

Figure 1 shows the results of Al-*K* XANES spectra of various Al-doped hydroxyapatite samples synthesized using the static hydrothermal process. As shown in Fig. 1, Al-*K* XANES spectra of sample obtained by hydrothermal process were quite similar. Furthermore, Al-doped hydroxyapatite samples with the high contents of aluminum ion were most of the same as ones with low content of aluminum ion. As a result, Al-doped hydroxyapatite samples with Al/(Ca+Al) ratio of 1, 3, 5 and 10 had the similar Al local structure.

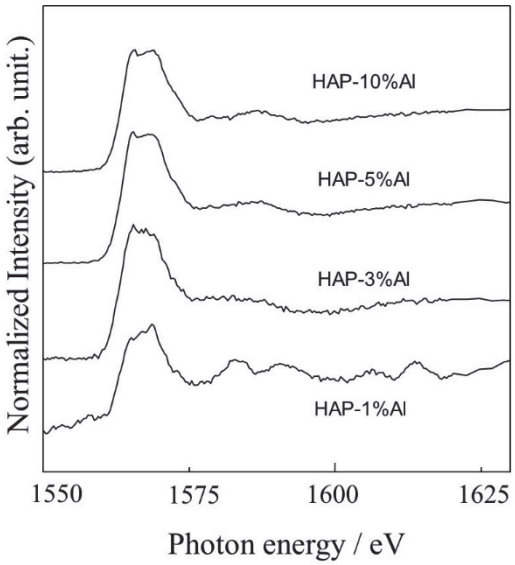

Fig. 1. Al-*K* XANES spectra of various products synthesized by the hydrothermal process at 423 K.Al-doped hydroxyapatite samples: Al/(Ca+Al) ratio of 1, 3, 5 and 10.

BL2A

Change in Charge States of Mo Ions in Sr_2FeMoO_6 by Incorporations of Ba and Nb Ions

S. Obunai[1] and T. Yamamoto[1, 2]

[1]*Faculty of Science and Engineering, Waseda University, Tokyo 169-8555, Japan*
[2]*Institute of Condensed-Matter Science, , Waseda University, Tokyo 169-8555, Japan*

The half-metallic materials have been widely studied due to their potential applications in new technologies such as spintronics. Sr_2FeMoO_6 is the promising candidates of half-metals, since it has high Curie temperature (420 K) and colossal magnetoresistance (CMR) at room temperature [1]. It was studied that the partial replacements of Sr and Mo by Ba and Ta, respectively, change magnetic property. There are two aspects to understand such change in magnetic property, that is 1) change in magnetic moments on Fe and Mo and 2) change in magnetic ordering. In order to investigate the first one 1), valence states of magnetic ions should be determined. For such purpose, XANES analysis is quite powerful. In the current study, we have investigated the change in valence states of Mo ions in Sr_2FeMoO_6 by incorporations of Ba and Nb ions using the Mo-L XANES measurements.

$Sr_{2-x}Ba_xFeMoO_6$ and $Sr_2FeMo_{1-x}Ta_xO_6$, were synthesized by the conventional solid state reaction method changing the cation ratio, x. $SrCO_3$, $BaCO_3$, a-Fe_2O_3, MoO_3 powders were used for the starting materials. Crystal structures of all the synthesized materials were examined by the powder X-ray diffraction with Cu-Kα X-rays.

XANES measurements at Mo-L_3 of the samples here synthesized were carried out at BL2A in UVSOR with a total electron yield method. All the sample powders were put on the carbon adhesive tape, which were attached onto the Al plate, and the drain current was measured instead of counting the number of emitted electrons from the samples. The InSb double-crystal monochromator was employed.

Observed Mo-L_3 XANES spectra of Ba incorporated Sr_2FeMoO_6, i.e., $Sr_{2-x}Ba_xFeMoO_6$, are shown in Fig. 1. The component in lower energy side decrease as increase of Ba concentration when x is 0.5 and 1.0, and at x = 1.5 that of higher energy side decreases. Finally, lower energy side recovers with no change in higher energy side as that at x = 1.5. From this analysis, we can discuss change in magnetic moment derived from Mo ions. Same analysis have been also carried out for $Sr_2FeMo_{1-x}Ta_xO_6$, whose spectra are shown in Fig. 2. In both cases, i.e., $Sr_{2-x}Ba_xFeMoO_6$ and $Sr_2FeMo_{1-x}Ta_xO_6$, it was found that simple peak shift without spectral change does not occur due to the Ba and Ta incorporations. The first principles calculations within a density functional theory were also carried out to investigate the change in charge states of Mo ions due to the incorporations of Ba and Nb ions, which support the experimental change in the spectral shapes.

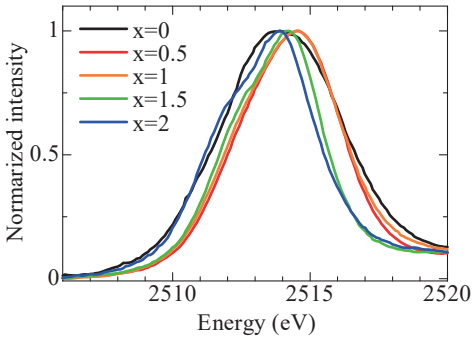

Fig. 1. Mo-L_3 XANES spectra of $Sr_{2-x}Ba_xFeMoO_6$.

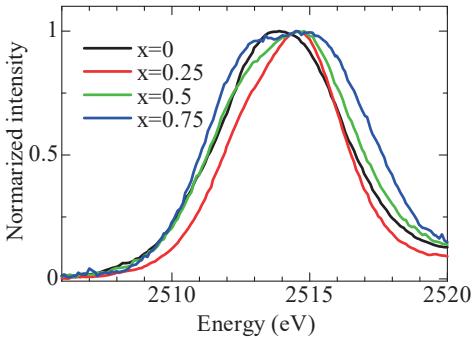

Fig. 2. Mo-L_3 XANES spectra of $Sr_2FeMo_{1-x}Nb_xO_6$.

[1] K. –I. Kobayashi *et al*., Nature **395** (1998) 677.

BL2A

Study of Local Structure of Al-K Edge for Novel Modified Layered Double Hydroxide by Rehydration Process

A. Nakahira[1], M. Iida[1], M. Togo[1], M. Sato[2] and H. Aritani[3]

[1]*Faculty of Engineering, Osaka Prefecture University, Sakai 599-8531, Japan*

[2]*Industrial Materials Research (IMR), Tohoku University, Sendai 980-8577, Japan*

[3]*Saitama Institute of Technology, Fukaya 369-0293, Japan*

Layered double hydroxide (LDH) is one of unique clay minerals with a layered structure and possess the excellent exchangeable anions ability owing to substitution to various cations and anions in LDH. Its composition formula is $[M(II)1\text{-}x\ M(III)x(OH)_2]x+\cdot[An\text{-}x/n\cdot YH_2O]$. M(II), M(III) for layered double hydroxide. Here, we focus on the structure evaluation of novel modified NiAl-LDH synthesized from MgAl-LDH composed of Al^{3+} and Mg^{2+}, which is called hydrotalcite. In special, it was found that in our experiments the rehydration treatment for MgAl-LDH samples heat-treated at 473 K to 773 K in air atmosphere resulted in the synthesis of novel modified NiAl-LDH. The purpose in this study was to evaluate the local structure of aluminum ion for novel modified NiAl-LDH synthesized by the rehydration treatment for MgAl-LDH in aqueous nickel acetate solution. The effect of concentration of aqueous nickel acetate solution on the microstructure for novel modified NiAl-LDH through the rehydration treatment was specially investigated.

Mixing solution was adjusted by mixing 0.2 mol/dm^3 $MgCl_2$ aqueous solution and 0.1 mol/dm^3 $AlCl_3$ aqueous solution. MgAl-LDH with M^{2+}/M^{3+} =2 were synthesized by adding mixing solution into 0.05 mol/dm3 $NaHCO_3$ at room temperature through the co-precipitation process. 1 mol/dm^3 NaOH was simultaneously added into the aqueous solution in order to keep pH 10. After precipitation was finished, the products for MgAl-LDH were aged at room temperature for 2 hours. They were separated from liquid phase with Buchner funnel and sufficiently washed by deionized water and finally air-dried at 323 K for 24 hours. Mixed oxides (Mg-Al double oxide) were prepared by calcination at 473 K to 773 K in air atmosphere for 2 hours of MgAl-LDH. The rehydration treatment for mixed oxides (Mg-Al double oxide) was carried out in aqueous nickel acetate solution with 0.1 M to 0.5 M at room temperature. The samples prepared through this process were characterized with X-ray diffraction technique. The microstructures were observed by SEM. The local structures around Al were characterized by measuring X-ray adsorption near edge structure (XANES) at BL01A in UV-SOR with KTP. Al-*K* XANES was measured at BL2A in UVSOR. The pellets of samples were mounted on carbon tapes. The incident X-ray beam was monochromatized with using KTP crystals. Al-*K* XANES signals were collected with GaAsP photo-diodes (Hamamatsu: G-1127-02). Theoretical spectra were obtained by the first-principles supercell method with a core-hole effect and evaluated for a detailed analysis of Al-*K* XANES.

XRD results indicated that MgAl-LDH samples prepared by the co-precipitation process were identified to hydrotalcite structure without another phase. After calcination at 573 K to 773 K in air atmosphere for 2 hours of MgAl-LDH, samples were identified to amorphous mixed oxides (Mg-Al double oxide), not hydrotalcite structure. Using these amorphous mixed oxides, the rehydration in aqueous nickel acetate solution was attempted to synthesize the modified NiAl-LDH. According to XRD, samples after the rehydration in aqueous nickel acetate solution were identified to hydrotalcite structure and modified NiAl-LDH was successfully obtained by the rehydration in aqueous nickel acetate solution. Figure 1 shows the results of Al-*K* XANES spectra for modified NiAl-LDH synthesized by the rehydration process. As shown in Fig. 1, Al-*K* XANES spectra of sample obtained by rehydration process were quite similar aluminum hydroxide. As a result, NiAl-LDH prepared by rehydration process the same structure as the coprecipitation process.

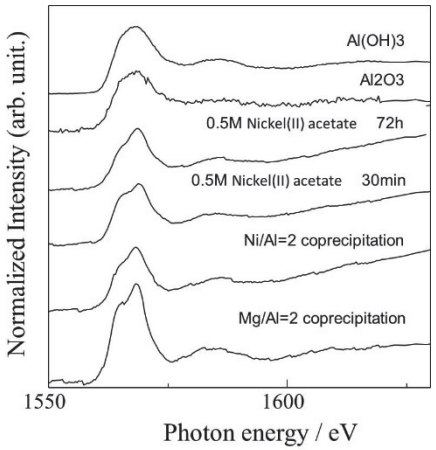

Fig. 1. Al-*K* XANES spectra of various products.

BL2A

Local Structure Investigations of $Gd_3Ga_5O_{12}$ Irradiated with Swift Heavy Ions

S. Yoshioka[1], K. K. Okudaira[2] and E. Kobayashi[3]

[1] *Gradiate School of Engineering, Kyushu University, Fukuoka 819-0395, Japan*
[2] *Graduate School of Science and Engineering, Chiba University, Chiba 263-8522, Japan*
[3] *Kyushu Synchrotron Light Research Center, Tosu 841-0005, Japan*

Gadolinium gallium garnet ($Gd_3Ga_5O_{12}$ or GGG) is considered as an important material for laser optical application. Ion irradiations are currently used to tailor materials properties. In particular, for garnet structure materials, swift heavy ion irradiations, produce amorphous tracks that can change the microstructure and the magnetic or magneto-optical properties. In the present study, we made a combined study of NEXAFS measurements and first principles calculations on $Gd_3Ga_5O_{12}$ with special interests on the local environment of Ga and Gd after irradiated with swift heavy ions.

Synthetic single crystals of $Gd_3Ga_5O_{12}$ were used in this study. The crystals were cut into sheets with a (111) plane surface and were polished to a mirror finish. The specimens were irradiated with 200 MeV Xe ions to fluences of 1×10^{13} cm^{-2} at the H1 beamline of the tandem ion accelerator facility at the Japan Atomic Energy Agency (JAEA) in Tokai. Ga L_3-edge XANES measurements were performed at the BL2A beamline of UVSOR Okazaki, Japan, using the partial fluorescence yield method (PFY). A Beryl double crystal monochromator defined Ga L_3 absorption edges in the energy region from 1105 to 1160 eV. The samples were set with their surface perpendicular to the incident X-ray beam. Fluorescence X-rays of Ga $L\alpha$ were collected using an energy dispersible silicon drift detector (SDD). All measurements of XANES spectra were carried out in vacuum of 1×10^{-5} Pa at room temperature. To interpret the local structure from the experimental spectra, we used theoretical spectra by the full-potential linearized augmented plane wave (APW) plus local orbitals technique as implemented in WIEN2k code[1].

Figure 1 shows calculated Ga L_3-edge XANES spectrum of monoclinic type gallium oxide (β-Ga_2O_3) as standard samples together with experimental spectra. Theoretical spectrum was performed with 120 atoms supercell. The calculation of Ga_2O_3 successfully reproduced the major peaks and shoulders of the experimental spectrum with respect to relative energy and intensity. Detailed analyses on the local environment of $Gd_3Ga_5O_{12}$ irradiated with swift heavy ions are in progress by combined use of the NEXAFS and the first principles band structure calculations.

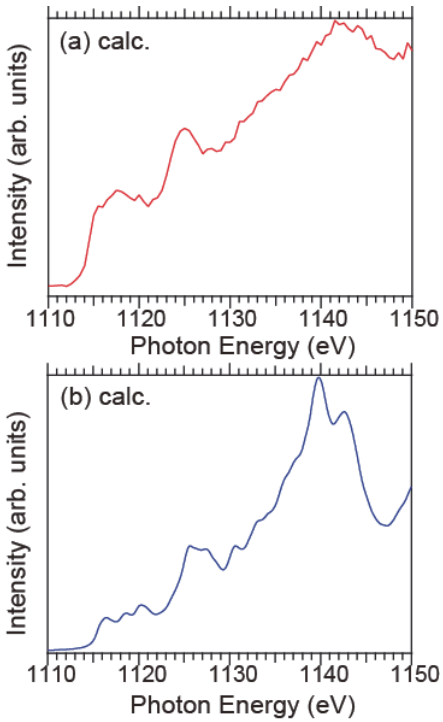

Fig. 1. Ga L_3-edge XANES spectra of Ga_2O_3. Experimental (a) and calculated (b) spectra.

[1] P. Blaha, *et al.*, WIEN2k, *An Augmented Plane Wave + Local Orbitals Program for Calculating Crystal Properties* (Karlheinz Schwarz, Techn. Universität Wien, Austria, 2001).

BL2B

Ultraviolet Photoelectron Spectroscopy Reveals Small Intermolecular Band Dispersion in an Acceptor-donor Blend

N. Aghdassi[1], Q. Wang[1, 2], R.-R. Ji[1], B. Wang[1], J. Fan[1] and S. Duhm[1]

[1]*Institute of Functional Nano & Soft Materials (FUNSOM), Soochow University, Suzhou 215123, P. R. China*

[2]*Institut für Angewandte Physik, Universität Tübingen, 72076 Tübingen, Germany*

7,8,15,16-tetraazaterrylene (TAT) thin films grown on highly oriented pyrolytic graphite (HOPG) substrates were studied by means of ultraviolet photoelectron spectroscopy (UPS). Photon energy-dependent UPS performed perpendicular to the molecular planes of TAT multilayer films at room temperature clearly reveals band-like intermolecular dispersion of the TAT highest occupied molecular orbital (HOMO) energy. Based on a comparison with a tight-binding (TB) model, a relatively narrow bandwidth of 54 meV is derived. Upon additional deposition of 2,2':5',2":5",2"'-quaterthiophene (4T), a 4T/TAT donor-acceptor blend is formed. The 4T/TAT blend likewise exhibits intermolecular dispersion of the TAT HOMO energy, yet with a significant decreased bandwidth.

Photon energy-dependent UPS measurements of TAT thin films were carried out at BL2B of UVSOR III in a UHV chamber with a base pressure of 1×10^{-8} mbar at normal electron emission and at room temperature (300 K). Energy calibration of the spectra was enabled by separately recording the particular Fermi edge on metallic components of the sample manipulator for each photon energy. TAT and 4T molecules were deposited by in-situ sublimation from quartz crucibles.

Figure 1 shows the photon-energy dependent UPS of a) a TAT thin film on HOPG and b) of a TAT thin film in a heterostructure with 4T. Figure 1 c shows the maxima of the HOMO-derived peak of the pristine TAT film. In a TB-model the dispersion can be expressed as

$$E_B(k_\perp) = E_B^0 - 2tcos(a_\perp k_\perp)$$

with the normal component of the electron momentum

$$k_\perp = \frac{\sqrt{2m_e^*(h\nu - E_B - V_0)}}{\hbar}.$$

In this context, E_B^0 denotes the energy of the band centre, t the transfer integral, $a_\perp$ the lattice spacing along the surface normal, $h\nu$ the photon energy, V_0 the inner potential and E_b the HOMO binding energy with respect to the vacuum energy. The data points were fitted by a least-squares fitting procedure with E_B^0, t and V_0 being treated as fitting parameters. In this way, t = 13.5 meV, E_B^0 = 6.546 eV and V_0 = -0.5 eV were obtained for the TAT HOMO energy dispersion. Regarding the 4T:TAT blend, the TB model yields t = 6.065 meV, E_B^0 = 6.423 eV and V_0 = -5.6 eV.

In conclusion, intermolecular energy-band dispersion of the TAT HOMO perpendicular to the molecular planes, is clearly identified for both the TAT multilayer film and the 4T:TAT blend. Comparatively narrow bandwidths well below 0.1 eV are identified, with the 4T:TAT bandwidth being significantly decreased compared to the initial TAT multilayer film. Therefore, suchlike donor-acceptor heterojunctions are rendered promising candidates as integral parts of organic-based devices. We further demonstrate that an experimental determination of very narrow bandwidths at room temperature is indeed feasible by means of UPS.

The results have been published in [1].

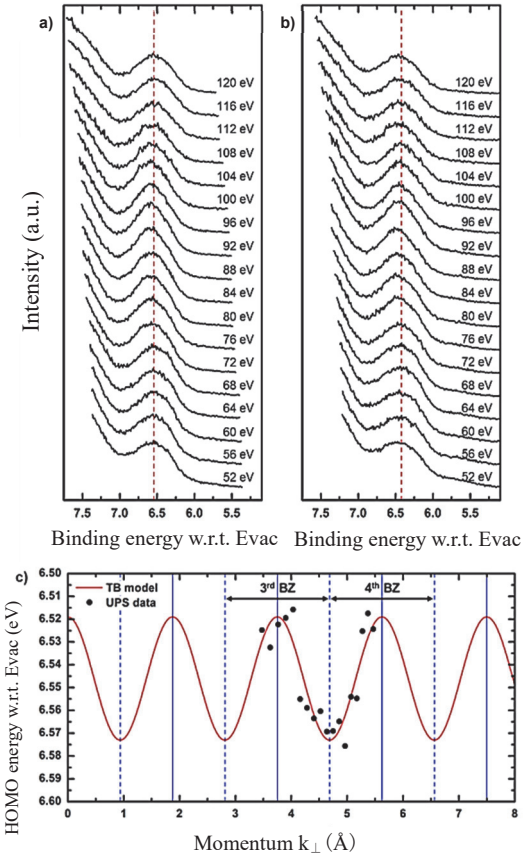

Fig. 1. HOMO region of photon energy-dependent normal emission UPS spectra of a) a TAT thin film with a nominal thickness of 150 Å and b) a 120 Å 4T/ 150 Å TAT blend on HOPG. c) TAT HOMO energy dispersion perpendicular to the molecular planes as derived from photon energy-dependent UPS. Black dots denote experimental data, whereas red curves are associated with the TB mode.

[1] N. Aghdassi, Q. Wang, R.-R. Ji, B. Wang, J. Fan and S. Duhm, Nanotechnology **29** (2018) 194002.

BL3B

Characterization of Intrinsic Luminescence from Orthophosphate and Borophosphate Crystals with Multiple Nonequivalent Oxoanions upon Vacuum UV Excitation

N. Kodama, C. Takahashi, H. Kubota and T. Takahashi
Graduate School of Engineering Science, Akita University, Akita 010-8502, Japan

To date, there has been very little work focusing on the formation of molecular-type excitons in the local structure of low-symmetry complex rare-earth oxides with multiple nonequivalent oxoanions of the PO_4^{3-} or BO_3^{3-} group. To the best of our knowledge, for these complex oxoanion crystals, a comprehensive understanding of the correlation between intrinsic luminescence bands and the number and symmetry of nonequivalent oxoanion groups such as PO_4^{3-} and/or BO_3^{3-} is still lacking. We focused on orthophosphate and borophosphate crystals with multiple nonequivalent PO_4^{3-} and/or BO_3^{3-} oxoanion groups. The first type is $Li_3Sc_2(PO_4)_3$ (LSP) with three nonequivalent PO_4^{3-} groups. The second type is $CaK(PO_4)_2$ (CKP) with two nonequivalent PO_4^{3-} groups. The third type is $Ba_3(BO_3)(PO_4)$ (BBP) with one PO_4^{3-} group and one BO_3^{3-} group.

We report intrinsic luminescence from self-trapped excitons (STEs) as intra-anion excitons in these crystals. In addition, we discuss the correlation between intrinsic luminescence bands from STEs and the number of nonequivalent PO_4^{3-} and/or BO_3^{3-} groups in LSP, CKP, and BBP.

Luminescence and excitation spectra of STEs in LSP, CKP, and BBP polycrystals were measured at twelve temperatures in the range of 8-293 K using the undulator BL3B at the UVSOR Synchrotron Facility. The emission spectra were corrected for the wavelength dependence of the diffraction monochromator and CCD detector using calibrated deuterium and halogen lamps as standard light sources. Time-resolved spectra were measured using a pulse with a width of 10 ns from a F_2 pulsed laser operating at 157 nm, and the decay times were determined.

All samples were found to exhibit multiple STE luminescence bands in the UV region under VUV excitation at 70 and 160 nm. The excitation spectral intensity in the 70-220 nm wavelength range for the orthoborate and borophosphate crystals increased rapidly below about 175-180 nm. Broad excitation bands were assigned to bandgap excitations or molecular transitions of the PO_4^{3-} or BO_3^{3-} group.

Figures 1(a)-1(f) show the luminescence spectra for LSP, CKP, and BBP at 8 and 293 K, excited at 70 nm. In order to estimate the number and peak energy of the bands, the spectra are deconvoluted into Gaussians in Figs. 1(a)-1(d). The luminescence spectra of LSP at 293 K and 8 K comprised, respectively, three distinct broad bands associated with STE(I), (II), and (III) having peaks at 263-247, 351, 430-476 nm, as shown in Figs. 1(a) and 1(b). These three intrinsic bands are assigned to STE(I), STE(II), and STE(III) in three sets of nonequivalent PO_4^{3-} groups. The spectra of CKP at 8 K consisted of two broad bands with peaks at 245 and 303 nm, and 281 and 364 nm, respectively, as shown in Figs. 1(c) and 1(d), associated with STE(I) and STE(II) in two sets of nonequivalent PO_4^{3-} groups. On the other hand, as shown in Figs. 1(e) and 1(f), BBP exhibited one broad band at 8 and 293 K. In LSP and CKP, the number of intrinsic luminescence bands corresponds to the number of nonequivalent PO_4^{3-} groups, whereas in BBP, only one band appears, despite the presence of a PO_4^{3-} group and a BO_3^{3-} group. The number of bands is inconsistent with the number of PO_4^{3-} and BO_3^{3-} groups. A possible explanation for this discrepancy is that a self-trapping of excitons takes place in either the PO_4^{3-} or BO_3^{3-} group with different geometries. The peaks of the STE luminescence bands in all samples (LSP, CKP, BBP) shifted to shorter wavelengths with decreasing temperature from 293 to 8 K.

The radiative decay curves consist of a fast and a slow component due to high-spin and low-spin STEs associated with the two possible spin orientations for the exciton electron-hole pair, as observed in alkali halides [1]. For LSP, the decay times for STE(I) luminescence at 243 nm are 15 ns and 174 ns, and those for STE(II) at 300 nm are 28 ns and 148 ns.

The fast decay components for STE(I) and STE(II) in LSP may originate from singlet STE states in two PO_4^{3-} groups with C_1 symmetry. In contrast, the slow decay components for STE(I) and STE(II) are attributed to triplet STEs in two PO_4^{3-} groups in which triplet STE states occur.

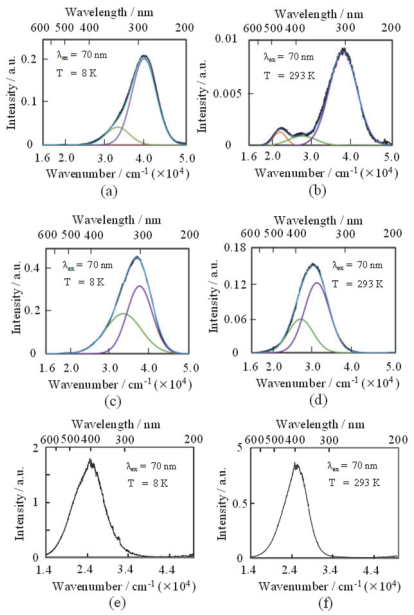

Fig. 1. The decompositions of intrinsic luminescence spectra excited at 160 nm in (a) and (b) LSP, (c) and (d) CKP, and in (e) and(f) BBP at 8 K and 293 K.The calculated components of the Gaussians are represented by yellow, orange, and gray lines.

[1] T. T. Williama, K. S. Song, J. Phys. Chem. Solds. **51** (1990) 679.

BL3B

Bandgap Energy of La and Y admixed $Gd_2Si_2O_7$ Crystals Using the UVSOR Facility

T. Horiai[1], S. Kurosawa[2, 3], A. Yamaji[1], S. Kodama[1], S. Yamato[1], Y. Shoji[1, 4], M. Yoshino[1], Y. Ohashi[2], K. Kamada[2, 4], Y. Yokota[2] and A. Yoshikawa[1, 2, 4]

[1]*Institute for Materials Research, Tohoku University, Sendai 980-8577, Japan*
[2]*New Industry Creation Hatchery Center (NICHe), Tohoku University, Sendai 980-8579, Japan*
[3]*Department of Physics, Yamagata University, Yamagata 990-8560, Japan*
[4]*C&A Corporation, Sendai 980-8579, Japan*

Scintillation crystals convert energy of ionizing radiation such as gamma-ray and X-ray into multiple photons of energy 2~8 eV. Scintillators are used in several fields, and oil-well exploration is one of the application fields [1-3]. Specifically, scintillators are used in gamma-ray detectors in combination with a photodetector to discriminate geologic layers at oil well exploration sites. Since the ground temperature in shale layer is reached approximately 200ºC, the noise by dark current of the photomultiplier tube (PMT) is become larger. On the other hand, the light outputs are dropped for conventional scintillators. To solve degrading the signal-to-noise ratio, the development of new scintillator which could keep high light output even at high temperature is required.

To satisfy this requirement, Ce-doped $(Gd,La)_2Si_2O_7$ (Ce:La-GPS) has been investigated. Ce:La-GPS has a light output of ~42,000 photons/MeV, and the light output is maintained even at 150°C [4]; however, for high temperature applications, further improvement is needed. In this study, we focus on Y-admixed Ce:La-GPS and optimize Y concentration to improve the temperature dependence. Here, in previous studies, the thermal quenching of Y-admixed Ce-doped Lu_2SiO_5 (Ce:LYSO) was suppressed when compared to Y-free sample (Ce:LSO) [5, 6].

We prepared $(Gd_{0.59-x}\ Ce_{0.01}\ La_{0.40}\ Y_x)_2Si_2O_7$ (Ce:LaY-GPS) single crystals grown by the micro-pulling-down method, and UV absorption edge for these samples were evaluated with a photo diode (IRD, AXUV 100) at BL3B of UVSOR. The bandgap energies were calculated from the UV absorption edge.

From the result of the temperature dependence of light output at 25ºC and 175ºC, Y5% substituted Ce:La-GPS was improved (Table 1). On the other hand, the light output of Y15% substituted Ce:La-GPS was degraded.

Figure 1 shows the UV absorption spectra of Y0% and 15% substituted Ce:La-GPS. From this figure, the UV absorption edge wavelength were constant regardless of Y concentration (~174 nm), and the bandgap energies were determined appoloximately 7.14 eV. Thus, the improvement factor of temperature dependence of light output was not the effect of the bandgap energy.

Table 1. Light outputs of $(Gd_{0.59-x}, Ce_{0.01}, La_{0.40}, Y_x)_2Si_2O_7$ at 25ºC and 175ºC

Sample	Light output @ 25ºC [photons/MeV]	Light output @ 175ºC [photons/MeV]
x = 0.00	42,000	34,000
x = 0.05	43,000	40,000
x = 0.10	36,000	34,000
x = 0.15	33,000	24,000

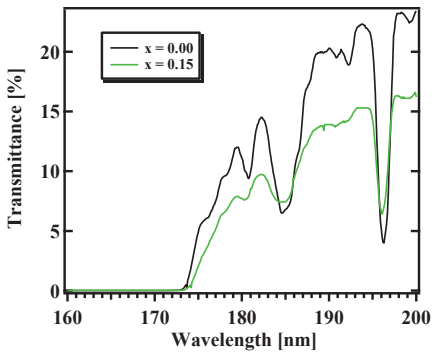

Fig. 1. UV absorption spectra of $(Gd_{0.59-x}, Ce_{0.01}, La_{0.40}, Y_x)_2Si_2O_7$ at 6 K.

[1] C. Rozsa, R. Dayton, P. Raby, M. Kusner and R. Schreiner, IEEE Trans. Nucl. Sci. **37** (1996) 966.
[2] A. Baberdin, A. Dutova, A. Fedorov, M. Korzhik, V. Ligoun, O. Missevitch, V. Kazak, A. Vinokurov and S. Zagumenov, IEEE Trans. Nucl. Sci. **55** (2008) 1170.
[3] C.L. Melcher, J.S. Schweitzer, R.A. Manente and C.A. Peterson, J. Crystal Growth **109** (1991) 37.
[4] S. Kurosawa, T. Shishido, T. Sugawara, A. Nomura, K. Yubuta, A. Suzuki, R. Murakami, J. Pejchal, Y. Yokota, K. Kamada and A. Yoshikawa, Nucl. Instrum. Methods Phys. Res. A **772** (2015) 72.
[5] H. Suzuki, T.A. Tombrello, C.L. Melcher and J.S. Schweitzer, IEEE Trans. Nucl. Sci. **40** (1993) 380.
[6] L. Pidol, A. Kahn-Harari, B. Viana, E. Virey, B. Ferrand, P. Dorenbos, J.T.M. Haas and C.W.E. Eijk, IEEE Trans. Nucl. Sci. **51** (2004) 1084.

BL3B

Insight into the High Light Output of Ce:(Gd, La)$_2$Si$_2$O$_7$ Scintillator

S. Kurosawa[1, 2], A. Yamaji[3], T. Horiai[3], S. Kodama[3], S. Yamato[3], Y. Shoji[3, 4], Y. Ohashi[3], Y. Yokota[1], K. Kamada[1, 4], A. Yoshikawa[1, 3, 4] and M. Kitaura[2]

[1] *New Industry Creation Hatchery Center (NICHe), Tohoku University, Sendai 980-8579, Japan*
[2] *Faculty of Science, Yamagata University, Yamagata 990-8560, Japan*
[3] *Institute for Materials Research (IMR), Tohoku University, Sendai 980-8577, Japan*
[4] *C&A Corporation, Sendai 980-8577, Japan.*

Crystalline scintillators have been used in various fields such as medical imaging, astronomy and so on. Recently, scintillation properties of ($Ce_{0.01}$, $Gd_{0.90}$, $La_{0.09}$)$_2$$Si_2O_7$ (Ce:La-GPS) have been studied. The Ce:La-GPS crystal had the light output of around 4,000 photons/MeV and the FWHM energy resolution of 5.0% at 662 keV [1, 2]. Moreover, the light output was constant in the temperature range from 10 to 423 K [3]. Thus, the Ce:La-GPS crystal is applicable to radiation detection at high temperatures.

The evaluation of the bandgap energy is very much important for the development of more functional scintillators. From this viewpoint, we have evaluated the bandgap energy of La-GPS crystals at the BL3B of UVSOR. The bandgap energy of La-GPS was estimated to be over 7.13±0.03 eV. Compared with other oxide scintillators, Ce:La-GPS was found to have wider bandgap. Generally, the light output of scintillator is inversely proportional to the band-gap energy. Despite such a large bandgap energy, the light output is larger than those of other oxide scintillators with small bandgap energies. This result implies that the product of transfer efficiency and/or electron-hole pair generation efficiency in Ce:La-GPS is higher than those in others. The cause may be due to small number of traps in Ce:La-GPS. In order to clarify high light output in Ce:La-GPS, we have investigated thermo-luminescence (TL) properties under irradiation with vacuum ultraviolet (VUV) radiation.

Figure 1 and 2 show TL emission spectra and TL glow curve for Ce:La-GPS, respectively, where the TL intensity is the integrated value from the TL emission spectrum at each temperature. The TL glow peak is found at around 120 K. The TL glow curve for 1.5% Ce-doped Gd_2SiO_5 (Ce:GSO) was also measured for a reference. Apparently, the integrated value of the 120 K peak for Ce:La-GPS is smaller than the sum of integrated values of a number of peaks for Ce:GSO up to 300 K. Since Ce:La-GPS have small number of the traps which block the electron transportation into luminesce center, the transfer efficiency becomes high, compared to Ce:GSO. Details of the present study will be reported in Ref. 4.

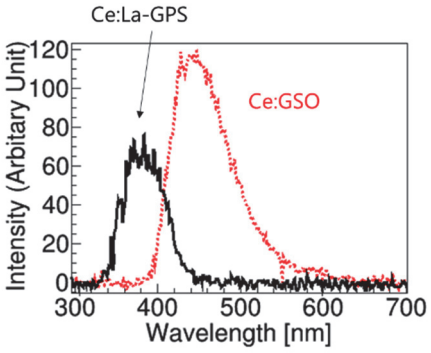

Fig. 1. TL-emission spectra for Ce:La-GPS at 120K and Ce:GSO at 282K.

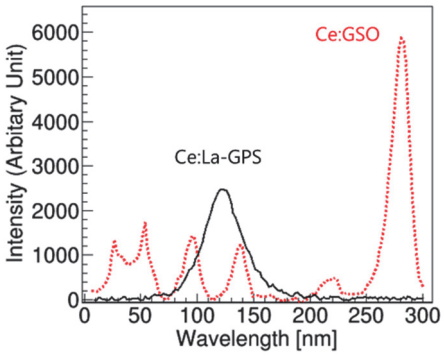

Fig. 2. TL glow curves of Ce:La-GPS (solid line) and Ce:GSO (dotted line).

[1] A. Suzuki *et al.*, Applied Physics Express **5** (2012) 102601.
[2] S. Kurosawa *et al.*, Nucl. Inst. and Meth. in Phys. Res. **A774** (2014)30.
[3] S. Kurosawa *et al.*, Nucl. Inst. and Meth. in Phys. Res. **A772** (2015)72.
[4] S. Kurosawa *et al.*, IEEE Trans. Nucl. Sci. Acceptted.

BL3B

PL Decay Times of Trans-stilbene and 1,4-Bis(2-methylstyryl) Benzene (BisMSB)-doped Trans-stilbene at 13-300 K

S. Yamato[1], A. Yamaji[1], S. Kurosawa[2, 3], M. Yoshino[1], Y. Ohashi[2], K. Kamada[2, 4], Y. Yokota[2] and A. Yoshikawa [1, 2, 4]

[1]*Institute for Materials Research (IMR), Tohoku University, Sendai 980-8577, Japan*
[2]*New Industry Creation Hatchery Center (NICHe), Tohoku University, Sendai 980-8579, Japan*
[3]*Fuculty of science, Yamagata University, Yamagata 990-8560, Japan*
[4] *C&A Corporation, Sendai 980-8577, Japan.*

Neutron detectors can be used in several fields such as homeland security and maintenance of social infrastructure. In such applications, gaseous detectors can be used due to high and low detection efficiency for neutron and gamma rays as background noise, respectively. However, gaseous detectors contain expensive gas or toxic gas like ^{3}He and BF_3, and scintillators are expected to be an alternative detector. Here, neutron energy is evaluated using Time-of-Flight (TOF) method, and the energy resolution depends on the timing response of the scintillator. Therefore, inorganic scintillators with long decay time are not suitable for measurements of neutron energies.

Organic scintillators are used as neutron detectors, and trans-stilbene crystals, for example, have decay time of 6.4 ns [1] and good pulse shape discrimination (PSD) property, which is often operated to discriminate neutron/gamma [2]. Organic non-single-crystal scintillators such as liquid scintillators (LSs) and plastic scintillators (PSs) are applied to detection of underground environment neutron and energy spectrum measurement of fast neutrons, etc., because these scintillators have faster scintillation decay than organic "crystal" scintillators. However, LSs are flammable and toxic, and PSs have low radiation hardness. Therefore, we focused on organic crystal scintillators which are safer and more stable than LSs and PSs.

We grew pure trans-stilbene crystal and 1,4-Bis(2-methylstyryl) benzene (BisMSB)-doped trans-stilbene crystal, by the self-seeding vertical Bridgman method using an enclosed chamber [3]. The doping amount of BisMSB was 1wt%. Pulling down rate for growth was 1.44 mm/h. BisMSB was used as solutes in LSs and PSs, and BisMSB doped LSs have fast decay times of ~2 ns [4].

We measured the photoluminescence (PL) emission spectra of the samples excited by 260-nm photons at 13 and 300 K as shown in Fig. 1, with the BL3B at UVSOR Synchrotron Facility, using a photo multiplier tube (PMT) (C5594, Hamamatsu Photonics) and a CCD camera (MODEL:TN/CCD/100PBVISAR, Princeton Instruments). At 300 K, the emission peaks ranged from 400 to 550 nm were appeared for the BisMSB-doped crystal. Although the spectrum was shifted by doping BisMSB at 13 K, the peak was blue-shifted compared to that at 300 K.

The PL decay times of the samples excited by 260-nm photons at 13-300 K are summarized in Table 1. The ranges of excitation wavelength and emission wavelength for PL decay measurements were from 226 to 293 nm and from 295 to 680 nm, respectively. The PL decay time of trans-stilbene matched the value in previous report [5]. Despite the difference of luminescence spectra, there was almost no difference in photoluminescence decay times between the two crystals. Further study is necessary to reveal the reason.

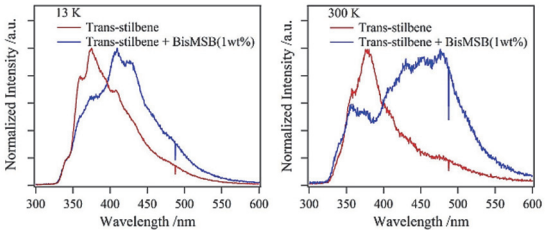

Fig. 1. Emission spectra of grown crystals excited by 260 nm at 13 K and 300 K.

Table 1. Photoluminescence decay times of grown crystals excited by 260 nm at 13-300 K

T [K]	Trans-stilbene	Trans-stilbene + BisMSB(1wt%)
	τ_1 [ns]	τ_1 [ns]
13	1.9	1.8
50	1.9	1.8
100	1.7	1.7
200	1.2	1.5
250	1.1	1.5
300	1.0	1.1

[1] J. B. Birks, The Theory and Practice of Scintillation Counting, (Pergamon, Oxford, 1964).
[2] N. Zaitseva *et al*., IEEE Trans. Nucl. Sci. **58** (2011) 3411.
[3] A. Arulchakkaravarthi *et al*., J. Crystal Growth **234** (2002) 159.
[4] M. M. de Souza *et al*., Synth. Metals **101** (1999) 631.
[5] D. J. S. Berch *et al*., Chem. Phys. Lett. **38** (1976) 432.

BL3B

Temperature Dependence of Cs_2HfI_6 Transmittance Spectra

S. Kodama[1], S. Kurosawa[2, 3], A. Yamaji[1], M. Yoshino[1], Y. Ohashi[1], K. Kamada[2, 4], Y. Yokota[2] and A. Yoshikawa[1, 2, 4]

[1] *Institute for Materials Research (IMR), Tohoku University, Sendai 980-8577, Japan*
[2] *New Industry Creation Hatchery Center (NICHe), Tohoku University, Sendai 980-8579, Japan*
[3] *Faculty of Science, Yamagata University, Yamagata 990-8560, Japan*
[4] *C&A Corporation, Sendai 980-8577, Japan*

A_2HfX_6 (A: monovalent cation, X: halogen ion) compounds are host-emitting materials originated from self-trapped exciton. Since the crystal lattice of A_2HfX_6 compounds can be a well-ordered and high symmetry cubic structure (space group: *Fm-3m*), producing a transparent single crystal is easy. Actually, Cs_2HfCl_6 (CHC) or anion-admixed $Cs_2HfCl_2Br_4$ had been reported as single-crystalline scintillators so far [1-2], and CHC has a high scintillation light-output of over 50,000 photons/MeV.

Generally, the light output of scintillator (Y) is inversely proportional to band-gap energy of the host material (E_{gap}); $Y \propto (E_{gap})^{-1}$. In order to realize the higher light output than CHC, Cs_2HfI_6 (CHI) is investigated in this study, because the Egap of CHC and CHI were calculated as ~6.4 eV and ~3.9 eV, respectively [3].

A single-crystalline CHI specimen was synthesized from 99%-pure HfI_4 and 99.999%-pure CsI using the vertical Bridgman growth method. CHI was revealed to emit orange-red light around 650 nm, and had a high light output of ~70,000 photons/MeV, a moderate fast scintillation decay of ~2.5 μs. We found that CHI is a first noble red-emitting scintillator applicable to the photon-counting detect technique.

To develop CHI furthermore, the evaluation of fundamental optical properties should be necessary, and we measured transmittance spectra of CHI at room temperature and 8 K cooled by liquid Helium in a cryostat chamber of UVSOR BL3B. Transmittance spectra were measured with a photo-diode (IRD, AXUV 100). The light source was a synchrotron light.

Figures indicate the obtained transmittance spectra of CHI at room temperature and 8 K. The transmittance gradually decreased towards shorter wavelength from 700 nm. We observed a transmittance drop around ~480 nm at room temperature, and the dropping wavelength was revealed to shift to ~440 nm at 8 K due to lattice vibration. Since CHI was revealed to absorb the blue-yellow visible light around ~480 nm, CHI crystal had the orange color. CHI should have an absorption edge around ~320 nm based on the calculated E_{gap} of ~3.9 eV. The transmittance drop at ~480 nm was considered to be an absorption of the self-trapped exciton.

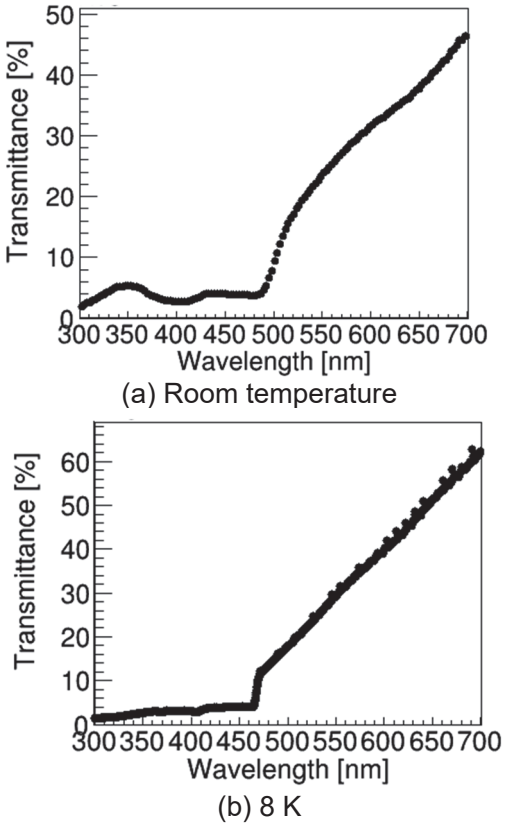

Fig. Transmittance spectra of CHI crystal. (a) and (b) are spectra at room temperature and 8 K, respectively.

[1] A. Burger *et al.*, Appl. Phys. Lett. **107** no. 14 (2015) 34.
[2] S. Lam, C. Guguschev, A. Burger, M. Hackett, and S. Motakef, J. Cryst. Growth **483** (2018) 121.
[3] B. Kang and K. Biswas, J. Phys. Chem. C **120** no. 22 (2016) 12187.

BL3B

Evaluation of Optical Basic Properties of Ultra-Violet Emitting Zinc Aluminate Phosphor

H. Kominami[1], K. Hada[1], S. Kubota[1], K. Kijima[1], M. Ohkawa[1], Y. Kato[1], T. Matsuura[2], M. Arimura[2], K. Imagawa[2] and K. Warita[2]

[1]*Graduate School of Integrated Science and Technology, Shizuoka University, Hamamatsu 432-8651, Japan*
[2]*Faculty of Engineering, Shizuoka University, Hamamatsu 432-8651, Japan*

The UV light is used for various applications depending on the wavelength as well as the sterilization described above. The lights of 200-280 nm (UV-C) region as for the sterilization, 280-320 nm (UV-B) region as the treatment of the skin disease, 320-400nm (UV-A) region as application of purification of water and air, and photocatalysts. Recently, from the viewpoint of consideration to the environment, the mercury free UV emission devices have been demanded for the application of catalyst and medical situations. In our previous work, it was clarified that $ZnAl_2O_4$ phosphor was suitable for the UV field emission lamp because of its stability and luminescent property. It shows strong UV emission peaked around 250 nm which suitable for sterilization. In $ZnAl_2O_4$, the application as the sterilization light source is expected from the luminescence wavelength area, but it is not sure about the application as other ultraviolet light sources. Therefore, the possibility of the application of the ultraviolet light source is thought about by controlling composition of $ZnAl_2O_4$.

$Zn(Al_{1-x}Ga_x)_2O_4$ powders were prepared by solid phase synthesis using ZnO (99.999%), α-Al_2O_3 (99.99%) and Ga_2O_3 (99.9%) powders. The Ga ratio x was changed from 0 ~ 1 for control the phase. The powders were fired at 1000 ~ 1300 ºC for 3 hours in air. And the powders were evaluated using X-ray diffraction (XRD), Cathodoluminescence (CL) and Photoluminescence (PL, PLE).

Figure 1 shows cathodoluminescent spectra of $Zn(Al_{1-x}Ga_x)_2O_4$ phosphors fired at 1300ºC in air. The emission peak was shifted from 250 nm to 350 nm according to increasing of Ga ratio X. However, CL intensity of phosphors were quite different by Ga composition. Especially, the powders at x = 0.5 and 1 showed poor luminescence. It is thought that the distortion of crystallinity was occurred for the powder of x = 0.5. On the other hand, for the powder of x = 1, the optimum firing condition of $ZnGa_2O_4$ was different from $ZnAl_2O_4$.

Figure 2 shows Photoluminescent excitation spectra of $Zn(Al_{1-x}Ga_x)_2O_4$ phosphors fired at 1300ºC in air, measured at 8K. The excitation band was shifted to longer wavelength according to increase of Ga ratio X. From our previous work, the PLE absorption edge of $ZnAl_2O_4$ was equivalent to forbidden gap. It indicates that forbidden gap of $Zn(Al_{1-x}Ga_x)_2O_4$ phosphors became narrower according to increase of Ga ratio. The energy of absorption edge was changed linearly. From XRD measurement also shows $Zn(Al_{1-x}Ga_x)_2O_4$ phosphors successfully synthesized at 1300ºC firing because of the shift of diffraction peak obeyed Begard's law. it seems that the replacement of Ga to Al-site was occurred smoothly.

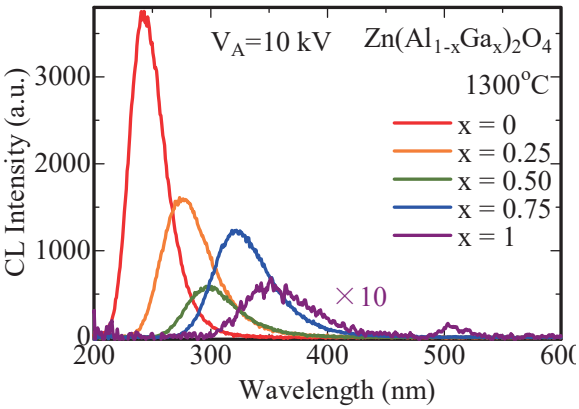

Fig. 1. CL spectra of $Zn(Al_{1-x}Ga_x)_2O_4$ alloy phosphor.

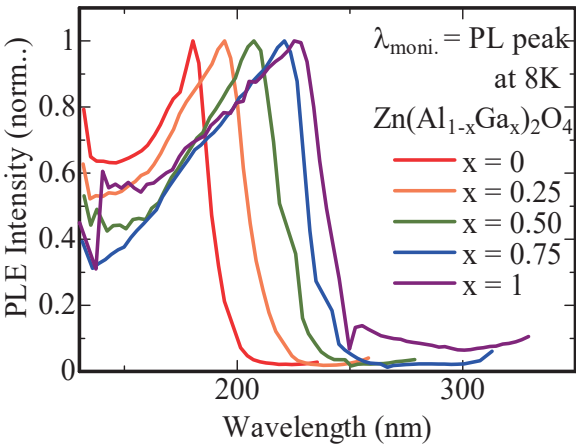

Fig. 2. PLE spectra of $Zn(Al_{1-x}Ga_x)_2O_4$ phosphor at 8K monitored at CL peak.

BL3B

Emission Spectra of Pr-doped SrY_2O_4

M. Yoshino, S. Nishiki, T. Kuyama and S. Watanabe
Graduate School of Engineering, Nagoya University, Nagoya 464-8603, Japan

The trivalent lanthanide ions (e.g., Ce^{3+}, Nd^{3+}, Er^{3+}) in oxide crystals have drawn attentions due to their application for luminescent materials in NIR to UV regions such as solid-state lasers, phosphors or scintillators. The trivalent praseodymium ion, Pr^{3+}, has also attracted attentions as luminescence centers. In this work, the excitation spectra and emission spectra for Pr^{3+} in SrY_2O_4 crystal have been measured. The Pr-doped SrY_2O_4 samples are synthesized by solid state reactions. The samples are annealed in N_2-H_2 atmosphere in order to reduce Pr^{4+} to Pr^{3+}. The concentration of Pr in the samples are 0.5, 1.0, 1.5, 2.0 and 3.0 mol%.

The excitation spectrum monitored at 520 nm emission contains absorption around 315 nm and 273 nm and they originate the 4*f*-5*d* transitions of Pr^{3+} [1]. The emission spectra at 315 and 273 nm excitation in 300 K are shown in Fig. 1 and Fig. 2, respectively.

Peaks A, B, C, D, E exist in the each spectra. On the other hand, peak F appears only in 273 nm excitation and has different dependency to Pr concentration compared with the other peaks. The intensity of F decrease with Pr concentration while it decreases after the increase in A, B, C, D and E. The emission spectra at 315 and 273 nm excitation in different temperatures are shown in Fig. 3 and Fig. 4, respectively. It is found that the peak F has also different dependency to temperature compared with the other peaks. The intensity of F is high when it measured in high temperature while it decreases monotonously with temperature in the other peaks. The peak F is not seen in the spectrum of 315 nm excitation in each temperature.

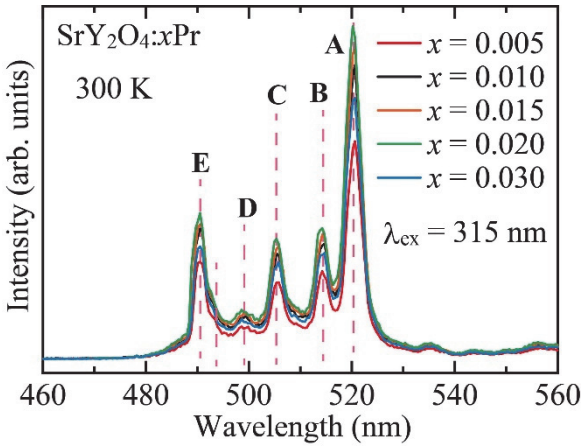

Fig. 1. Emission spectra of SrY_2O_4:*x*Pr. (λ_{ex}= 315 nm, 300 K).

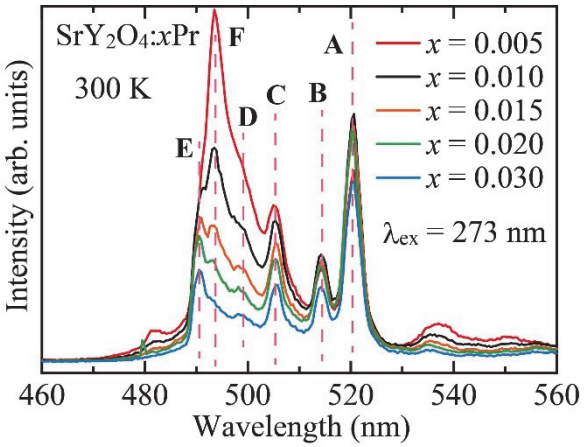

Fig. 2. Emission spectra of SrY_2O_4:*x*Pr. (λ_{ex}= 273 nm, 300 K).

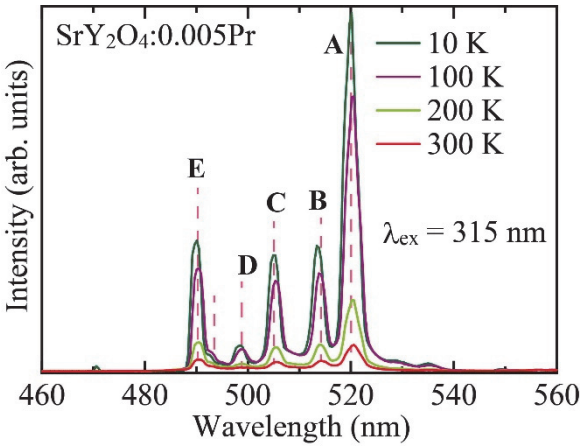

Fig. 3. Emission spectra of SrY_2O_4:0.005Pr. (λ_{ex}= 315 nm).

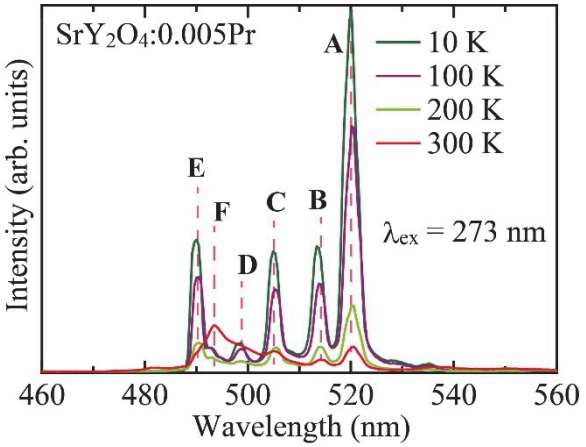

Fig. 4. Emission spectra of SrY_2O_4:0.005Pr. (λ_{ex}= 273 nm).

[1] M. Yoshino, S. Nishiki and S. Watanabe, UVSOR Activity Report **43** (2016) 95.

BL3B

Energy Transfer from I^- Centers to Tl^+ Centers in Co-Doped NaCl: I^-, Tl^+ Crystals

O. Yagi and T. Kawai
Graduate School of Science, Osaka Prefecture University, Sakai 599-8531, Japan

Energy transfer mechanism in solid crystals is one of the interesting research topics in solid state physics. Many experimental investigations have been performed on the crystals co-doped with two kinds of impurities. The resonant transfer and the emission reabsorption are well-known as the mechanism of the energy transfer. Both the mechanisms can occur if there is the overlap between the donor's luminescence band and the acceptor's absorption band [1].

In this study, we have investigated the NaCl crystals co-doped with I^- and Tl^+ ions (NaCl:I^-,Tl^+) to discuss the existence and the mechanism of the energy transfer. NaCl crystals have the wide band-gap up to the vacuum ultraviolet energy region and are a suitable candidate host for doping of impurity ions. NaCl crystals doped with iodine anion (NaCl:I^-) exhibit intense luminescence in deep ultra-violet region even at room temperature (RT), so iodine anions in NaCl are a suitable donor impurity.

Figure 1 shows the absorption spectrum of NaCl:Tl^+ and the luminescence spectrum of NaCl:I^- at RT. NaCl:Tl^+ produces three absorption bands labeled with A, B, and C at 4.8, 5.3, and 6.2 eV respectively. These absorption bands are attributed to the intra-ionic transitions from the ground $^1S_0$ state to the excited $^3P_1$, $^3P_2$, and $^1P_1$, states. NaCl:I^- shows the luminescence band appearing around 5.2 eV. It is called the NE luminescence band and comes from the one-center type localized exciton, which is localized on the central site of a substituted I^- impurity with small lattice relaxation [2]. The NE luminescence band in NaCl:I^- has almost no overlap with the absorption bands in NaCl:Tl^+. This fact indicates that the resonant energy transfer and the emission reabsorption from the I^- centers to the Tl^+ centers are hard to occur.

Figure 2 shows the decay profiles of the NE luminescence in the NaCl:I^-,Tl^+ under the excitation on the I^- absorption band (6.8 eV) at 6, 160, 200, and 240 K. The decay profiles at 6~160 K exhibit a single exponential decay. The decay time constants at 10 and 160 K are 88 and 43 ns, respectively, which are the same as the decay time of the NaCl:I^-. On the other hand, the decay profiles at 200~300 K exhibit two exponential decay components. Both decay components become faster with increasing temperature. The behavior of the decay profiles indicates the existence of the energy transfer from the I^- centers to the Tl^+ centers at more than 200 K. We are analyzing the decay profiles with the energy transfer model via carrier diffusion reaction.

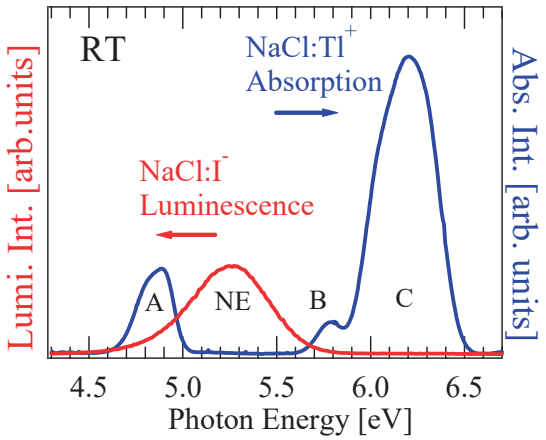

Fig. 1. Luminescence spectrum (Red) of NaCl:I^- and absorption spectrum (blue) of NaCl: Tl^+ at RT.

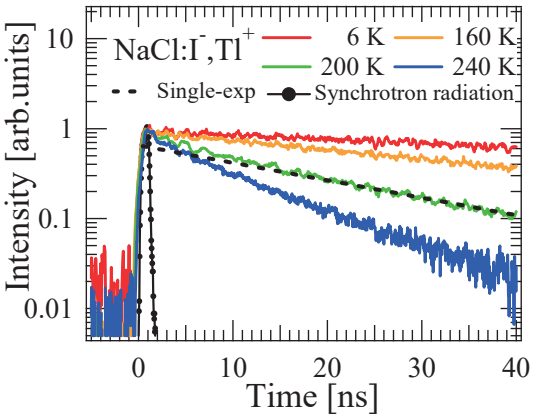

Fig. 2. Decay profiles of the NE luminescence in the NaCl:I^-,Tl^+ at 6, 160, 200, and 240 K.

[1] A. Iguchi, T. Kawai and K. Mizoguchi, Phys. Status Solidi. C **13** (2015) 85.
[2] I. Akimoto, M. Shimozato and K. Kan'no, Phys. Status Solidi. C **6** (2009) 342.

BL3B

Comparison of Luminescence Properties at Room Temperature between NaI:Tl$^+$ and NaI:In$^+$ Crystals

S. Watanabe and T. Kawai
Graduate School of Science, Osaka Prefecture University, Sakai 599-8531, Japan

Alkali halide crystals doped with Tl$^+$-type centers have been extensively studied until now. The Tl$^+$-type centers exhibit the optical bands called A, B, and C, which are attributed to intra-ionic transitions from the $^1A_{1g}$ ground state to the $^1T_{1u}$, $^3T_{2u}$+^3E_u, and $^3T_{1u}$ excited states, receptively [1,2].

Among the alkali halides doped with the Tl$^+$-type centers, CsI:Tl$^+$ and NaI:Tl$^+$ crystals have been widely used as a scintillator and investigated in detail. Especially, NaI crystals doped with the Tl$^+$ centers have the high scintillation yield and faster time response. On the other hand, optical studies on NaI crystals doped with In$^+$ centers have not been reported to our knowledge. In this study, optical properties of the NaI:In$^+$ crystals have been investigated at room temperature (RT).

NaI:In$^+$ and NaI:Tl$^+$ crystals were grown by the Bridgman method from NaI beads and InI or TlI powders, respectively. The samples used for the measurements were cleaved in a nitrogen-filled glove box. Optical measurements were performed at the BL3B of UVSOR.

Figure 1 shows the luminescence spectra of NaI:In$^+$ and NaI:Tl$^+$ under excitation at 200 nm at RT. In NaI:Tl$^+$, the A' luminescence band due to the radiative transition from the relaxed excited state of $^3T_{1u}$ is confirmed at 425 nm [3]. The NaI:In$^+$ crystal exhibits a broad luminescence band around 520 nm, which would assigned to the A' luminescence of the In$^+$ centers from the comparison with NaI:Tl$^+$.

Figure 2 shows the absorption (broken curve) and the excitation (solid curve) spectra for the A' luminescence of NaI:In$^+$ and NaI:Tl$^+$ at RT. The absorption band at 295 nm in NaI:Tl$^+$ corresponds to the A absorption band [3]. Since the absorption bands of the In$^+$ center in alkali halide crystals are located at the lower energy region than those of the Tl$^+$ centers, the band at 275 nm in NaI:In$^+$ would correspond to the C band. The A' luminescence bands in both the crystals are efficiently excited at the respective absorption bands. Furthermore, both excitation spectra demonstrate that the A' luminescence bands have responses even in the higher energy range than about 230 nm, where correspond to the energy region above the fundamental absorption edge of NaI host crystals. The fact indicates that the energy absorbed by the host crystals transfers to the energy level of the impurity centers. The luminescence properties of NaI crystals activated with various kind of impurity centers should be extensively investigated.

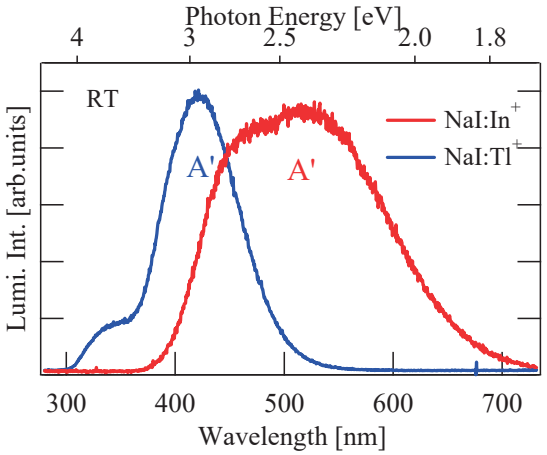

Fig. 1. Luminescence spectra of NaI:In$^+$ (red) and NaI:Tl$^+$ (blue) crystals excited at 200 nm at RT.

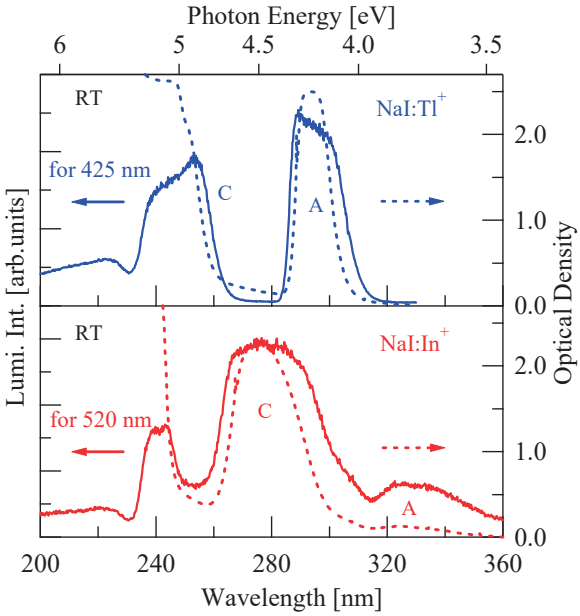

Fig. 2. Absorption (broken) and Excitation (solid) spectra for the A' luminescence of NaI:In$^+$ and NaI:Tl$^+$ at RT.

[1] A. Ranfagni *et al.*: Advances in Physics **32** (1983) 823.
[2] P. W. M. Jacobs: J. Phys. Chem. Solids **52** (1991) 35.
[3] M. P. Fontana and W. J. Van Sciver: Phys. Rev.**168** (1968) 960.

BL3B, BL7B

Total Photoelectron Yield Spectroscopy on 3*d* Transition Metal Doped AlN Films

N. Tatemizo[1], S. Imada[1], S. Hirata[2], W. Kamihigoshi[2] and K. Fukui[2]
[1]*Faculty of Electrical Engineering and Electronics, Kyoto Institute of Technology, Kyoto, 606-8585, Japan*
[2] *Faculty of Electrical and Electronics Engineering, University of Fukui, Fukui, 910-8507, Japan*

Intermediate band (IB) materials proposed by Luque *et al*., have gained attention for use in absorption layers of solar cells to increase their conversion efficiency [1]. Heavy 3*d*-transition metal (3*d*-TM) doped AlN films are one of the candidates of IB materials. Exploring the possibility of them, we have synthesized Ti [2], V [3] and Cr [4,5] doped AlN films and investigated their band structures.

The films were deposited on SiO_2 glass or Ti metal polycrystalline substrates by RF sputtering from an AlN target with Ti or Cr metal chips on it. Results of XRD, TEM and 3*d*-TM K-edge EXAFS showed that the films have wurtzite structures with Ti and Cr atoms occupied the Al sites of AlN [2,5]. To investigate the potentials of the electron occupied states (Valence band and/or a part of IB), we carried out total photoelectron yield spectroscopy (TPYS) [6] for the films deposited on Ti metal substrates. As show in Fig. 1. electrical contacts with the film were made both back (thorough the Ti substrate) and front (a Cu metal plate with hole). A photoelectron corrector was set in front of the film with around 1mm interspace. A negative bias was applied to the sample against the grounded photoelectron corrector. The number of photoelectrons was obtained by measuring the current needed to compensate for the photoexcited holes at the sample with an ammeter. The photoemission yield was measured as a function of incident photon energy.

Figure 2 shows TPY spectra of AlN films doped with 11.0 and 8.3% Ti and 12.3 and 9.3% Cr. It is clear that the Cr-doped films have threshold at around 5.5 eV, while threshold of the Ti-doped films is at around 6.0 eV. These results agree well with the theoretical levels of Cr and Ti in AlN [7]. We have obtained different thresholds for other different 3*d*-TM elements, which means the potential of IB can be controlled via choice of 3*d*-TM elements and adjust the band structure for the effective photoconversion. To reveal all potentials of the electron occupied band of the films, we will extend the energy region of the measurements to larger one.

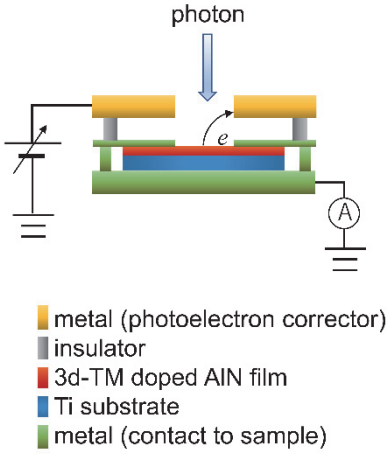

Fig. 1. Schematic of sample setting for the TPYS measurements.

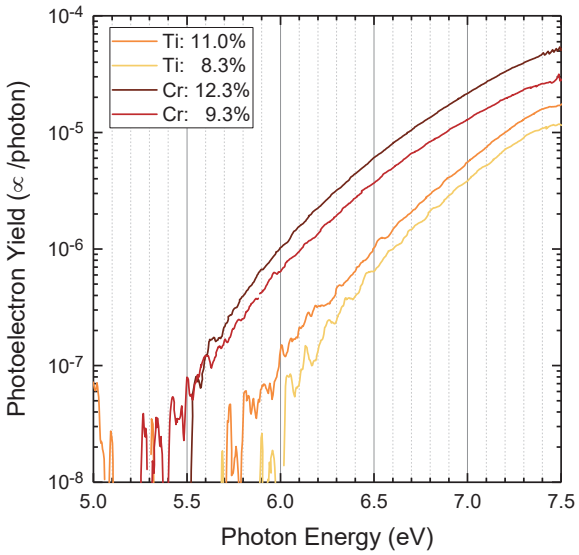

Fig. 2. Total photoelectron yield spectra of 3*d*-TM doped AlN films (12.3 and 9.3 % of Cr and 11.0 and 8.3 % of Ti) deposited on Ti metal substrates.

[1] A. Luque *et al*., Phys. Rev. Lett. **78** (1997) 5014.
[2] N. Tatemizo *et al*., J. Mater. Chem. A **5** (2017) 20824.
[3]N. Tatemizo *et al*., J. App. Phys., **123** (2018) 161546.
[4] N. Tatemizo *et al*., J. of Phys.: Conden. Matter, **29** (2017) 085502.
[5] N. Tatemizo *et al*., AIP advances, **7** (2017) 055306.
[6] M. Honda *et al*., J. Appl. Phys. **102** (2007) 103704.
[7] U. Gerstmann *et al*., Phys. Rev. B, **63** (2001) 1.

BL3B

Study of Defect Induced by Hydrogen Reduction in MgO Single Crystal by UV Absorption Spectroscopy

E. Kobayashi[1], K. K. Okudaira[2], S. Yoshioka[3], K. K. Bando[4] and O. Takahashi[5]

[1]*Kyushu Synchrotron Light Research Center, Tosu 841-0005, Japan*

[2]*Chiba University, Chiba 263-8522, Japan*

[3]*Gradiate School of Engineering, Kyushu University, Fukuoka 819-0395 Japan*

[4]*National Institute of Advanced Industrial Science and Technology, Tsukuba 305-8565, Japan*

[5]*Institute for Sustainable Science and Development, Hiroshima University, Higashi-Hiroshima, 739-8526, Japan*

Magnesium oxide (MgO) is a typical wide band gap insulator and is used in a wide range of devices [1-4]. Physical characteristics such as optical or electrical performances are greatly affected by the presence defects. Various types of defects are found in metal oxides, which are composed of points, lines and planes. The electronic state derived from those defects controls electrical, optical, or magnetic functions of devices. Therefore, a lot of efforts have been made so far to understand the effect of point defects on the electronic states of metal oxides so far, but more detailed atomic level investigation of defects is still desired.

In this study, we focused on magnesium oxide to see the effect of typical oxygen point defects on the electronic states derived from oxygen. We investigated the correlation between the defects and the electronic states using near-edge X-ray absorption fine structure (NEXAFS) spectroscopy and ultraviolet absorption spectroscopy.

The MgO single crystals were annealed at several temperatures at 673 K ~1173 K in a hydrogen atmosphere for 4 hours. The sample was gradually cooled to room temperature, exposed to the air, then introduced into a vacuum apparatus, and the spectrum was measured. UV spectra of MgO single crystal were measured at the BL3B of UVSOR in the Institute of Molecular Science.

The change in the band gap created by oxygen defects was investigated with transmission spectra in the ultraviolet region. Figure 1 shows UV spectra of MgO(100). A distinct increase in absorption from 5.6 eV to 7.2 eV was observed for the samples treated under hydrogen, compared to an untreated sample. On the other hand, in the NEXAFS measurement, a new maximum appeared in the pre-edge area. The appearance of pre-edge peaks suggested that defects created new electronic states in the conduction band.

The results of both UV and NEXAFS indicated that a new electronic state was formed in the conduction band due to the oxygen defect produced by the hydrogen reduction treatment, which made the band gap narrower.

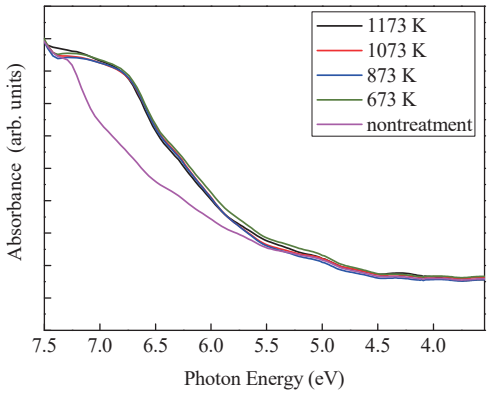

Fig. 1. UV spectra of MgO(100).

[1] D. M. Roessler and W. C. Walker, Phys. Rev. **159** (1967) 733.

[2] E. A. Colbourn, Surf. Sci. Rep. **15** (1992) 281.

[3] G. H. Rosenblatt, M. W. Rowe, G. P. Williams, Jr., R. T. Williams and Y. Chen, Phys. Rev. B **39** (1989) 10309.

[4] M. M. Freund, F. Freund and F. Batllo, Phys. Rev.Lett. **63** (1989) 2096.

BL3B

Luminescence Possibly Due to Localized Excitons in $CH_3NH_3Pb(I,Cl)_3$ Alloyed Thin Films

T. Makino and K. Waza

Depeartment of Electrical and Electronics Engineering, University of Fukui, Fukui 910-8585, Japan

Perovskite-halide semiconductors ($CH_3NH_3PbI_3$) have attracted intense research interest due to their potential applications in solar-cells. The radiative and nonradiative recombination processes between the light harvesting and the hole transport layers are very important to understand the light-electricity conversion mechanism. However, the emission mechanism which is intimately related to the abovementioned recombination in $CH_3NH_3PbI_3$ is not understood completely.

Here, we are rather interested in the optical properties of its alloyed system, namely, $CH_3NH_3Pb(I,Cl)_3$. The physical origin of spontaneous emission in $CH_3NH_3Pb(I,Cl)_3$ may be attributed to the recombination of localized excitons. No photoluminescence (PL) studies have been reported in this alloy, whereas the corresponding PL studies have been reported in unalloyed $CH_3NH_3PbI_3$. An S-shaped (red–blue–redshift) temperature dependence has been observed for the peak positions of the PL spectra even in $CH_3NH_3PbI_3$. This strongly suggests inhomogeneities in $CH_3NH_3PbI_3$. Stronger inhomogeneity is expected to exist in the alloy because of the microscopic fluctuation of the concentration. This anomalous behavior is reminiscent to what one observed in alloys or quantum structures in nitride semiconductors. Essentially, no quantitative approach has been made to interpret the temperature dependence of the PL spectra in $CH_3NH_3Pb(I,Cl)_3$.

Let us briefly review the history for the explanation of the exciton localization mechanism in nitride semiconductors. Several simulation-based studies have been performed. The band-tail-filling model has been adopted to describe the recombination of the localized excitons. However, this model failed to explain the low-temperature dynamics of excitons. Low-temperature excitonic localization has been interpreted using numerical solutions of Schrödinger equations. This numerical approach has not successfully been applied to high temperature exciton dynamics. Finally we successfully interpreted the temperature dependence based on Monte Carlo simulation of phonon-assisted exciton hopping and relaxation, considering effects of the earlier-mentioned potential fluctuations.

We are interested in the anomalous optical behaviors of $CH_3NH_3Pb(I,Cl)_3$. Whether can it be interpreted along the abovementioned model applicable for nitrides?

In this work, we currently study about the temperature dependence of the PL spectra in $CH_3NH_3Pb(I,Cl)_3$.

As a preparation of its detailed analysis, we show in Fig. 1 the PL spectrum taken in a low temperature (10 K). It should be noted that this spectrum has not been yet corrected with the instrumental function. Therefore, the final line-shape has possibility to be changed significantly during the correction.

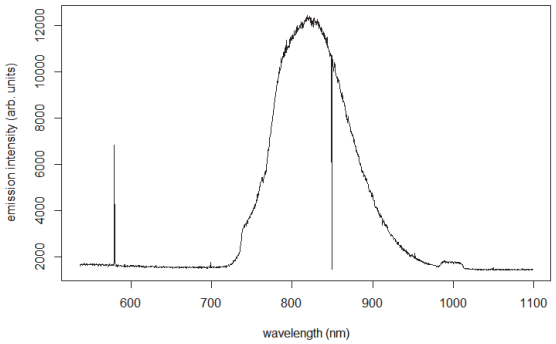

Fig. 1. Photoluminescence from alloyed thin film taken at 10 K. Excitation is made with the light source at the UVSOR Synchrotron Facility.

[1] Md. S. Hasan, Md. S. Islam, Md. R. Islam, I. M. Mehedi, T. Makino, J. Comput. Electron. **17** (2018) 373.

BL3B

Improvement of Persistent Luminescence Intensity of $Ba_2SiO_4:Eu^{2+}$ Phosphor by Lanthanide Ion Co-doping Based on VRBE Diagram

K. Asami, K. Yasuda, J. Ueda and S. Tanabe
Graduate School of Human and Environmental Studies, Kyoto University, Kyoto 606-8501, Japan

The Eu^{2+} doped barium silicate phosphors are attracting much attention in optical application for scintillation materials [1] and persistent phosphors [2]. In this study, we focused on Ba_2SiO_4 host in which Eu^{2+} doped persistent luminescence property has not been investigated. For understanding the electron transfer processes and a suitable trap ion for long persistent luminescence, a vacuum referred binding energy (VRBE) diagram is useful[3]. Thus, we constructed the diagram by the spectroscopic data obtained from photoluminescence excitation (PLE) spectra of both Ce^{3+} and Eu^{3+}- singly doped Ba_2SiO_4 phosphors. Based on the VRBE diagram, we found the suitable lanthanide ion co-dopant as a trap center for improvement of persistent luminescence intensity.

Figure 1 shows the PLE spectrum of the Ce^{3+}- doped Ba_2SiO_4 phosphor at 15 K which was measured at BL3B. In the PLE spectrum, the host exciton peak was observed at around 7.05 eV and three bands derived from Ce^{3+} were observed at 3.2-5.8 eV. From the host exciton peak, the bandgap energy was estimated to be 7.61 eV.

Figure 2 shows PLE spectrum of the Eu^{3+}- doped Ba_2SiO_4 phosphor at 10 K. The strong broad band was observed at around 4.0-7.0 eV, which is attributed to the charge transfer (CT) transition of Eu^{3+}. The CT band is deconvoluted into two bands because there are two Ba sites in Ba_2SiO_4 structure. From the peak of lower CT band shown as red curve in Fig. 2, the CT energy was estimated to be 4.40 eV.

From the obtained spectroscopic data, VRBE diagram of Ba_2SiO_4 host with 4*f* ground states of divalent and trivalent lanthanide ions was constructed as shown in Fig. 3 based on the procedure developed by Dorenbos [3].From the constructed diagram, we selected Er^{3+} ion as a trap center of Ba_2SiO_4:Eu phosphor. This is because estimated trap depth of Er^{3+} in Ba_2SiO_4 host (0.64 eV) from the VRBE diagram is similar to that of Dy^{3+} in $SrAl_2O_4:Eu^{2+}$-Dy^{3+} bright persistent phosphor (~0.60 eV)[4].

Figure 4 shows the photographs of Eu^{2+} doped (left) and Eu^{2+}-Er^{3+}codoped (right) Ba_2SiO_4 phosphors under white light (upper), UV light (middle) and without light (lower). By co-doping Er^{3+} into Ba_2SiO_4:Eu phosphor, persistent luminescence was clearly observed. Persistent luminescence duration time on 0.32 mcd/m^2 is 7 min and 3.5 h for Eu^{2+}- and Eu^{2+}-Er^{3+} co-doped Ba_2SiO_4 phosphor, respectively.

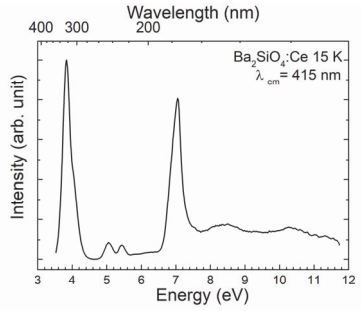

Fig. 1. PLE spectrum of $Ba_2SiO_4:Ce^{3+}$.

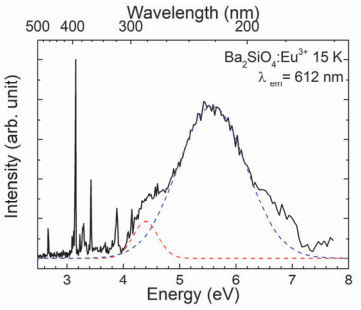

Fig. 2. PLE spectrum of $Ba_2SiO_4:Eu^{3+}$.

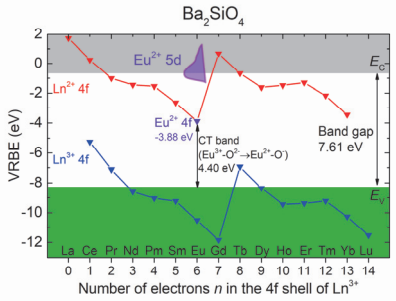

Fig. 3. VRBE diagram of Ba_2SiO_4 host.

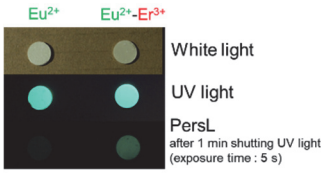

Fig. 4. Photographs of Eu^{2+} doped and Eu^{2+}-Er^{3+}codoped Ba_2SiO_4 phosphors.

[1] Y. Eagleman, *et al.,* IEEE Trans. Nucl. Sci. **59** (2012) 479.
[2] Y. Jia, *et al.,* Mater. Des. **90** (2016) 218.
[3] P. Dorenbos , J. Lumin. **135** (2013) 93.
[4] H. Takasaki, S. Tanabe and T. Hanada, J. Ceram. Soc. Japan. **104** (1996) 322.

BL4U

In-situ Studied the Oxygen 2*p*-vacancy in the TaO_x Interlayers of Resistive Switching Materials

J. W. Chiou[1], Y. F. Wang[2], W. F. Pong[2], J. S. Chen[3], T. Ohigashi[4] and N. Kosugi[4]

[1]*Department of Applied Physics, National University of Kaohsiung, Kaohsiung 811, Taiwan*

[2]*Department of Physics, Tamkang University, Tamsui 251, Taiwan*

[3]*Department of Materials Science and Engineering, National Cheng Kung University, Tainan 701, Taiwan*

[4]*UVSOR Synchrotron Facility, Institute for Molecular Science, Okazaki 444-8585, Japan*

Resistance random access memory (ReRAM) using the change in resistance between crystalline and amorphous states of a chalcogenide compound has attracted a great deal of attention for use as next-generation nonvolatile memories. The ReRAM memory cell has a capacitor-like structure composed of insulating or semiconducting materials sandwiched between two metal electrodes. Due to its simple structure, highly scalable cross-point and multilevel stacking memory structures have been proposed. In the resistive switching phenomenon, A. Sawa [1] reports that a large change in resistance (>1000%) occurs on applying pulsed voltages and the resistance of the cell can be set to a desired values by applying the appropriate voltage pulse.

In this work, we have in-situ studied the electronic structure and the location of oxygen 2*p*-vacancy in the TaO_x interlayers and identified the type of conducting path by scanning transmission x-ray microscopy (STXM) and x-ray absorption near-edge structure (XANES). During the STXM measurements, a various voltage, 0, +50, -50, 0 volts, has exerted on both ends of the Ta/TaO_x/Pt thin film, respectively, to specify the electronic structure associated with the conducting path. The amorphous TaO_x thin film of thickness of ~75 nm was deposited on Pt/SiO_2/Si substrate by electron beam evaporation method. Active electrodes of Ta were thermally evaporated respectively on the TaO_x thin film with an equivalent thickness of ~130 nm. As shown in Fig. 1, the STXM stack mapping displays the cross-sectional views of the Ta/TaO_x/Pt thin film under various applied voltages. The experiments were performed at the BL4U. The corresponding O *K*-edge STXM-XANES spectra of the Ta/TaO_x/Pt thin film were recorded at TaO_x interlayers, as shown in Fig. 2. According to the dipole-transition selection rule, the features at ~530-545 eV are attributed to the electron excitations from O 1*s* core level to O 2*p*-derived states, which are approximately proportional to the density of the unoccupied O 2*p*-derived states. The intensities of the O *K*-edge STXM-XANES spectra are significantly lower as a voltage applied on both ends of the Ta/TaO_x/Pt thin film, which reflects the decrease in the number of unoccupied O 2*p*-derived states. In other words, the STXM-XANES results demonstrate that the population of defects at the O sites in the TaO_x interlayers and intensely support the phenomena that the existence of O 2*p*-vacancy in the TaO_x interlayers plays a main role for the mechanics of charge transfer in resistive switching materials.

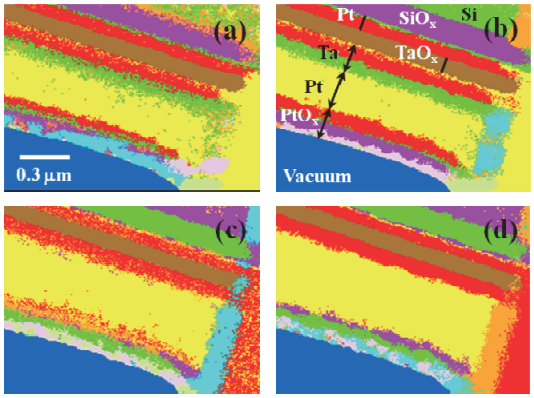

Fig. 1. The STXM stack mapping obtained in applying (a) 0, (b) +50, (c) -50, and (d) 0 volts on both ends of the Ta/TaO_x/Pt thin film, respectively.

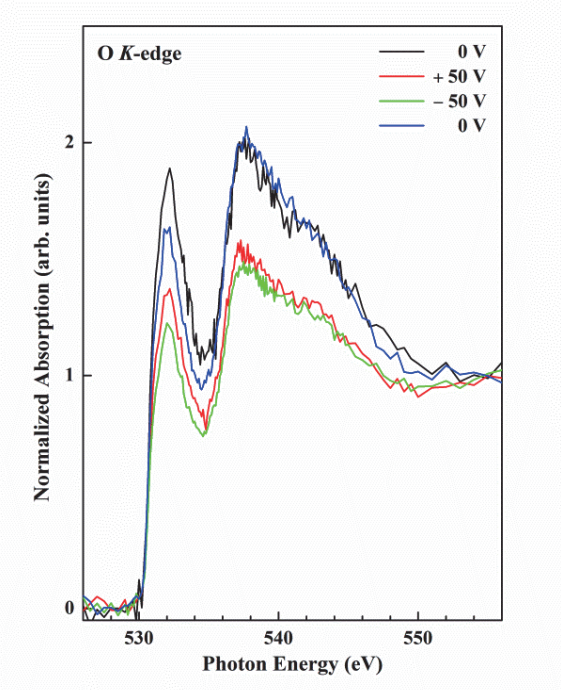

Fig. 2. The corresponding O *K*-edge STXM-XANES spectra were recorded at TaO_x interlayers under various applying voltages.

[1] A. Sawa, Materials Today **11** (2008) 28.

BL4U

Nano-Scale Chemical Mapping of Vapor Processed-$(PEA)_2(MA)_{n-1}Pb_nI_{3n+1}$ Quasi-2D Perovskite Solar Cells

H. W. Shiu[1], M. S. Li[2], L. C. Yu[1], Y. L. Lai[1], T. Ohigashi[3], N. Kosugi[3], P. Chen[2] and Y. J. Hsu[1]

[1]*National Synchrotron Radiation Research Center, Hsinchu 300, Taiwan*

[2] *Department of Photonics, National Cheng Kung University, Tainan 701, Taiwan*

[3]*Institute for Molecular Science, Okazaki 444-8585, Japan*

In the last couple years, a dimensionally tuned quasi-2D perovskite thin film was developed which is systematically synthesized by introducing a large organic cation, phenylethylammonium (PEA = $C_8H_9NH_3$) at a judiciously-chosen stoichiometry [1]. The quasi-2D perovskite exhibits the capability of combination of enhanced stability of 2D perovskite and outstanding optoelectronic properties of 3D perovskite [2]. In this work, we systematically studied the layer number dependent behavior of $(PEA)_2(MA)_{n-1}Pb_nI_{3n+1}$ Quasi-2D perovskite by X-ray photoelectron spectroscopy (XPS), Near-edge X-ray absorption fine structure (NEXAFS), and scanning transmission X-ray microscopy (STXM).

In our previous studies, we have successfully synthesized dimensional tunable quasi-2D perovskite by mixing stoichiometric quantities of lead iodide (PbI_2), MAI (Ch_3NH_3I) and PEAI to yield a series of compounds, $(PEA)_2(MA)_{n-1}Pb_nI_{3n+1}$ with different layer numbers of n. The MAI vapor-assisted method can control the morphology to achieve compact and highly stable crystalline layer. The PCEs up to 19.1% and 18.69% were achieved for n = 40 and n =60 layers compound, respectively. Both of them showed better performance than the pristine 3D perovskite of $MAPbI_3$ (PCEs = 17.31%, n = ∞) and 2D perovskite of $(PEA)_2MAPb_2I_7$ (PCEs < 15%). Besides, compare with the SEM results, it indicated that PEAI may play an important role for the photovoltaic performance, because the change of the morphology was correlated with the amount of large organic cation.

To further confirm the correlation between the morphology, photovoltaic properties and the effect of MAI vapor, chemical mapping of carbon, nitrogen and titanium in the aggregation of $SiN/TiO_2/(PEA)_2(MA)_{n-1}Pb_nI_{3n+1}$ (n =1, 2, 20, 40 and ∞) are studied by NEXAFS and STXM. Figure 1 shows the STXM OD images of n = 2, quasi-2D perovskite with and without MAI vapor treatment at 293.5 eV, which is corresponding to the C-Cσ* resonances. As shown in Fig. 1 (a), most of the areas is covered by the plump caterpillar-like perovskite films without MAI treatment. In contrast, the perovskite becomes slim and aggregating on to TiO_2 nano-structures as observed in Fig. 1 (b). Some bright spots with intense spherical shapes in carbon mapping is observed at low dose of the MAI treatments while it is not observed at higher dosage.

The corresponding micro NEXAFS spectra at carbon K-edge with circular marks in Fig. 1 are shown in Fig. 2a. Figure 2b shows the reference NEXAFS spectra of n = 1, n = 20, n = 40 and $MAPbI_3$ (n = ∞) for comparison. When the PEAI is doped into the PbI_2 film for n = 2 without MAI vapor reaction, the absorption profile along with characteristic peaks are similar to the 2D $(PEA)_2PbI_4$ perovskite (n = 1). After MAI vapor treatment, the n = 2 film starts growing in the mixture phase containing $CH_3NH_3^+$ (MA^+) cation and aggregates onto TiO_2 substrate. The spectrum is similar to the measurement of $MAPbI_3$. For lower MAI dosage, an intermediate state is observed as shown in Fig. 2a that may explain the reaction process of MAI vapor treatment.

(a) (b)

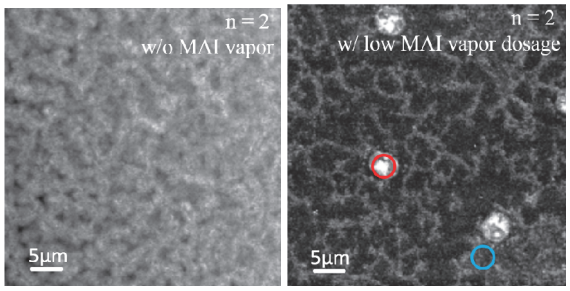

Fig. 1. C K-edge optical density images of n = 2 quasi-2D perovskite (a) without and (b) with MAI vapor treatment onto SiN/TiO_2 substrate. The carbon OD images are obtained at 293.5 eV.

(a) (b)

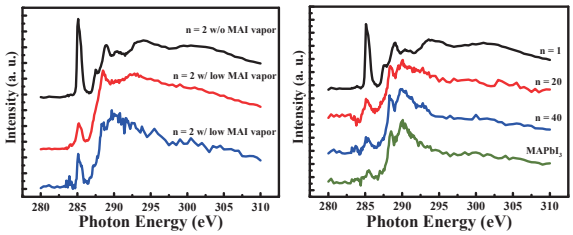

Fig. 2. (a) C K-edge spectra of n = 2 quasi-2D perovskite without (Fig.1a) and with low (Fig.1b) MAI vapor dosage. (b) C K-edge reference spectra for n =1, n = 20, n = 40 and $MAPbI_3$ (n = ∞).

[1] I. C. Smith, E. T. Hoke, D. S.-Ibarra, M. D. McGehee, H. I. Karunadasa, Angew. Chem. Int. Ed. **53** (2014) 1.

[2] L. N. Quan, M. Yuan, R. Comin, O. Voznyy, E. M. Beauregard, S. Hoogland, A. Buin, A. R. Kirmani, K. Zhao, A. Amassian, D. H. Kim, E. H. Sargent, J. Am. Chem. Soc. **138** (2016) 2649.

BL4U

Phase Evolution of Complex Metal Hydrides during De/Rehydrogenation

J. L. White[1, 2], T. Ohigashi[3], K. G. Ray[2, 4], Y.-S. Liu[2, 5], V. Stavila[1, 2], M. D. Allendorf[1, 2] and J. Guo[2, 5]

[1]*Sandia National Laboratories, Livermore, CA 94551, United States*
[2]*Hydrogen Materials–Advanced Research Consortium (HyMARC), Livermore, CA 94551, United States*
[3]*UVSOR Synchrotron Facility, Institute for Molecular Science, Okazaki 444-8585, Japan*
[4]*Lawrence Livermore National Laboratory, Livermore, CA 94550, United States*
[5]*Lawrence Berkeley National Laboratory, Berkeley, CA 94720, United States*

Lightweight complex metal hydrides are of interest for use as energy-dense on-board vehicular hydrogen stores [1]. One material of particular interest, magnesium borohydride ($Mg(BH_4)_2$), has very high hydrogen capacity, at 14.9 wt.% H, but suffers from slow kinetics and the need for extreme conditions for both dehydrogenation and rehydrogenation from magnesium diboride (MgB_2) [2]. In order to establish methods to improve the kinetic properties of this system, a greater understanding of the nucleation and growth of various solid phases is essential.

Several samples of partially dehydrogenated $Mg(BH_4)_2$ and partially hydrogenated MgB_2 were examined by Scanning Transmission X-Ray Microscopy (STXM) at the boron K-edge using the transfer system from a glovebox to BL4U to prevent oxidation upon exposure to air. The resulting series of X-ray absorption images were analyzed using computed spectra for several B containing species (Fig. 1), since the experimental XAS spectra showed substantial amounts of oxidized boron.

The STXM maps revealed some intriguing phase propagation patterns not heretofore observed. MgB_2 partially hydrogenated at 400 °C and either 200 or 700 bar H_2 over the course of 72 h (Fig. 2) showed that hydrogenation to $Mg(BH_4)_2$ began at the exterior of the particles and spread inward, with greater conversion evident at the higher pressure, as expected.

However, the $Mg(BH_4)_2$, partially dehydrogenated at 400 °C and H_2 overpressures of 200 and 360 bar, showed a much more counterintuitive phase transformation (Fig. 3). It has commonly been hypothesized that the dehydrogenated phase forms first on the outside of hydride particles as the hydride releases H_2 from the surface [3]. Instead, our STXM results on $Mg(BH_4)_2$ show that the hydride remains on the exterior, whereas the interior becomes dehydrogenated first. The higher overpressure sample decomposed less, and consequently its interior retained more of the hydride phase. Therefore, nucleation of the dehydrogenated material begins in the bulk, and hydrogen atoms diffuse toward the surface where they can combine and desorb as H_2 gas. Information regarding the phase evolution in in the Mg-B-H system provides valuable insights into the rate-limiting step of hydrogen desorption.

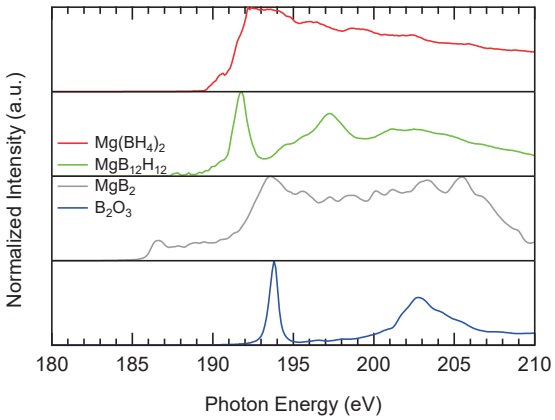

Fig. 1. Simulated B K-edge XAS spectra of relevant chemical species used in STXM analyses.

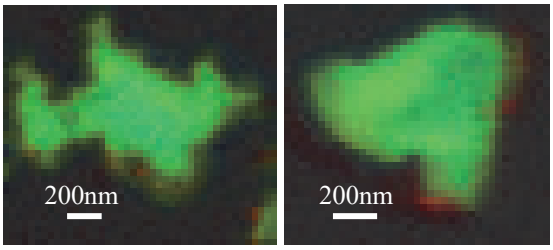

Fig. 2. STXM maps of MgB_2 hydrogenated for 72 h at 400 °C and (a) 200 or (b) 700 bar H_2. Red indicates $Mg(BH_4)_2$, green $MgB_{12}H_{12}$, and blue B_2O_3.

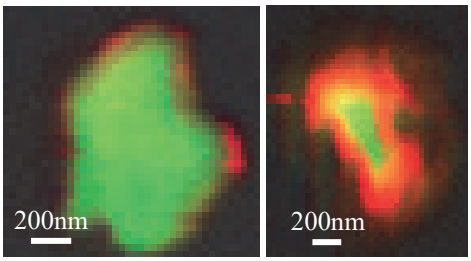

Fig. 3. STXM maps of $Mg(BH_4)_2$ dehydrogenated for 72 h at 400 °C and H_2 overpressures of (a) 200 and (b) 360 bar H_2. Red indicates $Mg(BH_4)_2$, green $MgB_{12}H_{12}$, and blue B_2O_3.

[1] S.-i. Orimo *et al.*, Chem. Rev. **107** (2007) 4111.
[2] K. G. Ray *et al.*, Phys. Chem. Chem. Phys. **19** (2017) 22646.
[3] B. C. Wood *et al.*, Adv. Mater. Interfaces **4** (2017) 1600803.

BL4U

Probing the Electronic Structure of $BiVO_4$ Coated ZnO Nanodendrite Core - Shell Nanocomposite Using Spatially Resolved Scanning Transmission X-ray Microscopy Studies

M. M. Shirolkar[1], J.-W. Chiou[2], T. Ohigashi[3], N. Kosugi[3] and W.-F. Pong[1]
[1]*Department of Physics, Tamkang University, Tamsui 251, Taiwan*
[2]*Department of Applied Physics, National University of Kaohsiung, Kaohsiung 811, Taiwan*
[3]*Institute for Molecular Science, Okazaki 444-8585, Japan*

Recently, it has been reported that ZnO nanodendrites (NDs) coated with $BiVO_4$ nanolayers core-shell nanocomposite thin film structure forms a multiple-level hierarchical heterostructure, which is remarkably beneficial for light absorption and charge carrier separation for the competent photoelectrochemical (PEC) properties compared to their individual counterparts [1]. As PEC properties are essentially a function of band alignment and atomic – electronic structures, we studied the nanocomposite thin film using various X-ray spectroscopic and microscopy studies. We have probed the origin and nature of localized electron states in core-shell structures using valance band spectroscopy, X-ray absorption spectroscopies and spatially resolved scanning transmission X-ray microscopy (STXM). The valance band studies show band alignment at the core-shell interface, which allows efficient charge transfer between heterostructure. While, X-ray absorption studies essentially show that in core-shell structure tetrahedral environment of V^{5+} in $BiVO_4$ is unusually distorted and the inter-band gap states related to another valence state of vanadium, namely, V^{4+} is present. The presence of multiple valance states of vanadium gives favorable conditions for small polaron formation in $BiVO_4$, thereby degrading PEC activities. However, it was observed that V^{4+} coordinates with ZnO lattice thereby giving rise to conditions similar to vanadium doped ZnO. These studies reveal electronic structure over few micrometers length scale within the thin film, which contains hundreds of nanostructures and precise locations of the coordination within individual nanostructure remain unrevealed. Moreover, high-resolution transmission electron microscopy - electron energy loss spectroscopy could not effectively resolve above-mentioned coordination features.

On the other hand, STXM is powerful technique and retains the ability to efficiently resolve the observed coordination features efficiently within single or cluster of nanocomposite structure because of its high spatial resolution features [2]. Figure 1 depicts STXM results obtained on the core – shell nanostructure. With STXM measurements, we able to probe core-shell coordination and the sites in ZnO NDs contributing to V^{4+} doped ZnO within single nanocomposite structure. Consequently, our STXM investigations strongly support our other synchrotron measurements.

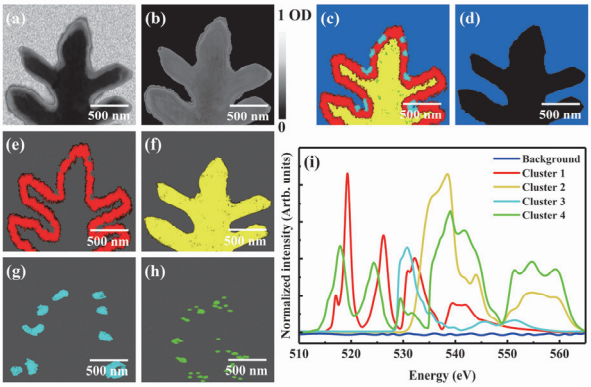

Fig. 1. (a) shows transmission electron microscope micrograph of $BiVO_4$ coated ZnO nanodendrite core-shell nanostructure, (b) shows magnified STXM optical image of core-shell nanodendrite highlighted in (a), (c) – (h) shows STXM mapping of O – K edge representing various coordination among core and shell structures: Bi – V – O (red), Zn – O (yellow), Bi – O (cyan) and Zn – V – O (green) and (i) represents O – K edge spectra obtained on various clusters.

[1] J.-S. Yang and J.-J. Wu, Nano Energy **32** (2017) 232.

BL4B

X-ray Irradiation Effect on the Local Structural Modification in Charge Transfer Salts (BEDT-TTF)$_2$X

T. Sasaki
Instutute for Materials Research, Tohoku University, Sendai 980-8577, Japan

It has been known that X-ray irradiation to the organic materials causes molecular defects and disorders. We have investigated the X-ray irradiation effect widely in the series of molecular materials κ-(BEDT-TTF)$_2$X showing superconductivity or Mott insulating state from the viewpoint of the relation between the correlated electronic states and disorders [1, 2]. The experimental and theoretical investigations suggest that the -CN parts in the anion molecules X are mainly damaged and the modification of the local structure may occur.

In this study, we investigated the soft X-ray absorption spectra in the nitrogen K-edge region for the anion layers X of the charge transfer salts of (BEDT-TTF)$_2$X with X = Cu[N(CN)$_2$]Br, Cu$_2$(CN)$_3$ and RbZn(SCN)$_4$. X-ray irradiation to the crystals was done by using the tungsten tube with 40 kV, 20 mA at room temperature. The dose amount was controlled by the irradiation time. BL4B soft X-ray beamline was used for X-ray Absorption Near Edge Structure (XANES) spectroscopy measurements in the nitrogen K-edge region. The spectra were taken by means of the total electron yield method using EM at room temperature.

Figure 1 shows the nitrogen K-edge XANES spectra around 400 eV for (a) the non-irradiated pristine and (b) 500 hours X-ray irradiated κ-(BEDT-TTF)$_2$Cu$_2$(CN)$_3$. The angle θ indicates the soft X-ray incidence angle from the a*-axis in the a*-(b+c) plane. The structure of anion molecules and the configuration to the incident soft X-ray beam are shown in Fig. 2. In the spectra, several absorption peak structures originating from the nitrogen atoms are observed. The major sharp A and broad B peaks can be attributed to the π* and σ* orbitals, respectively, coupled to the carbon or cupper atoms in the anion molecule layer. The peak intensity of A and B show characteristic dependence of the incident beam angle θ, which should contain the information of the local bonding structure around the nitrogen atoms. In these results, we found that the incident beam angle dependence changes in the X-ray irradiated crystals. These observations clearly show that X-ray irradiation causes the local modification of the anion structure around the nitrogen. The details are under analysis in parallel with the comparison to the results of the other compounds with X = Cu[N(CN)$_2$]Br and RbZn(SCN)$_4$.

[1] T. Sasaki, Crystals **2** (2012) 374.
[2] L. Kang, K. Akagi, K. Hayashi and T. Sasaki, Phys. Rev. B **95** (2017) 214106.

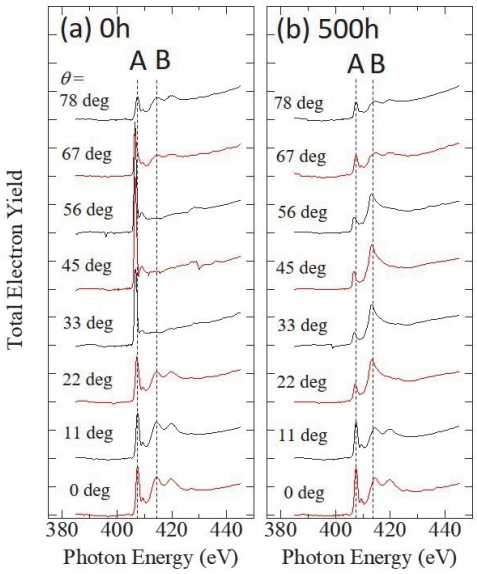

Fig. 1. Nitrogen K-edge XANES spectra of (a) non-irradiated pristine and (b) 500 hours X-ray irradiated κ-(BEDT-TTF)$_2$Cu$_2$(CN)$_3$. The angle θ indicates the incidence angle from the a*-axis in the a*-(b+c) plane.

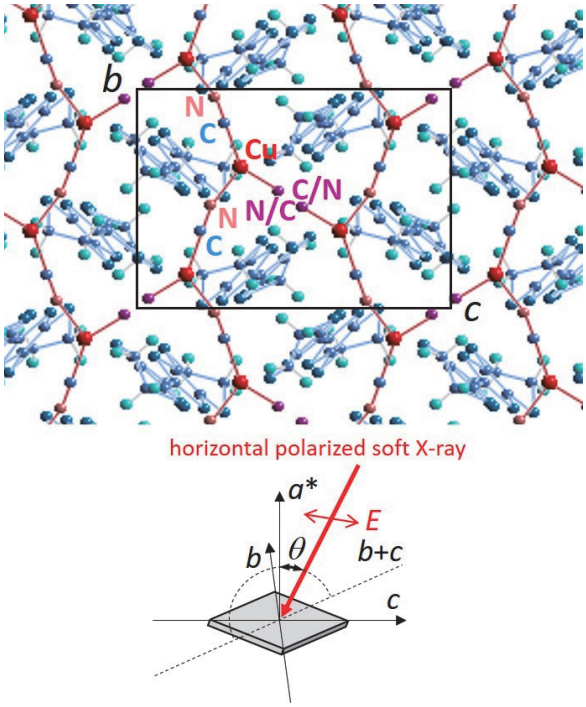

Fig. 2. The anion Cu$_2$(CN)$_3$ structure from the view along the long direction of BEDT-TTF molecule.

BL4B

Preparation of TiO_2 Film Photocatalysts for Effective Nitrogen Doping to Provide Visible Light Response

T. Yoshida[1], S. Niimi[2], M. Yamamoto[2], Y. Kato[3], A. Ozawa[3] and S.Yagi[4]

[1] *Advanced Research Institute for Natural Science, Osaka City University Osaka 558-8585, Japan*

[2] *Graduate School of Engineering, Nagoya University, Nagoya, 464-8603, Japan*

[3] *Graduate School of Engineering, Osaka City University, Osaka 558-8585, Japan*

[4] *Institute of Materials and Systems for Sustainability, Nagoya University, Nagoya 464-8603, Japan*

Photocatalytic reactions at the surface of titanium dioxide (TiO_2) under UV light irradiation have been attracting much attention in view of their practical applications to environmental cleaning such as self cleaning of tiles, glasses, and windows. Recently, Asahi *et al.* reported that the doping of nitrogen into TiO_2 contributes to band gap narrowing to provide visible-light response.

The photocatalysis of TiO_2 and nitrogen-doped TiO_2 are derived from the formation of photogenerated electrons and holes. Therefore, from a perspective of the improvement of photocatalytic properties of TiO_2, the effective depth (TiO_2 thickness) in which the electron-hole pairs capable to diffuse and contribute photocatalysis at the surface should be determined.

In the present work, we employed a pulsed laser deposition (PLD) method to fabricate the TiO_2 thin film and tried to estimate the effective depth by comparison of photocatalytic activities for TiO_2 film samples with various thicknesses. In addition, we tried to dope nitrogen into the effective depth region of TiO_2 by nitrogen implantation method, and investigated the chemical states of nitrogen effective for the visible light response of a TiO_2 photocatalyst by XAFS analysis.

Thickness-controlled TiO_2 film samples were fabricated on the (001)-face of $LaAlO_3$ or $(LaAlO_3)_{0.3}$-$(SrAl_{0.5}Ta_{0.5}O_3)_{0.7}$ single-crystal insulator substrates by a pulsed laser deposition (PLD) with a KrF excimer lazer at 973 K in an atmosphere with oxygen pressure of 5 Pa.

High-resolution X-ray diffraction measurements revealed that the deposited TiO_2 thin films on the substrates are highly (001)-oriented crystalline phase of anatase TiO_2. TEM and SIMS measurements confirmed the formation of homogeneous TiO_2 thin films. The thicknesses of the TiO_2 thin film samples have been estimated as 3, 10, 16, 19, 30 and 59 nm. We also have prepared a thick anatase TiO_2 film with the thickness of 167nm as a reference bulk sample.

The prepared TiO_2 film samples promoted photocatalytic degradation of methylene blue (MB) under UV-light irradiation. Decrease of MB concentration well obeyed the first-order kinetics, and the reaction rate constant was calculated. The reaction rate constant increased with increasing the TiO_2 thickness up to 10 nm. Then, it decreased until the thickness becomes ca. 30 nm, followed by staying constant. Thus, it is notable that the 10 nm thickness of TiO_2 on the insulator substrate would be the optimum structure.

We also doped nitrogen into the effective depth region (ca. 10 nm) of TiO_2 by 5 keV N^+ implantation and the nitrogen doped TiO_2 samples promoted photocatalytic degradation of MB under visible-light irradiation. Figure 1 shows N K-edge XANES spectra of a TiN powder, the photocatalytic active and inactive samples. The XANES profile of the active sample was well reproduced by the theoretical prediction using FEFF code when N occupies one of the O sites of TiO_2. On the other hand, the XANES spectrum of the inactive sample showed a distinct single peak around 401 eV. This peak could be empirically attributed to formation of NO_2 species.

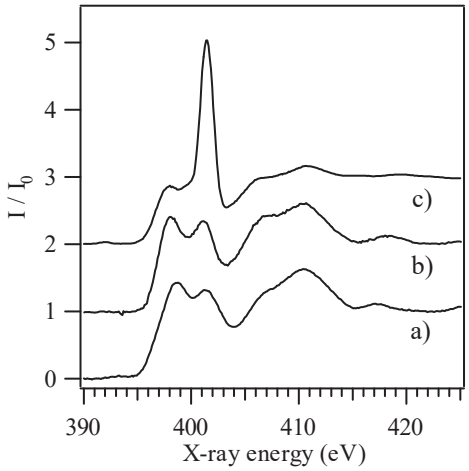

Fig. 1. N K-edge XANES spectra of (a) TiN, (b) the photocatalytic active sample and (c) the photocatalytic inactive sample.

[1] A. Fujishima, X. Zhang and D. A. Tryk, Surf. Sci. Rep. **63** (2008) 515.

[2] R. Asahi, T. Morikawa, T. Ohwaki, K. Aoki and Y. Taga, Science **293** (2001) 269.

[3] T. Yoshida and E. Kuda, Stud. Surf. Sci. Catal., T. Yoshida and E. Kuda, Stud. Surf. Sci. Catal. **175** (2010) 267.

BL4B

Valence State Analysis of Mn Ions in Mg_2TiO_4 and Mg_2SnO_4

T. Yamamoto[1, 2] and K. Akiya[1]

[1]*Faculty of Science and Engineering, Waseda University, Tokyo 169-8555, Japan*

[2]*Institute of Condensed-Matter Science, , Waseda University, Tokyo 169-8555, Japan*

Phosphor materials are widely studied because of their useful application for industrial use. Doping technique, i.e., incorporation of new elements in the host materials, have been widely employed to synthesize an effective phosphors, in which rare-earth elements have been often used as dopants. Recently, rare-earth free phosphors has become a new target, in which Mn has been selected as an emission center for the red-emitting phosphor. Although it is essential to know the charge state of the doped Mn ions for the understanding of emission spectra and efficiency, most of the research did not reveal it. In the current study, Mn doped Mg_2TiO_4 and Mg_2SnO_4 have been synthesized and the valence states of Mn ions in these materials were investigated by the Mn-L XANES measurements.

Mn doped Mg_2TiO_4 and Mg_2SnO_4 were synthesized by the solid state reaction method, in which high purity powders of MgO, TiO_2, SnO_2 and Mn_2O_3 were used for starting materials. Concentrations of doped Mn are 0, 0.005, 0.1, 0.05 and 0.1 with respect to Ti or Sn. The crystal structures of all the synthesized powders were examined by the conventional powder X-ray diffraction technique, which suggested all the samples crystallized in a single-phased spinel structure. The photoluminescence spectra of these synthesized materials were measured, in which Mn-doped Mg_2TiO_4 and Mg_2SnO_4 showed red and green emissions, respectively, as shown in Fig. 1. XANES spectra at Mn L-edge were collected at BL4B in UVSOR with the total electron yield method. Incident beam was monochromatized by the varied-space grating (800 l/mm). Samples were attached on the carbon adhesive tape, which were put on the first Cu-Be dinode of the electron multiplier.

Observed Mn-L_3 XANES spectra of Mn-doped Mg_2TiO_4 and Mg_2SnO_4 are shown in Fig. 2 with those of standard Mn compounds. It is widely accepted that the Mn-L XANES profile is sensitive to change in charge states and fingerprint type analysis is possible. As shown in this figure, spectral profile of Mn-doped Mg_2TiO_4 and Mg_2SnO_4 are different, which suggest charge states of Mn ions in these two host materials are different. From the comparison of the profiles with those of standard materials, that of Mn-doped Mg_2TiO_4 shows similar profiles as that of MnO_2, which suggests majority of the doped Mn ion is 4+ in Mg_2TiO_4. On the other hand, the profile of Mn-doped Mg_2SnO_4 seems to be derived mainly from Mn^{2+}. These charge states of Mn ions in Mg_2TiO_4 and Mg_2SnO_4 deduced from the XANES results can explain their emission colors, i.e., red and green emissions.

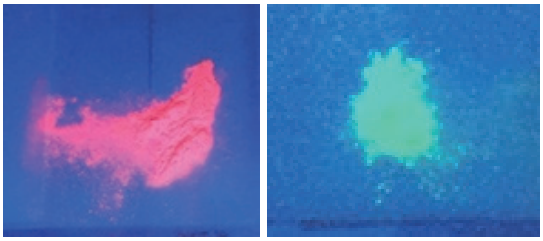

Fig. 1. Photograph of red (left) and green (right) emissions from Mn doped Mg_2TiO_4 and Mg_2SnO_4, respectively, by UV irradiation.

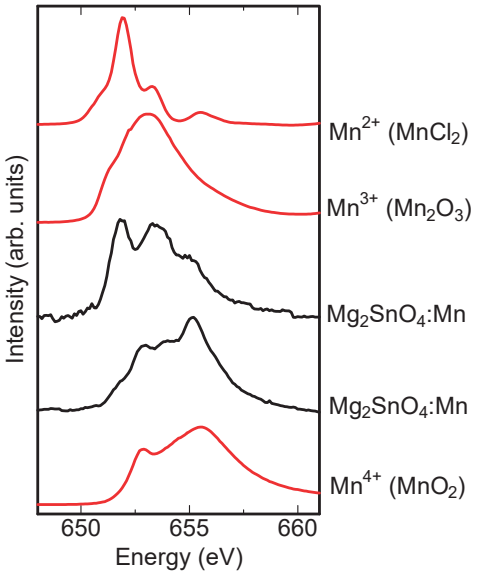

Fig. 2. Observed Mn-L_3 XANES spectra of $MnCl_2$ (Mn^{2+}), Mn_2O_3 (Mn^{3+}), Mn-doped Mg_2SnO_4, Mn-doped Mg_2TiO_4 and MnO_2 (Mn^{4+}). Mn concentration in Mg_2TiO_4 and Mg_2SnO_4 are 0.05.

BL4B

Evaluation of Chemical State of Nitrogen in Nitrided Alloy by Soft X-ray Spectroscopy

M. Sato and S. Matsumoto
Institute for Materials Reseach, Tohoku University, Sendai 980-8577, Japan

Machinery structural materials such as gears, shafts and molds are required to have high surface hardness and high toughness because of the severe friction and/or abrasion at the surface.

Nitriding is a surface hardening technique widely used industrially and flows nitrogen from the surface and combining with strong nitride forming elements (for example, Al, Cr, V, Ti, etc.) contained in steel to precipitate clusters and alloy nitrides at near the surface. Compared to other surface hardening methods such as carburizing and shot peening, the nitriding has advantages of less strain because it does not involve phase transformation and deformation during treatment. Therefore, the importance of nitriding process is increasing in recent high-precision materials. In the nitriding treatment, a sufficient amount of nitrogen flows in the vicinity of the surface to precipitate the alloy nitride at the initial stage of nitriding, whereas precipitation is delayed at the inside of the sample because it takes long time for the nitrogen diffusion. As a result, the concentration gradient of nitrogen is formed in a sample.

In this research, we aimed to investigate whether such gradient change of nitrogen can be captured by XAFS method. Since this measurement is our first beam time at BL4B, it is also an important object to acquire how to use the devices and to obtain the correct data.

A sample with a nitrogen concentration gradient from the surface to the inside was prepared by plasma nitriding treatment at 550 °C for 16 hours using the Fe-0.5V-1.5Al alloy. In addition, nitrogen martensite steel including 0.3, 0.5 and 2 mass% N prepared by nitriding and quenching (N-Q) treatment using the pure iron, and the γ'-Fe_4N and the BN powder were used as reference materials.

XAFS measurement was carried out at the BL4B, and the N-K edge (380 ~ 450 eV) and the Fe-L edge (700 ~ 760 eV) XANES spectra were collected by the total electron yield method, respectively. Since the SDD detector had been out of order, we could not measure by fluorescence method during beam time. The measurement time was kept to 30 minutes for one scan. The measurement on the low concentration sample was performed a plurality of times, and the obtained spectrum was merged.

In the measurement of the Fe-L edge, the similar spectrum to pure iron was obtained for all bulk samples, and it had the same shape as the spectrum reported in various papers. Therefore, it is considered that acquisition of measurement method was carried out without problems. On the other hand, the XANES spectrum obtained from the Fe_4N powder had the same shape as the Fe_2O_3, suggesting the possibility that the surface is oxidized. Since Fe_4N sample was extracted from tempered N-Q sample, it is necessary to pay attention to handling and storage conditions in the future.

Figure 1 shows the N-K edge XANES spectra of samples. Since the SDD detector could not be used in this beam time, low concentration samples could not measure. Therefore, only the spectrum of the relatively high nitrogen concentration of BN, Fe_4N and 2mass%N alloy are shown. It was also confirmed that the obtained spectrum of BN powder was similar to that previously reported one [1].

The nitrogen atom in the N-Q treated sample is considered to be in a solid solution state. However, spectrum of nearly the same shape with Fe_4N was obtained. Therefore, further investigation is necessary in combination with simulation using FEFF code in the next time.

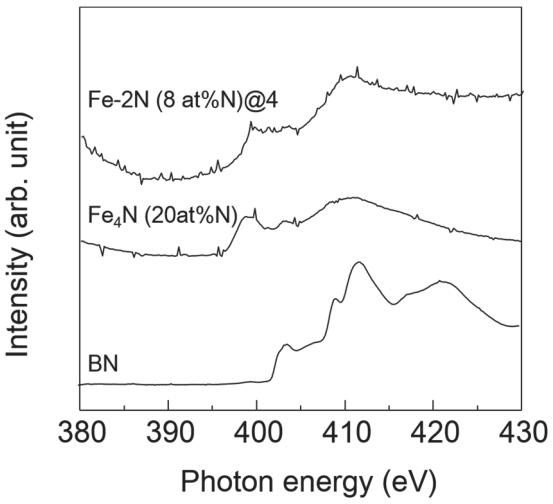

Fig. 1. N-K edge XANES spectra of BN, Fe_4N and N-Q treated Fe specimen.

[1] L. Liu *et al.*, Phys. Chem. Chem. Phys. **15** (2013) 6929.

BL5U

High-Resolution ARPES Study of $TaSe_2$ Atomic-Layer Ultrathin Film

Y. Nakata[1], K. Sugawara[2, 3], T. Yoshizawa[1], T. Nakamura[1], H. Oinuma[1], T. Takahashi[1, 2, 3] and T. Sato[1, 3]

[1]*Department of Physics, Tohoku University, Sendai 980-8578, Japan*
[2]*WPI Research Center, Advanced Institute for Materials Research, Tohoku University, Sendai 980-8577, Japan*
[3]*Center for Spintronics Research Network, Tohoku University, Sendai 980-8577, Japan*

Atomic-layer materials (single-layer nano-sheet in the thinnest limit of bulk layered materials) have been a target of intensive investigations since they exhibit novel physical phenomena related to the degree of freedoms in electrons such as charge, orbital, spin, and valley. Amongst layered bulk materials, transition metal dichalconenide (TMD) $NbSe_2$ has attracted considerable attention more than half century because of the coexistence of superconductivity and charge density wave (CDW). On the other hand, atomic- layer $NbSe_2$ show physical properties distinct from the bulk counterpart, such as two-dimensional superconductivity with the giant enhancement of upper-critical magnetic field due to spin-momentum locking at the Brillouin zone corners (K and K') in the electronic state arising from the strong spin-orbit coupling and the breaking of space inversion symmetry [1]. However, the physical properties such as the transport properties and the electronic state in single-layer $TaSe_2$ (the same family as IV group with spin-orbit interaction stronger than that of $NbSe_2$) has not been experimentally reported yet, desipite theoretical studies [2].

In this study, we carried out high-resolution angle-resolved photoemission spectroscopy (ARPES) on single-layer $TaSe_2$ grown on bilayer graphene substrate. By utilizing energy-tunable photons from synchrotron radiation, we determined the overall VB structure and Fermi surface of single-layer $TaSe_2$.

Monolayer $TaSe_2$ films were grown on bilayer graphene by using MBE system constructed at Tohoku University. Bilayer graphene was fabricated by annealing Si-terminated 6H-SiC(0001) single crystal. Monolayer $TaSe_2$ films were grown by evaporating Ta on the bilayer-graphene/SiC substrate in Se atmosphere. The as-grown film was annealed at 450 °C for 30 min. Then, we additionally deposited Se atoms on monolayer $TaSe_2$ films to protect the surface from the atmosphere. Se-capped monolayer $TaSe_2$ films was then installed to a preparation chamber at BL5U and the Se capping-layer was removed by radiation heating.

Figure 1(b) shows the ARPES-intensity plot at Fermi energy (E_F) as a function of 2D wave vectors measured along the ΓKM direction at $h\nu$ = 50 eV with linear polarization. We clearly find a large hole-like Fermi surface (FS) centered at the Γ point of both first and second Brillouin zone, indicating the well-ordered samples. Around the M point of the second Brillouin zone, a small FS with the strong intensity which is assigned as the π* band of bilayer graphene, was found. On the other hand, the spin-polarized FSs which are theoretically expected around the K point are not clearly observed because of the matrix-element effect. Figures 1(c) and (d) show the valence-band structure along the Γ-M and the Γ-K cuts. The energy band with the top of 1 eV at the Γ point and the metallic band near the Fermi level can be found along both Γ-M and the Γ-K cuts. Although the theoretical calculation has predicted the spin-split band at the Γ-K cut due to protection with the mirror symmetry at the Γ-M cut [2], it is unclear from the present expeirment that whether such band splitting exists or not, likely because of the quite small domain sizes of our films.

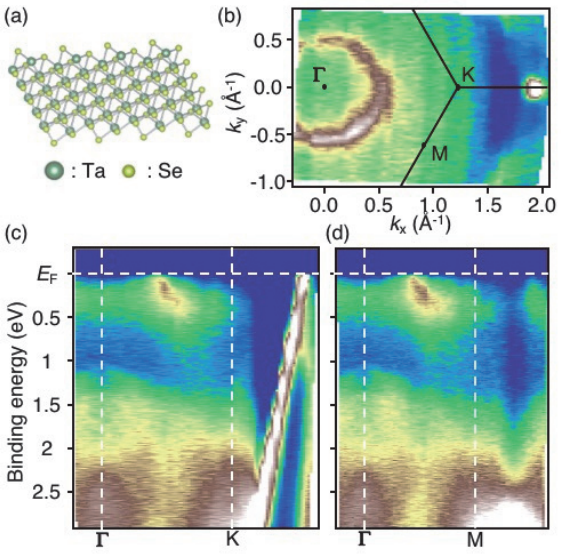

Fig. 1. (a) Crystal structure of monolayer $TaSe_2$. (b) Plot of ARPES intensity at E_F as a function of 2D wave vector measured at T = 40 K along the ΓM cut with linearly polarized 50 eV photons. (c) and (d) ARPES intensity plots in the VB region measured at T = 40 K along the Γ–M and the Γ–K line with linearly polarized 50 eV photons, respectively.

[1] X. Xi *et al.*, Nat. Phys. **12** (2016) 139.
[2] J. -A. Yan *et al.*, Sci. Rep. **5** (2015) 16646.

BL5U

Search for Nematicity in the Cuprate Superconductor $YBa_2Cu_3O_y$ by Angle-Resolved Photoemission Spectroscopy

S. Nakata[1], K. Koshiishi[1], K. Hagiwara[1], C. Lin[1],
S. Ideta[2], K. Tanaka[2], T. Nishizaki[3] and A. Fujimori[1]

[1]*Department of Physics, University of Tokyo, Tokyo 113-0033, Japan*
[2]*UVSOR Synchrotron Facility, Institute for Molecular Science, Okazaki 444-8585, Japan*
[3]*Department of Electrical Engineering, Kyushu Sangyo University, Fukuoka 813-8503, Japan*

In cuprate superconductors, to understand the origin of the pseudogap region in the phase diagram remains a most significant issue. Recently, experimental evidence for several kinds of order (e.g. charge density wave, spin density wave, nematic order) has been reported in the pseudogap region [1]. Nematicity, which does not break the translational symmetry but breaks the fourfold rotational symmetry of the lattice, has been reported below the pseudogap temperature and may play an important role in the pseudogap region [2]. For instance, evidence for nematicity appeared in $YBa_2Cu_3O_y$ (YBCO) from transport [3,4], neutron scattering [5] and magnetic susceptibility [6] measurements and in $Bi_2SrCaCu_2O_{8+\delta}$ from resistivity measurement [7].

Nematicity has been discussed also in Fe-based superconductors [8] and studied by angle-resolved photoemission spectroscopy (ARPES) [9], which is the most direct way to reveal the electronic structure. However, at the moment, there has been no report that reveals the nematicity in cuprates by ARPES. We performed ARPES measurements in order to study the nematicity in cuprates. Furthermore, by ARPES one can investigate whether the nematicity is specific to the pseudogap state or remains in the superconducting state.

YBCO single crystal samples were grown by the flux method. It was nearly optimally doped sample and T_c and T^* were 92 K and 180 K, respectively. ARPES measurements were carried out at UVSOR BL5U. We used linearly polarized light with $h\nu$ = 57.1 eV. The total energy resolution was set at 32 meV. The samples were cleaved *in-situ* under the pressure of ~ 2×10^{-8} Pa.

Figure 1 shows Fermi surface mapping at the Fermi level taken at various temperatures. Figure 2 shows energy distribution curves (EDCs) around $\boldsymbol{k}$ = (-π, 0) (X point) and (0, π) (Y point). As one can expect from the symmetry of the CuO_2 plane, the difference between EDCs around the X and Y points can be seen throughout all temperatures. So far, it is difficult to identify whether this anisotropy originate from nematicity or merely from the anisotropy of the crystal structure although the difference seems to depend on temperature. More detailed measurements with many temperatures especially in the pseudogap state are necessary.

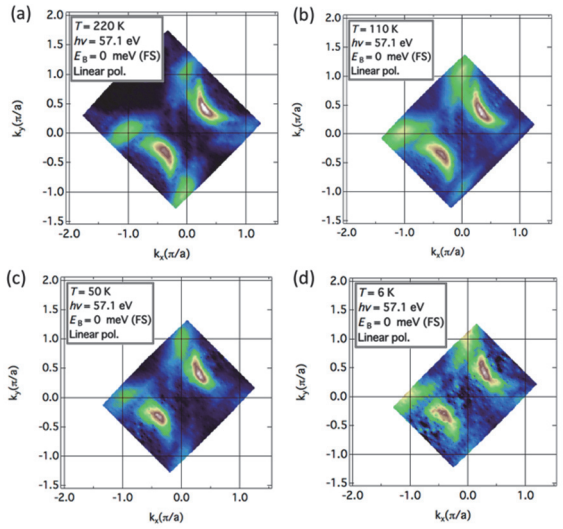

Fig. 1. Fermi surface mapping integrated over ±10 meV of the Fermi level taken at (a) 220 K, (b) 110 K, (c) 50 K and (d) 6 K, respectively.

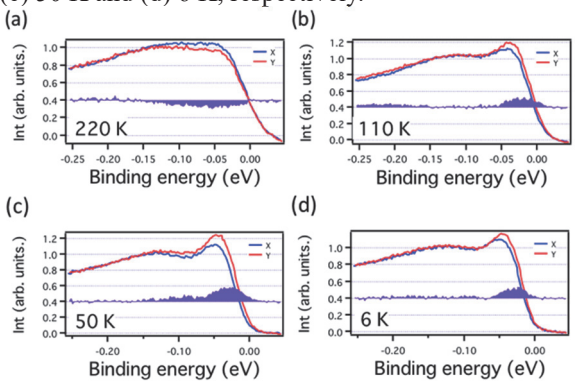

Fig. 2. EDCs of YBCO at various temperatures. Each EDC has been integrated from k_x = -1. 2 to -0. 75 (from k_y = 0. 75 to 1. 2). The difference between the lineshape of EDCs around the X and Y points are also shown.

[1] B. Keimer *et al.*, Nature **518** (2015) 179.
[2] S. A. Kivelson *et al.*, Nature **393** (1998) 550.
[3] Y. Ando *et al.*, Phys. Rev. Lett. **88** (2002) 137005.
[4] R. Daou *et al.*, Nature **463** (2010) 519.
[5] V. Hinkov *et al.*, Science **319** (2008) 597.
[6] Y. Sato *et al.*, Nat. Phys. **13** 1074 EP (2017).
[7] K. Ishida *et al.*, JPS fall meeting (2016) 14pJC-12.
[8] S. Kasahara *et al.*, Nature **486** (2012) 382.
[9] M. Yi *et al.*, PNAS **108** (2011) 6878.

BL5U, BL7U

Electronic Structure of a Bi Atomic Chain on InAs(110) Surface

T. Nakamura[1], Y. Ohtsubo[2, 1], Y. Yamashita[1], S. Ideta[3], K. Tanaka[3], K. Yaji[4], A. Harasawa[4], S. Shin[4], F. Komori[4], R. Yukawa[5], K. Horiba[5], H. Kumigashira[5] and S. Kimura[2, 1]

[1]*Department of Physics, Graduate School of Science, Osaka University, Toyonaka 560-0043, Japan*
[2]*Graduate School of Frontier Biosciences, Osaka University, Suita 565-0871, Japan*
[3]*Institute for Molecular Science, Okazaki 444-8585, Japan*
[4]*Institute for Solid State Physics, The University of Tokyo, Kashiwa 277-8581, Japan*
[5]*Photon Factory, Institute of Materials Structure Science, High Energy Accelerator Research Organization (KEK), Tsukuba 305-0801, Japan*

Low dimensional electronic structures on a solid surface has been studied extensively, such as Rashba-type spin split states due to the space-inversion asymmetry [1], and non-Fermi liquid electrons in one-dimensional (1D) metal [2, 3]. In this study, to investigate the 1D state with spin splitting due to Rashba effect, we have observed the surface electronic structures of Bi/InAs(110)-(2×1) by angle-resolved photoelectron spectroscopy (ARPES). The Bi atoms on an InAs(110) substrate form strongly buckled zig-zag atomic chains along [$\bar{1}$10] [4]. This quasi-1D (Q1D) structure formed by heavy Bi atoms, which would play an important role for Rashba effect on this surface due to its strong spin-orbit interaction, is a good candidate for a research about Rashba-type spin splitting in 1D surface states.

The InAs(110) surface was prepared by cleaving the side face of the InAs(001) wafer in an ultra-high vacuum chamber. Then, a Bi layer with the thickness of ~5 monolayers was evaporated from a Knudsen cell at room temperature. After annealing at 563 K for 15 minutes, a (2×1) periodic structure was observed, consistent with an earlier report [4]. The surface electronic structure of Bi/InAs(110) was observed at BL5U and 7U of UVSOR-III.

Figure 1 shows the ARPES constant energy contour at a binding energy at 700 meV measured with polarized photons at 85 eV. k_x (k_y) is defined parallel to [001] ([$\bar{1}$10]). The contour shows quasi-1D shape along k_x direction. A waving feature along k_y in Fig. 1 indicates a finite inter-chain interaction.

Figure 2 displays the second derivative ARPES intensity plot along k_y at the k_x point indicated by the dashed line in Fig. 1. A pair of the hole bands lies slightly below the Fermi level, indicating almost metallic but semiconducting electronic structure. Photon-energy-dependent ARPES data (not shown here) suggest that the hole bands are surface states because of no photon energy dependence.

Assuming parabolic dispersions (dashed lines in Fig. 2) with spin splitting along k_x, the size of the Rashba spin splitting is evaluated as 5.5 eV Å^{-1}. This value is the largest among other 1D and Q1D Rashba systems [5, 6] and is comparable with typical giant Rashba systems such as BiTeI and Bi/Ag surface alloys [7, 8].

The giant spin splitting in the Q1D surface state discovered here would be a promising template for future spintronic devices.

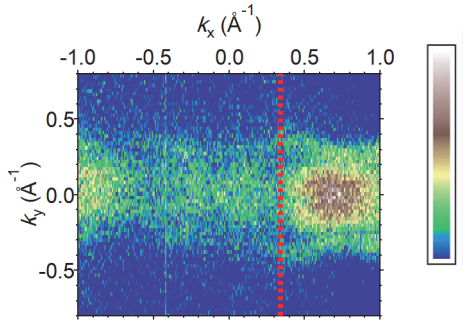

Fig. 1. A constant energy contour at the binding energy of 700 meV ($h\nu$ = 85 eV).

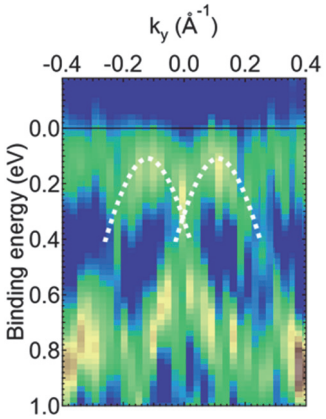

Fig. 2. Second derivative ARPES intensity plots along k_y at k_x = 0.34 Å^{-1} ($h\nu$ = 85 eV).

[1] Y. A. Bychkov and E. I. Rashba, JETP Lett. **39** (1984) 78.
[2] M. Grioni *et al.*, J. Phys.: Condens. Matter **21** (2009) 023201.
[3] C. W. Nicholson *et al.*, Phys. Rev. Lett. **118** (2017) 206401.
[4] M. G. Betti *et al.*, Phys. Rev. B **59** (1999) 15760.
[5] J. Park *et al*, Phys. Rev. Lett. **110** (2013) 036801.
[6] A. Takayama *et al.*, Phys. Rev. Lett. **114** (2015) 066402.
[7] C. R. Ast *et al.*, Phys. Rev. Lett. **98** (2007) 186807.
[8] K. Ishizaka *et al.*, Nat. Mater. **10** (2011) 521.

BL5U

ARPES Study of Transition-Metal Dichalcogenides $NbSe_2$ and NbS_2

I. Watanabe[1], K. Sugawara[2, 3], Y. Nakata[1], K. Shigekawa[1], K. Ueno[4], T. Takahashi[1, 2, 3] and T. Sato[1, 3]

[1]*Department of Physics, Tohoku University, Sendai 980-8578, Japan*
[2]*WPI Research Center, Advanced Institute for Materials Research, Tohoku University, Sendai 980-8577, Japan*
[3]*Center for Spintronics Research Network, Tohoku University, Sendai 980-8577, Japan*
[4] *Department of Chemistry, Graduate School of Science and Engineering, Saitama University, Saitama 338-8570, Japan*

Transition-metal dichalchogenides (TMDs) have attracted considerable attention since they show variety of physical properties such as magnetic ordering, charge-density wave (CDW), Mott-insulator, and superconductivity. Amongst TMDs, 2*H*-$NbSe_2$ [see Fig. 1(a)] has been intensively studied since it exhibits coexistence of CDW (T_{CDW}~33 K) and superconductivity (T_C ~ 7 K) [1], and there has been an intensive discussion on whether the CDW is the precursor of superconductivity or competes with the superconductivity. It is known that a cousin material of 2*H*-$NbSe_2$, 2*H*-NbS_2, shows the superconductivity below 5.7 K without any indication of CDW [2]. Thus, a comparative study of NbS_2 and $NbSe_2$ would enable us to clarify the interplay between the superconductivity and CDW in great detail. Very recently, it has been suggested from the theoretical calculation that the two-gap superconductivity can be realized in 2*H*-$NbSe_2$, and it could originate from strong coupling of electrons with low-energy anharmonic phonons [3]. To elucidate these important issues, electronic states of 2*H*-$NbSe_2$ and 2*H*-NbS_2 need to be investigated by angle-resolved photoemission spectroscopy (ARPES) with energy-tunable photons from synchrotron radiation.

In this study, we have performed high-resolution ARPES on 2*H*-$NbSe_2$ and 2*H*-NbS_2. By utilizing energy-tunable photons from synchrotron radiation, we determined the electronic states near the Fermi level and found that Fermi surface topology of 2*H*-NbS_2 is the same as that of 2*H*-NbS_2, while FS volume centered at the K point of 2*H*-NbS_2 is slightly smaller than that of 2*H*-NbS_2. These results play an important rule to understand the origin of CDW in TMDs.

Figures 1(b) and (c) show experimental Fermi surfaces on 2*H*-$NbSe_2$ and 2*H*-NbS_2 determined by ARPES. One can immediately recognize that the Fermi-surface topology of 2*H*-$NbSe_2$ resembles to that of 2*H*-NbS_2. The Fermi surface consists of the large pockets centered at the Γ and K points, respectively, which originate from Nb 4*d* orbitals. These Fermi surfaces commonly have hole-like character as recognized from the Fermi level (E_F) crossing of the valence band (VB) in Figs 1(d) and (e). By comparing the Fermi-surface volume between 2*H*-NbS_2 and 2*H*-$NbSe_2$, we found that a large hole pocket centered at the K point in NbS_2 is slightly larger than that in $NbSe_2$. It has been experimentally shown in bulk 2*H*-$NbSe_2$ that there exist three "hot spots" on K/K'-centered FS which are interconnected by *three* equivalent 3 × 3 CDW vectors (Q_{CDW}) [Fig. 1(b)), which enhance the electron-phonon interaction, leading to the CDW instability [4]. The present result indicates that K/K'-centered FS in 2*H*-NbS_2 is not well interconnected by 3 × 3 Q_{CDW} because of the suppression of CDW in 2*H*-NbS_2. Therefore, the present result suggests that Fermi-surface topology plays an important role to the CDW instability in TMDs.

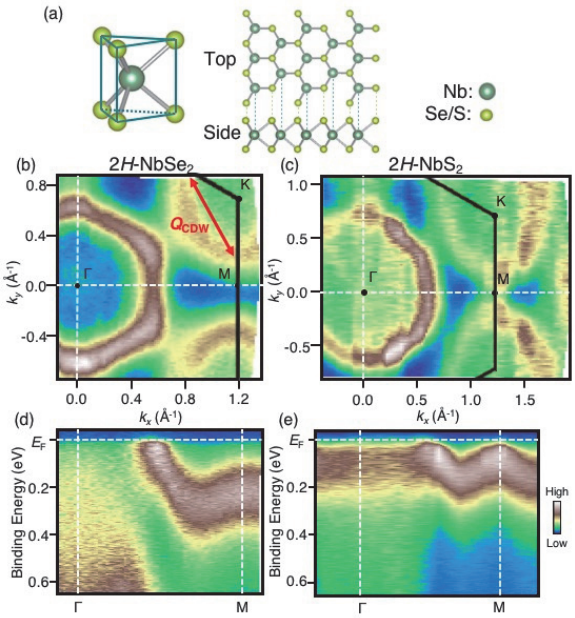

Fig. 1. (a) Crystal structure of 2*H*-$NbSe_2$ and 2*H*-NbS_2. (b) and (c) APRES intensity at E_F in 2*H*-$NbSe_2$ and 2*H*-NbS_2 plotted as a function of two-dimensional wave vector measured at *hv* = 50 and 40 eV, respectively. (d) and (e) Experimental band dispersion along the Γ-M high-symmetry line in $NbSe_2$ and NbS_2, respectively.

[1] J. A. Wilson *et al*., Adv. Phys. **24** (1975) 117.
[2] M. Naito *et al*., J. Phys. Soc. Jpn. **51** (1982) 219.
[3] C. Heil *et al*., Phys. Rev. Lett. **119** (2017) 087003.
[4] S. V. Borisenko *et al*., Phys. Rev. Lett. **102**, (2009) 166402.

BL5U

Possible CDW Effects on ARPES Spectra in the Antinodal Region of Bi2212

C. Lin[1], K. Koshiishi[1], S. Nakata[1], M. Suzuki[1], S. Ideta[2], K. Tanaka[2], D. Song[3], Y. Yoshida[3], H. Eisaki[3] and A. Fujimori[1]

[1]*Department of Physics, University of Tokyo, Tokyo 113-0033, Japan*
[2]*UVSOR Synchrotron Facility, Institute for Molecular Science, Okazaki 444-8585, Japan*
[3]*National Institute of Advanced Industrial Science and Technology (AIST), Tsukuba 305-8568, Japan*

With more and more recent observations of various symmetry-breaking orders found in the pseudogap state of high-T_c cuprates [1], the understanding of this intertwisted phase becomes increasingly important. The ubiquitous charge density wave (CDW) has been discovered in all hole-doped cuprates and even in some electron-doped cuprates, nevertheless whether CDW competes with superconductivity and whether it is related to the pseudogap are still under hot debate.

The signature of CDW-associated band folding has not been observed by angle-resolved photoemission spectroscopy (ARPES) with one exception that may be the closest—the revelation of particle-hole symmetry breaking in the pseudogap state of single-layer Bi2201, which refutes the preformed superconductivity nature of the pseudogap and suggests a possible association between the pseudogap and CDW [2]. In order to investigate whether particle-hole symmetry is broken in the bilayer Bi2212 due to possible charge ordering, we have performed temperature-dependent ARPES measurements at UVSOR BL5U.

To avoid ultra-high energy scale and complex band structure due to super-modulation, over-doped $Bi_{1.7}Pb_{0.5}Sr_{1.9}CaCu_2O_8$ (T_c = 87 K, OD87) single crystals with Pb doping were used and cleaved *in-situ* under the pressure of ~ 2 × 10^{-8} Pa. The photon energy of the incident light was 57 eV with linear polarization perpendicular to the analyzer slit and the total energy resolution was set to 20 meV. Samples were grown by the floating-zone method and the hole concentration was controlled by annealing the samples in N_2 or O_2 flow.

Figure 1 shows the temperature evolution of the antinodal electronic states. The antibonding band was enhanced by using current photon energy [3]. By ploting the peak positions of the energy distribution curves (EDCs) and summing up in Fig. 2, a clear misalignment between the Fermi momenta (k_F (±)) determined in the normal state and the band bending momenta (k_G (±)) can be observed, indicating the particle-hole symmetry breaking for OD87 Pb-Bi2212. Currently, we suppose a similar CDW nature of this broken particle-hole symmetry as in the case of Bi2201 [2,4], detailed explanation is planned in the near future.

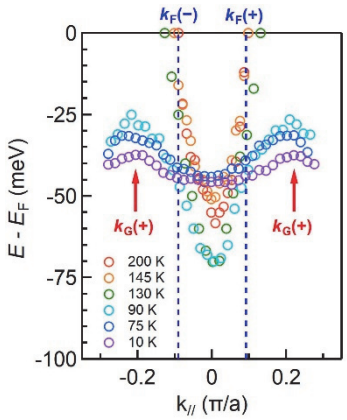

Fig. 2. Misalignment between the Fermi momenta (k_F (±)) determined in the normal state and the band bending momenta (k_G (±)) indicating the particle-hole symmetry breaking in the pseudogap state of OD87 Pb-Bi2212.

[1] R. Comin and A. Damascelli, Annu. Rev. Condens. Matter Phys. **7** (2016) 369.
[2] M. Hashimoto *et al.*, Nat. Phys. **6** (2010) 414.
[3] A. A Kordyuk *et al.*, Phys. Rev. Lett. **89** (2002) 077003.
[4] R. He *et al.*, Science. **331** (2011) 1579.

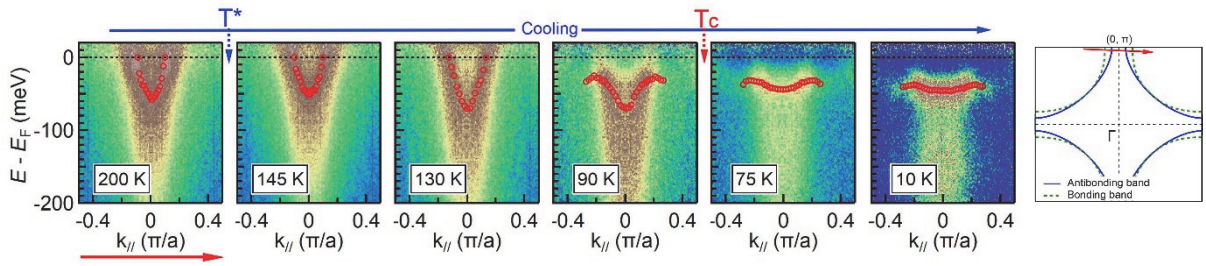

Fig. 1. Temperature evolution of the antinodal dispersions of OD87 Pb-Bi2212. The antibonding band was enhanced and the symmetrized spectra were divided by the resolution-convolved Fermi–Dirac function (FD) to effectively remove the Fermi cutoff. Red circles indicate the peak positions of the FD-EDCs and red arrow shows the cut position in the first Brillouin zone.

BL5U

Detwinned Electronic Structure of $Ba_{0.75}K_{0.25}Fe_2As_2$ Observed by ARPES

S. Ideta[1, 2], M. Nakajima[3] and K. Tanaka[1, 2]

[1]*UVSOR Synchrotron Facility, Institute for Molecular Science, Okazaki, 444-8585, Japan*

[2] *The Graduate University for Advanced Studies (SOKENDAI), Okazaki, 444-8585, Japan*

[3]*Department of Physics, Graduate School of Science, Osaka University, Toyonaka 560-0043, Japan*

Iron-based superconductors have an interesting phase diagram with the antiferromagnetic (AFM) transition and the structural phase transition. Recently, nematicity, defined as broken rotational symmetry [a trigonal(C_4)-to-orthorhombic (C_2) structural transition], has shed light on the understanding of the mechanism on the iron-based superconductivity [1-4]. In hole-doped $BaFe_2As_2$ (Ba122) system, $Ba_{1-x}Na_xFe_2As_2$ and $Ba_{1-x}K_xFe_2As_2$ (K-Ba122) have shown the magnetic order without C_4 symmetry breaking [5, 6] and the moment's direction would be swapped from in-plane to out-of-plane [7]. Besides, the superconductivity is suppressed between the superconductivity and the C_4-magnetic phase. The electronic structure at the C_4 magnetic phase has been unclear yet, and it would give us a great interest to elucidate the mechanism of the hole-doped Ba122.

Here, we demonstrated a temperature dependent angle-resolved photoemission spectroscopy (ARPES) experiment to elucidate the electronic structure of detwinned K-Ba122 ($x \sim 0.25$) with the C_4-magnetic phase in order to prevent from two domains in the orthorhombic (C_2) phase below the structural and AFM transition temperatures ($T_{N,S} \sim 60$ K).

High-quality single crystals of $Ba_{0.75}K_{0.25}Fe_2As_2$ ($T_c \sim 25$ K) were grown by self-flux technique. ARPES experiments were carried out at BL5U of UVSOR-III Synchrotron using the linearly *s* polarized light of *hv* = 60 eV. Temperature was set at $T = 6$ K-230 K and clean sample surfaces were obtained for the ARPES measurements by cleaving single crystals *in-situ* in an ultrahigh vacuum better than 1×10^{-8} Pa.

Figures 1(a) and 1(b) show the second-derivative ARPES intensity plots along the Z-X and Z-Y directions, respectively, corresponding to the Z points. In Figs. 1(a) and 1(b), the direction of the uniaxial pressure is parallel or perpendicular to the *s* polarization vector, respectively [4], and both band dispersions are considered to be the electronic structure from the strain free single domain. Here, we confirmed that the electronic structure for both directions (Z-X and Z-Y) was the same at 230 K. In future work, we focus on the d_{yz} and d_{xz} orbitals as shown in Figs. 1(a) and 1(b) and will analyze the temperature dependent ARPES spectra. In the electronic structure of the Z-X and Z-Y directions, we expect that the occupation of the d_{yz} and d_{xz} orbitals might be the same due to the reentrant C_4-magnetic phase.

In summary, we have performed an ARPES study of detwinned K-Ba122 ($x \sim 0.25$) and measured the electronic structure in the Z-X and Z-Y directions. We found that the electronic structure in both Z-X and Z-Y directions shows different band dispersions, reflecting the electronic structure from the single domain due to the uniaxial pressure. We will analyze the detailed temperature dependence of the ARPES spectrum of d_{yz} and d_{xz} in future work.

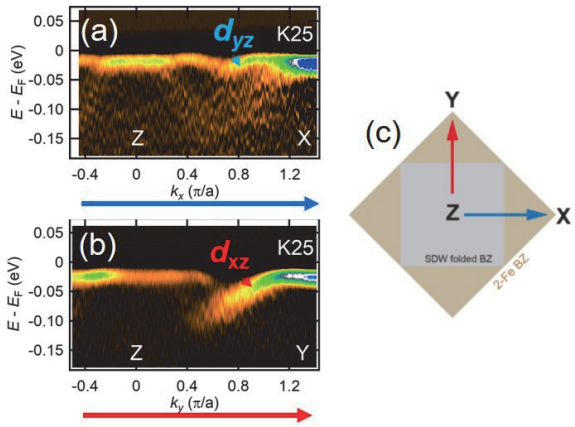

Fig. 1. (a), (b) Second-derivative ARPES intensity plots of detwinned $Ba_{0.75}K_{0.25}Fe_2As_2$ taken at $hv = 60$ eV ($T = 6$ K), corresponding to the Z point. The d_{yz} and d_{xz} bands are clearly observed differently. (c) Schematic Brillouin Zone. Blue and red arrows indicate the direction of the momentum cut of panels (a) and (b).

[1] R. M. Fernandes *et al.*, Nat. Phys. **10** (2014) 97.
[2] R. M. Fernandes *et al.*, Phys. Rev. Lett. **111** (2013) 127001.
[3] T. Shimojima *et al.*, Phys. Rev. B **90** (2014) 12111 (R).
[4] Y. Ming et al., PNAS **108** (2011) 6878.
[5] L. Wang *et al.*, Phys. Rev. B **93** (2016) 014514.
[6] A. E. Böhmer *et al.*, Nat. Commun. **6** (2015) 7911.
[7] D. D. Khalyavin *et al.*, Phys. Rev. B **90** (2014) 174511.

BL5U

Observation of Dirac Cone in Layered $NiTe_2$ by Angle Resolved Photoelectron Spectroscopy

M. Nishino[1], S. Miyasaka[1], Z. H. Tin[1], T. Adachi[1], S. Tajima[1], S. Ideta[2, 3] and K. Tanaka[2, 3]

[1]*Department of Physics, Graduate School of Science, Osaka University, Toyonaka 560-0043, Japan*

[2]*UVSOR Synchrotron Facility, Institute for Molecular Science, Okazaki 444-8585, Japan*

[3]*School of Physical Sciences, The Graduate University for Advanced Studies (SOKENDAI), Okazaki 444-8585, Japan*

Transition metal dichalcogenides MX_2 (M=transition metal elements, X=S, Se and Te) has a layered structure. These systems show various physical phenomena such as charge density wave (CDW), superconductivity and so on. MX_2 has been attracted significant attention because of their interesting properties.

Recently $PdTe_2$ and PtX_2(X=Se,Te) revisited from a viewpoint of Dirac fermion [1, 2]. Several experimental and theoretical studies has confirmed the existence of type-II Dirac cone with Dirac point at (0,0,k_z) between Γ-A points. We have investigated the angle resolved photoemission spectroscopy (ARPES) of the related system $NiTe_2$ to confirm the existence of the type-II Dirac cone and to clarify its different features between $NiTe_2$ and other systems.

The single crystals of $NiTe_2$ were synthesized by a flux method in an evacuated silica tube [3]. The results of the energy dispersive X-ray spectroscopy (EDX) indicated that the actual Ni/Te ratio is 1.17:2. The ARPES spectra were measured at BL5U of UVSOR Synchrotron Facility in Institute for Molecular Science using incident photons with $h\nu$=60-80 eV. All the measurements were carried out at 20 K.

Figure 1 shows the APRES intensity plot along k_y at various k_z (=0, 0.25 and 0.38c*). At k_z =0, there is a hole band near Fermi level around the zone center (k_y=0, Γ point), indicated by red break lines in Fig. 1(a). As shown in Figs. 1(a)-(c), this hole band systematically sinks down with increasing k_z. Around k_z =0.38c*, the top of this band is located very near Fermi level, and the band show the linear dispersion along k_y.

We also measured the band dispersion along k_z (Γ-A direction), and found the band crossing point near Fermi level around k_z =0.38c*. The present result of ARPES indicates that the Dirac point is located around (0,0,0.38c*) near Fermi level in this compound. In addition, the Dirac cone is tilted along k_z, i.e., $NiTe_2$ is a type-II Dirac fermion system.

The band calculation in consideration of the spin-orbit interaction suggests the existence of type-II Dirac cone with Dirac point around (0,0,0.36c*), which is consistent with the present ARPES results [4]. On the other hand, the energy level of the calculated Dirac point is +0.1 eV above Fermi level, and slightly different from the present experimental result. In the present work, we used the single crystals of $Ni_{1.17}Te_2$, which includes excess Ni. This excess Ni introduces the electrons into this material. As a result, the electron doping shifts up to the Fermi level and the energy level of Dirac point is located very near Fermi level in the present compound.

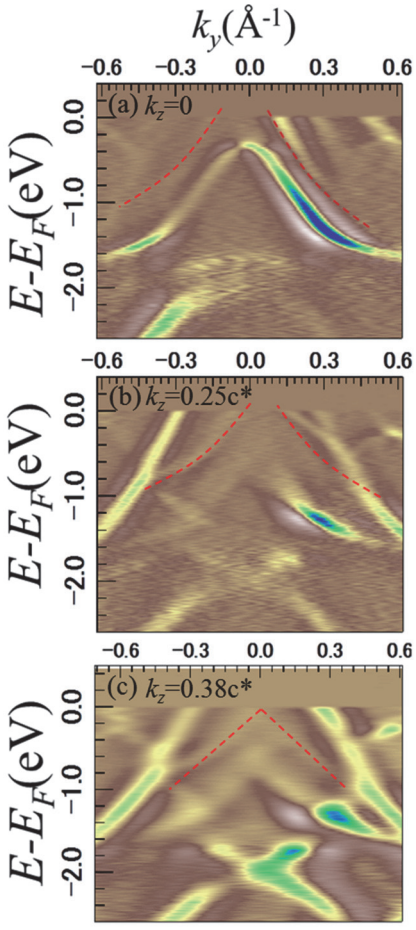

Fig. 1. ARPES intensity mapping along k_y direction at different k_z (=0, 0.25c*, and 0. 38c*) in $Ni_{1.17}Te_2$.

[1] K. Zhang *et al.,* Phys. Rev. B **96** (2017) 125102.
[2] H. -J. Noh *et al.,* Phys. Rev. Lett. **119** (2017) 016401.
[3] J. A. Wilson and A. D. Yoffe, Adv. Phys. **18** (1969) 193.
[4] H. Usui and K. Kuroki, private communication.

BL5U

Polarization-dependent Angle-resolved Photoemission Study of V_2AlC

T. Ito[1, 2], M. Ikemoto[2], D. Pinek[3], M. Nakatake[4], S. Ideta[5, 6], K. Tanaka[5, 6] and T. Ouisse[3]

[1]*Nagoya University Synchrotron radiation Research center (NUSR), Nagoya University, Nagoya 464-8603, Japan*

[2]*Graduate School of Engineering, Nagoya University, Nagoya 464-8603, Japan*

[3]*Univ. Grenoble Alpes, CNRS, Grenoble INP, LMGP, F-38000 Grenoble, France*

[4]*Aichi Synchrotron Research Center, Seto, 489-0965, Japan*

[5]*UVSOR Synchrotron Facility, Institute for Molecular Science, Okazaki 444-8585, Japan*

[6]*The Graduate University for Advanced Studies, Okazaki 444-8585, Japan*

MAX phase compounds, i.e., $M_{n+1}AX_n$ where M is a transition metal, A belongs to groups 13-16 and X is the C or N element, have recently been attracted much attention due to their possible application for new class of two-dimensional systems called MXenes by removing A atoms [1]. On the other hand, the bulk electronic structure of MAX phase has been studied mostly by calculations, mainly because of lack of well-established single crystalline samples. In this study, we have performed angle-resolved photoemission spectroscopy (ARPES) on MAX phase compound V_2AlC [2] to directly investigate the electronic structure of this system.

ARPES measurements were performed at the UVSOR-III BL5U. Data were acquired at T = 30 K with hν = 70 eV which enables us to trace around the ΓKM plane with inner potential of V_0=22.5 eV estimated from the photon energy dependent measurement (not shown). With using horizontally (P) and vertically (S) polarized photons, we have obtained the orbital dependent ARPES image. It should be noted that all ARPES images were obtained at the normal emission geometry without changing the photon incident angle relative to the sample surface by utilizing 2D mapping lens mode of MBS A-1 analyzer.

Figures 1(a) and (b) show the polarization dependent band structure along the ΓM line obtained by P- and S-polarized photons, respectively. We found that the highly dispersive electron band (e) around the Γ point dominates in Fig. 1(b). On the other hand, the spectral weight of electron band seems to be suppressed around 300 meV in Fig.1(a) where hole-like dispersive feature (h) appears below the Fermi level (E_F). From the comparison with the band calculation (Fig. 1(c)), the observed electron and hole band are correspond to larger electron and a hole pocket, respectively. To investigate the band structure near E_F in detail, we have shown the comparison of polarization-dependent EDC and MDC spectra in Figs.1(e) and (f), respectively. Here the measured momentum point of each EDC spectrum is indicated at the top of Fig.1(f). It has clearly been observed on the S-polarized spectra that the band e shows continuous dispersive feature similarly to the calculation. On the other hand, the band e on the P-polarized ones appears as intense narrow peak just below E_F together with a sudden decrease of spectral weight as approaching to the h band. As a result, the dispersive feature on the P-polarized seems to form the narrow band with its bottom locates around 200meV (h'). Though the observed narrow dispersive feature on the P-polarized electronic structure is not reproduced by the band calculation, it suggests that a orbital-dependent electron correlation effect plays a role for the mass enhancement on V_2AlC [1].

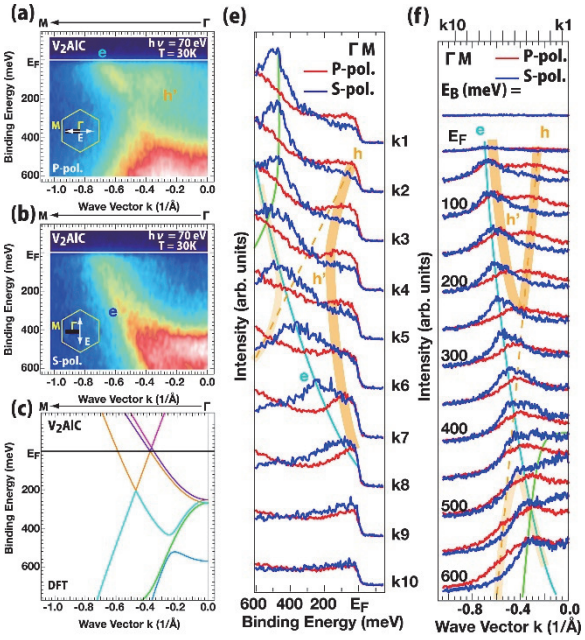

Fig. 1 Band structure along the ΓM line of V_2AlC obtained by P-(a) and S- (b) polarized photons. (c) Band calculation of V_2AlC. EDC (e) and MDC (f) spectra of V_2AlC obtained by P- (red) and S- (blue) polarized photons. In (e) and (f), solid and dashed lines are guide for eyes.

[1] M. Barsoum, *MAX phases* (Wiley, Weinheim, 2013).

[2] T. Ouisse *et al.*, J. Cryst. Growth **384** (2013) 88.

BL6B

Large Size Crystal Growth of p-terphenyl Crystal

A. Yamaji[1], S. Yamato[1], S. Kurosawa[2, 3], T. Horiai[1], S. Kodama[1], Y. Ohashi[2], Y. Yokota[2], K. Kamada[2] and A. Yoshikawa[1, 2]

[1]*Institute for Materials Research, Tohoku University, Sendai 980-8577, Japan*
[2]*New Industry Creation Hatchery Center, Tohoku University, Sendai 980-0845, Japan*
[3]*Faculty of Science, Yamagata University, Yamagata 990-8560, Japan*

Novel neutron imaging methods using a pulsed neutron source and neutron-resonance-absorption spectroscopy technique have been developed. These methods require position sensitive detectors for neutron with the Time-of-Flight (TOF), and one of the issues is development of fast response scintillator. Although some halide scintillators show high light yield and fast decay time, most halide materials have hygroscopic nature. Then, we focused on the organic scintillator crystals, which have fast decay time in the nanosecond range and no hygroscopic nature.

The organic scintillators include hydrogen with high reaction cross-section for thermal and fast neutron. However, conventional organic scintillator has low melting temperatures, and scintillation properties would degrade with overheating. Therefore, we have developed organic crystals for neutron scintillators with high melting temperatures and fast decay times.

As a first step, we grew p-terphenyl crystals by the self-seeding vertical Bridgeman technique (SSVBT) [1]. In this report, we tried to grow large size p-terphenyl crystals for the neutron detector.

Growth of p-terphenyl crystals was performed in the double-wall quartz ampoule by using the SSVBT, as shown in Fig. 1. Raw material of p-terphenyl powders (98%up purity, Tokyo Chemical Industry) was loaded into both the inner and outer ampules. The ampoule was set in a closed chamber, and was heated by using a resistive heater under nitrogen atmosphere. Due to the low purity of raw material, the ampoule was move up and down several times like zone melting for purification, and pulling rate was 0.7 mm/h.

We succeeded in growing the p-terphenyl crystal with a diameter of 22 mm as shown in Fig. 2. This crystal had some pores, and the tail portion was not flat. The surface of the tail portion (Fig. 2(a)) and the first position at the bottom of the outer ampoule (Fig. 2(c)) looked brownish and black, respectively.

Since different phases can be generated, the phases of these portions and the inner of the grown crystal (Fig. 2(b)) were measured by using transmission Fourier Transform infrared spectroscopy (FT-IR). The FT-IR transmittance spectra as shown in Fig. 3 show that only p-terphenyl phase, and no impurity phase peaks were observed, and these brownish and black parts can be some impurities such as carbon.

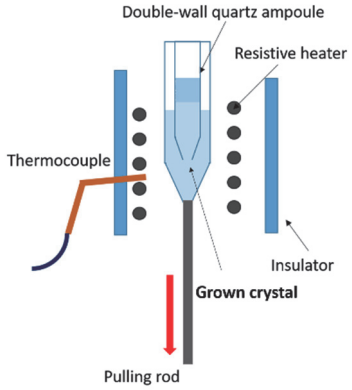

Fig. 1. Schematic of crystal growth setup by using SSVBT.

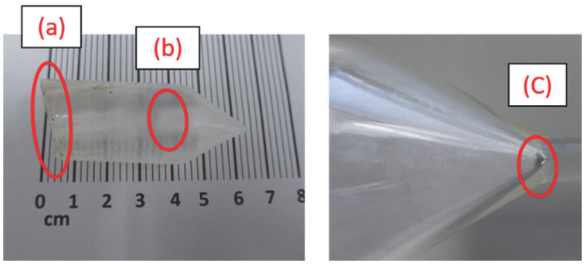

Fig. 2. Photographs of the grown crystal (left) and the bottom of the outer ampoule (right).

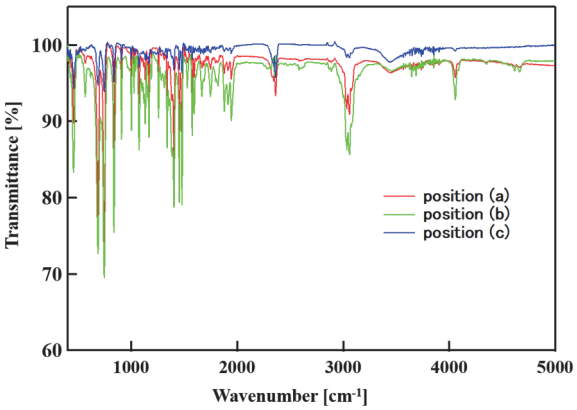

Fig. 3. FT-IR transmittance spectra of the grown p-terphenyl crystal.

[1] A. Arulchackkar avarthi *et al.,* J. Cryst. Growth **234** (2002) 159.

BL6B

Upper Ground State of Ultrashallow Thermal Donors in Silicon

A. Hara and T. Awano
Faculity of Engineering, Tohoku Gakuin University, Tagajo 985-8537, Japan

We have found ultrashallow thermal donors (USTDs) in carbon-doped and hydrogen-doped Czochralski silicon (CZ Si) crystals.[1, 2] To the best of our knowledge, these are the shallowest energy levels among those of currently reported donors in Si crystals. In addition, the ground state (1S state) of the USTDs was found to be split into at least two states.[3] This is direct evidence that the ground state of the USTDs is composed of a linear combination of the wave functions of the conduction band minimum. To evaluate the upper ground states, we measured the transmittances of various samples with different USTD concentrations between 8 and 60 K.

Carbon-doped CZ Si samples were doped with hydrogen by annealing in wet oxygen at 1300°C for 60 min. The samples were then cooled to room temperature by rapid exposure to air. For carbon doping, the Si melt used to prepare the ingot was doped with carbon powder during CZ Si crystal growth. Transmittance spectra were obtained with a far-IR spectrometer at the BL6B using a flowing cryostat.

Figure 1 shows the transmittance spectra of two samples, where sample A shows features related to USTD-1, but sample B shows weak USTD-1 features. Both samples show spectral features of USTD-3. Figure 2 shows Trans. (40 K)/Trans. (8 K), where Trans. (T K) represents the transmittance at T K. According to our previous research, the two broad dips observed at approximately 100 and 150 cm^{-1} at 40 K originate in the transition from the upper ground state to the $2P_0$ and $2P_{+-}$ states. The upper ground states are occupied by thermal excitation of electrons from the ground state. After comparing these data, we conclude the following. Features c and c* are correlated with USTD-3, but not USTD-1. Thus, feature c (c*) corresponds to the transition from the upper ground state of USTD-3 to the $2P_{+-}$ ($2P_0$) state. Namely, the energy levels of the upper ground state are inverted compared to those of the ground state. The electronic transitions are summarized in Fig. 3.

In summary, the ground-state splitting of USTDs was evaluated. The energy levels of the upper ground state are inverted compared to those of the ground state.

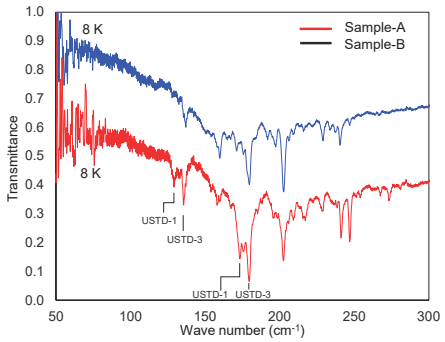

Fig. 1. Transmittance of USTDs observed in two different samples at 8 K.

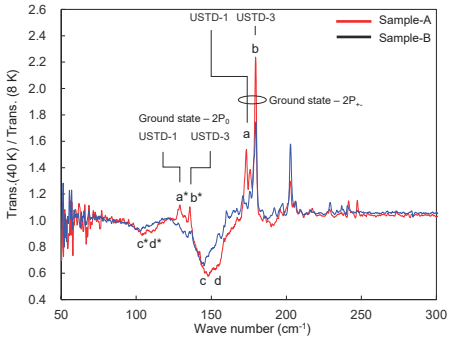

Fig. 2. Trans. (40 K)/Trans. (8 K) for two different samples in Fig. 1.

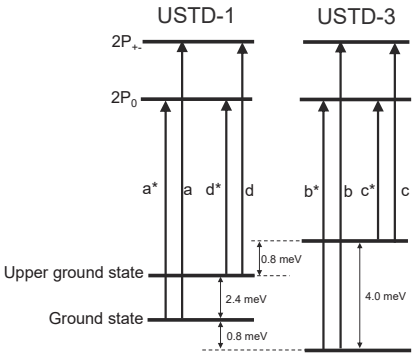

Fig. 3. The energy levels of upper ground state are inverted against those of ground state.

[1] A. Hara, T. Awano, Y. Ohno and I. Yonenaga, Jpn. J. Appl. Phys. **49** (2010) 050203.
[2] A. Hara and T. Awano, Jpn. J. Appl. Phys. **54** (2015) 101302.
[3] A. Hara and T. Awano, Jpn. J. Appl. Phys. **56** (2017) 068001.

BL6B

UV-induced Infrared Absorption Band in Ce:$Lu_{3-x}Gd_xAl_2Ga_3O_{12}$ Crystals

T. Yagihashi[1], M. Kitaura[1], K. Kamada[2], S. Kurosawa[1, 2],
S. Watanabe[3], A. Ohnishi[1] and K. Hara[4]

[1]*Faculty of Science, Yamagata University, Yamagata 990-8560, Japan*
[2]*New Industry Creation Hatchery Center, Tohoku University, Sendai 990-8560, Japan*
[3]*Graduate School of Engineering, Nagoya University, Nagoya 464-8603, Japan*
[4]*Reseach Institute of Electronics, Shizuoka University, Hamamatsu 432-8011, Japan*

We have investigated shallow electron traps in Ce:$Gd_3Al_2Ga_3O_{12}$ (Ce:GAGG) crystals, which have been known as a scintillator with high-light out. From infrared absorption spectroscopy under irradiation with ultraviolet (UV) light, it was found that a broad band appears at around 12000 cm^{-1} [1]. This band quenched at 60 K, the depth was estimated 80 meV. These facts indicate that the infrared absorption band originates in shallow electron traps. It was also clarified that the infrared absorption band is enhanced by high-temperature annealing in a reduced atmosphere. At first glance, it seems likely that shallow electron traps in Ce:GAGG crystals are associated with oxygen vacancies. However, since absorption bands due to such oxygen vacancies appear in UV region, the origin of the infrared band is different from simple oxygen vacancies. The origin of shallow electron traps in Ce:GAGG crystals still remain unclear, and is an open subject to be solved for better understanding of the development of optical materials such as scintillators and long-persistent phosphorescent phosphors [2, 3].

The purpose of the present study is to clarify whether shallow electron trap centers are formed by constituents. To do so, we have chased the change of the UV-induced infrared absorption band at cm-1 for Ce:$Lu_{3-x}Gd_xAl_2Ga_3O_{12}$ mixed crystals. The crystals were grown by the micro pulling down method. The concertation of cerium ions was set 0.5 mol% in all of crystals. Experiment was performed at the BL6B of UVSOR synchrotron facility in the Institute for Molecular Science.

Figure 1 shows UV-induced absorption spectra of Ce:$Lu_{3-x}Gd_xAl_2Ga_3O_{12}$ mixed crystals at 12 K. The data were obtained by subtracting UV-unirradiated spectra from UV-irradiated spectra. As Gd^{3+} ions are replaced by Lu^{3+} ions, the infrared absorption band at 12000 cm^{-1} is gradually weakened. It disappears completely for x=0 (Ce:$Lu_3Al_2Ga_3O_{12}$). From the creation spectra for photostimulated luminescence, it was confirmed that the bottom of the conduction band is almost unchanged for $Lu_{3-x}Gd_xAl_2Ga_3O_{12}$ mixed crystals. It is thus apparent that the low-energy shift of the conduction band is not responsible for the disappearance of the UV-induced absorption band.

The present result demonstrates that Gd^{3+} ions participate in the formation of shallow electron traps centers in Ce:GAGG crystals. It is, therefore, most likely that excited electrons are shallowly trapped by Gd^{3+} ions adjacent to oxygen vacancies. The Gd^{3+} ions may locate at the octahedral cation sites (B site). This type of the cation is named as antisite defect [4], because Gd^{3+} ions normally occupy the dodecahedral sites (A site). The theoretical calculation for the formation energy of such antisite defects revealed that they are more stable at the octahedral site rather than the tetrahedral site (C site) [5]. On this basis, Gd^{2+} ions at B sites adjacent to oxygen vacancies are most plausible candidate for the origin of shallow electron traps in Ce:GAGG crystals.

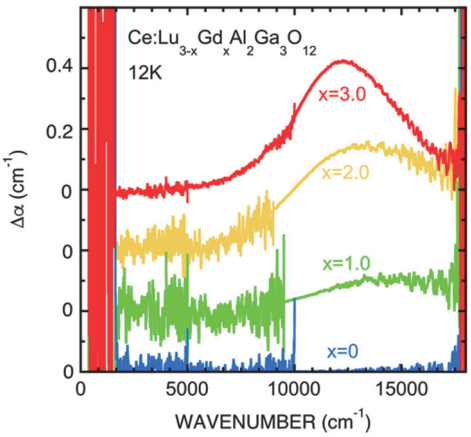

Fig. 1. UV-induced absorption spectra for Ce:$Lu_{3-x}Gd_xAl_2Ga_3O_{12}$ mixed crystals at 12 K. The data were obtained by subtracting UV-unirradiated spectra from UV-irradiated spectra.

[1] M. Kitaura *et al*., APEX **9** (2016) 072602.
[2] K. Kamada *et al*., J. Cryst. Growth **352** (2012) 88.
[3] K. Asami *et al*., Opt. Mater. **62** (2016) 171.
[4] M. Nikl *et al*., Appl. Phys. Lett. **88** (2006) 141916.

BL6B

Far-Infrared Reflective Spectrum of Lattice Vibration Modes in Lead-Free Alkali Niobate Piezoelectric Materials

H. Nishiyama, D. Ando, D. Xie, R. Hasegawa, S. Maeda, T. Fuchigami and K. Kakimoto
Graduate School of Engineering, Nagoya Institute of Technology, Nagoya 466-8555, Japan

Piezoelectric materials are widely used in the industry to convert electrical energy to mechanical energy. The piezoelectric property deteriorates by applying repeated electric field. This phenomenon is called as fatigue and serious problem for long use. Elucidation of the fatigue phenomenon is necessary to produce piezoelectric materials with high fatigue resistance. There are two origins of piezoelectric effect: lattice expansion and domain structure change. Some researchers attributed the fatigue phenomenon to pinning of the domain structure, however, there have been no investigation about the change of intrinsic effect. In previous reports, we have tried to investigate domain structure from the permittivity change in the line mapping measurement and a vibration mode of Nb - O oxygen octahedra for (Na, K)NbO_3 piezoceramics before and after fatigue processing using far-infrared (FIR) reflective analysis [1, 2]. However, we had not reached identification of the vibration mode in detail because ceramics have a lot of grains and randomly-oriented polarization structure. Therefore, vibration modes of $KNbO_3$ single crystal which has crystal system same as (Na, K)NbO_3 piezoceramics were investigated by FIR reflective analysis to clarify intrinsic effect in ceramics.

$KNbO_3$ single crystal was prepared by self flux method. It was confirmed that stripe domain structure appeared on the mirror polished surface. FIR measurement was conducted by a FT-IR spectrometer in BL6B from 100 to 660 cm^{-1}. BL1B was also used to obtain an information of optic mode TO1 at low wave number area, 15 – 110 cm^{-1}. Synchrotron light was used for polarized FIR light source in both BL1B and BL6B. The spectrum was fitted to obtain complex permittivity according to Drude-Lorentz equation and Fresnel equation. Fitting details are shown in the previous report [2].

Figure 1 shows angle of polarized light dependence of FIR reflectivity for $KNbO_3$ crystal. Reflectivity spectra changed every 15° periodically. This result showed the $KNbO_3$ crystal had a periodical structure on the surface. Figure 2 (a) shows FIR reflectivity for $KNbO_3$ crystal. Large FIR attenuations were appeared at 22.1, 190.0, 427.9 cm^{-1}. Figure 2 (b) shows imaginary part of permittivity ε'' calculated from the fitting spectrum shown in Fig.2 (a). Three transverse optic modes, TO1, TO2 and TO3, were appeared corresponding to the FIR attenuations. These results indicated that it is possible to investigate vibration modes of piezoelectric materials by combining of FIR reflectivity measurements of BL1B and BL6B. Vibration mode of ceramics should be clarified by referring to the TO modes detected in crystal.

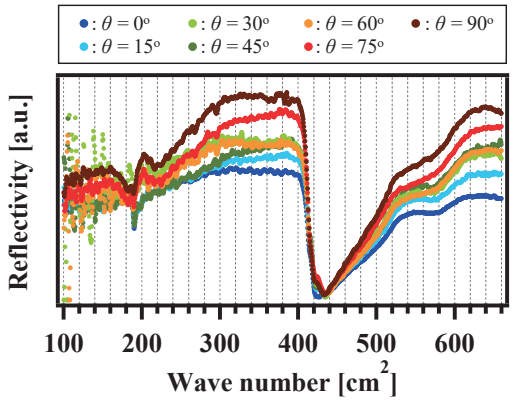

Fig. 1. Angle of polarized light dependence of FIR reflectivity for $KNbO_3$ crystal. θ = 0° means polarized light of incident FIR is parallel to the stripe domain structure.

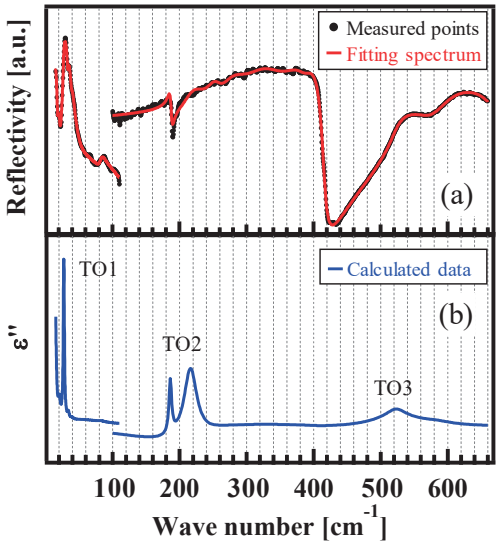

Fig. 2. FIR reflective analysis for KNbO3 crystal in a wide range of wave number from 15 to 660 cm^{-1}. Angle of polarized light θ was zero in this measurement. (a) Measurement points of FIR reflectivity and fitting spectrum (b) Imaginary part of permittivity ε'' calculated from the fitting spectrum.

[1]J. Hlinka *et al.*, Phys. Rev. Lett. **101** (2008) 167402.
[2] H. Nishiyama, N. Matsubara, K. Yoshida, D. Ando, T. Fuchigami and K. Kakimoto, UVSOR Activity Report 2016 **44** (2017) 84.

BL6B, BL7B

Anisotropic Metal-to-Insulator Transition of RuAs Probed by Polarized Infrared Micro-Spectroscopy

Y. Nakajima[1], Z. Mita[2], J. Hibi[2], S. Kamei[2], H. Watanabe[2, 1], H. Kotegawa[3], H. Sugawara[3], H. Tou[3], T. Ito[4] and S. Kimura[2, 1]

[1]*Department of Physics, Osaka University, Toyonaka 560-0043, Japan*
[2]*Graduate School of Frontier Biosciences, Osaka University, Suita 565-0871, Japan*
[3]*Department of Physics, Kobe University, Kobe 657-8501, Japan*
[4]*Synchrotron Radiation Research Center, Nagoya University, Nagoya 464-8603, Japan*

Ruthenium mono-pnictides, Ru*X* (*X* = P, As, Sb), with orthorhombic crystal structure (space group *Pnma*) attract attention because of the relationship to iron-arsenide (Fe-As) superconductors. These materials also have various physical properties such as metal-to-insulator transition (MIT) in RuAs [1], charge density wave in RuP [2] and superconducting transition in Rh-doped RuP, RuAs, and non-doped RuSb [1]. These properties are believed to be related to the superconducting property of Fe-As's, but the origin has not been clarified yet.

Recently, thanks to the successful synthesis of single-crystalline RuAs, its physical properties have now been investigated [3]. There are two structural transition at T_{MI1} = 255 K and T_{MI2} = 195 K, which are second-order and first-order transitions, respectively. The electrical resistivity slightly (rapidly) increases below T_{MI1} (T_{MI2}) suggesting that a partial (full) energy gap opens. However, there is no information of the gap opening T_{MI1} and T_{MI2} because of the limited sample size of 0.8×0.3 mm^2 at most.

To investigate the origin of MIT and the anisotropic energy gap of RuAs, we performed a polarized optical reflection spectroscopy on single-crystalline RuAs along *b* and *c* axes using IR and THz microscopes in the photon energy ranges of 0.05 – 1 eV and 20 – 60 meV, respectively, at BL6B combined with VUV reflectivity spectra at BL7B. To obtain more information, we have also performed an angle-integrated photoelectron spectroscopy (PES) at Aichi-SR.

Figure 1 shows temperature-dependent PES spectra of RuAs along the *c* axis. The spectrum does not change so much with changing temperature. This suggests that the overall electronic structure does not change by MIT. The PES spectra are consistent with the calculated density of states without any electron correlations [3]. It suggests that the intensity of the electron correlation in RuAs is weak.

Figure 2 shows polarized optical conductivity [$\sigma(\omega)$] spectra of RuAs in the IR region along two independent axes derived from the Kramers-Kronig analysis of the polarized reflectivity spectra. The strong temperature dependence is visible below the photon energy of 0.5 eV in *E* // *c* and 0.4 eV in *E* // *b*, but weak temperature dependence appears above these photon energies. The result is consistent with the PES result shown in Fig. 1, where the overall spectrum has almost no temperature dependence. Along the *c* axis (*E* // *c*), the $\sigma(\omega)$ intensity below 0.5 eV gradually decreases below the temperature of 230 K (< T_{MI1}) and suddenly drops below 190 K (~ T_{MI2}). This spectral change seems to be consistent with the structural transition. In contrast, along the *b* axis, the $\sigma(\omega)$ intensity below 0.4 eV gradually decreases with decreasing temperature.

The different behavior along the different axes is considered to be important for the origin of MIT of RuAs.

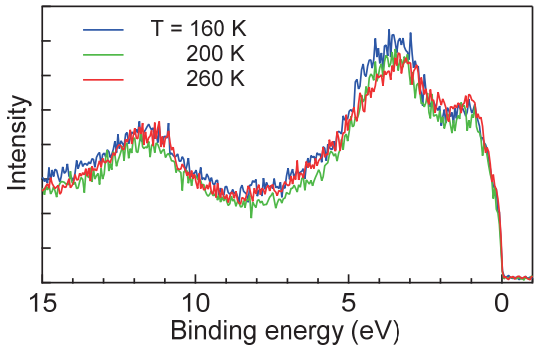

Fig. 1. Temperature-dependent angle-integrated photoelectron spectra of RuAs along the *c* axis.

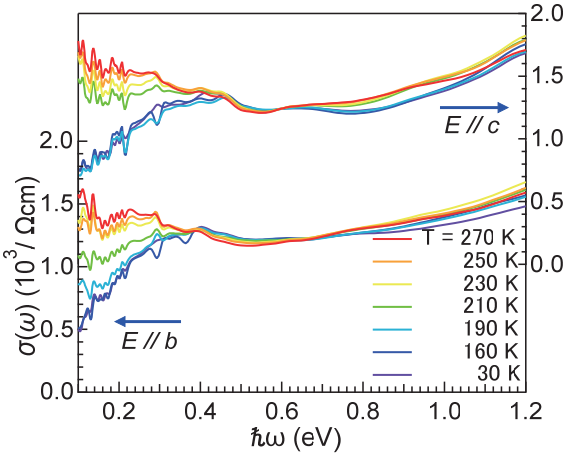

Fig. 2. Temperature-dependent optical conductivity [$\sigma(\omega)$] spectra of RuAs along the *b* and *c* axes.

[1] D. Hirai *et al.*, Phys. Rev. B **85** (2012) 140509(R).
[2] R. Y. Chen *et al.*, Phys. Rev. B **91** (2015) 125101.
[3] H. Kotegawa *et al.*, submitted.

BL6B

Infrared Microspectroscopy Using UVSOR BL6B

A. Irizawa[1], S. Suga[1], T. Nagashima[2], A. Higashiya[2], M. Hashida[3] and S. Sakabe[3]

[1]*The Institute for Scientific and Industrial Research, Osaka University, Ibaraki 567-0047, Japan*

[2]*Faculty of Science and Engineering, Setsunan University, Neyagawa 572-8508, Japan*

[3]*Advanced Research Center for Beam Science, Institute for Chemical Research, Kyoto University, Uji 611-0011, Japan*

Optical study is one of the most powerful techniques for investigating electronic states of solids. Great deal of information about electronic state, band structure, crystal structure, and dielectric response can be obtained by using spectroscopic techniques. From its handling for experiments, the optical study is extremely compatible with microscopy and under multiple conditions such as low temperature, high magnetic field, and high pressure. In the case of solids, it is well known that the temperature is one of the decisive factors for the electronic states. In case of strongly correlated systems, the considerable types of phase transition are induced by the change of the temperature. Particularly, the multiferroic compounds can be controlled of its physical properties mutually by the external fields such as magnetic, electronic, and elastic ones. The other particular condition, the pressure will directly affect the electron-electron interactions through the change of lattice constants. There we need microscopic technique for probing the small space in DAC. IN other cases, 2D scanning microspectroscopy ca detects the change of electronic and/or chemical states in particular regions such as changed and damaged by beam irradiations. The BL6B in UVSOR is adjusted for the investigations at low temperature and microscopy in the low-energy infrared region. There equips two type interferometers of both Michelson and Martin-Puplett types for FIR region and microscopy for MIR region.

In this report, we have performed the optical transmittance measurements in MIR region for several compounds having damages by THz-FEL irradiation. THz-FEL at The Institute of Science and Industrial Research (ISIR) in Osaka University is a FEL light source in the terahertz band or the far-infrared region (frequency: 2.5 - 7.5 THz, wavelength: 40 - 120 μm, wavenumber: 83 - 250 cm^{-1}) which is the boundary region of electromagnetic wave between radio waves and lights. The electric field of this intense monochromatic laser reaches several MV/cm which is enough to make ablations and/or discharge phenomena for materials. Recently, our group can be found a strange mark constructed on a surface of semiconductors, Si [1]. This stripe mark has been known as LIPSS (laser induced periodic surface structure) for the damage by NIR fs-laser irradiation, but in THz-FIR region, this is the first observation in quite different wavelength. LIPSS has been known for its fine structures having smaller period compared for the wavelength. In case of THz-FIR LIPSS, the period is about 10 times smaller than that of NIR fs-laser LIPSS. Therefore, the models of LIPSS formation considered for NIR laser can not be explicable for THz LIPSS.

Experiments are performed by using MIR microscope installed in BL6B. 2D mapping was performed for THz-FEL irradiated sample of Si. The size of aperture is 100*100 μm and 10*10 areas are measured. Both thermal light source and SR light source were used for the measurement. The spectra of irradiated and non-irradiated areas are compared right now. We will discuss the difference of spectra and the effects of THz-FEL irradiation constructing LIPSS on Si in the article under construction.

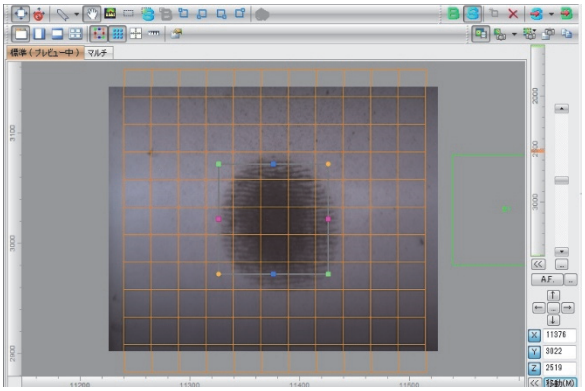

Fig. 1. MIR spectroscopic 2D mapping of THz-FEL irradiated Si.

[1] A. Irizawa, S. Suga, T. Nagashima, A. Higashiya, M. Hashida and S. Sakabe, Appl. Phys. Lett. **111** (2017) 251602.

BL7U

ARPES Study of Van Der Waals Ferromagnet $Cr_2Ge_2Te_6$

M. Suzuki[1], B. Gao[2], A. Solomon[2], K. Koshiishi[1], S. Nakata[1], K. Hagiwara[1], C. Lin[1], S. Ideta[3], K. Tanaka[3], M. Kobayashi[4], S-W. Cheong[2] and A. Fujimori[1]

[1]*Department of Physics, The University of Tokyo, Tokyo 113-0033, Japan*
[2]*Rutgers Center for Emergent Materials, Rutgers University, Piscataway, New Jersey 08854, USA*
[3]*Editorial Board, UVSOR Facility, Institute for Molecular Science, Okazaki 444-8585, Japan*
[4]*Center for Spintronics Research Network, The University of Tokyo, Tokyo 113-0033, Japan*

In recent years, van der Waals (vdW) ferromagnets, which have attractive physical properties, have been intensively studied in order to investigate the origin of their ferromagnetism with 2D crystalline [1]. A representative vdW ferromagnetic insulator $Cr_2Ge_2Te_6$ (CGT) exhibits ferromagnetism below ~ 61 K [2]. It has also been reported that the magnetic behavior of CGT atomic layer is well described as ideal 2D Heisenberg model [3].

We have conducted angle-resolved photoemission spectroscopy (ARPES) measurement of CGT with using two linearly polarization in order to clarify its electronic states directly. As shown in Fig. 1, hole-like band along the Γ point below Fermi level was observed, confirming its insulating property. We have also performed DFT calculations. The spectra nearby Fermi level obtained by the experiments and calculated partial density of states (PDOS) of Cr 3*d* electrons are shown in Fig. 2. We found that the spectrum for p-polarization has a large peak around binding energy of 2eV different from the case of s-polarization showing a peak at lower binding energy. Comparison between the experiments and the calculations suggests that the peak for p-polarization comes mainly from Cr $3d_{x^2-y^2}$ and $3d_{xy}$ orbitals, and the spectrum for s-polarization reflects Cr $3d_{z^2}$ PDOS.

For the future prospect, we would like to perform ARPES measurements for other vdW compounds such as $Cr_2Si_2Te_6$ in order to investigate the effect by the difference in composition.

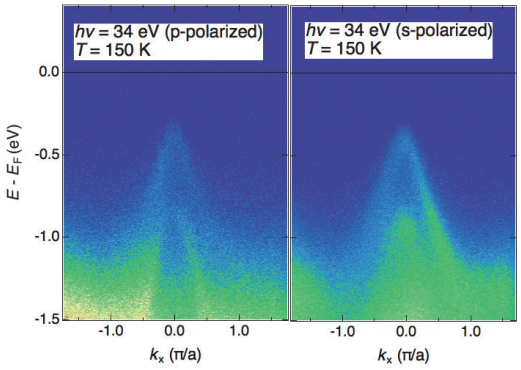

Fig. 1 ARPES spectra for different polarization.

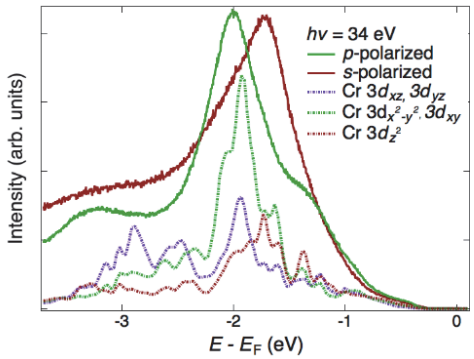

Fig. 2 The exprimental spectra near E_F for different polarization and Cr 3*d* PDOS by DFT calculation.

[1] N. Smith, Nature **546** (2017) 216.
[2] X. Zhang *et al.*, Jpn. J. Appl. Phys. **55** (2016) 033001.
[3] C. Gong *et al.*, Nature **546** (2017) 265.

BL7U

ARPES Study of Topological Line-Node Semimetal CaAgAs

D. Takane[1], K. Nakayama[1], S. Souma[2, 3], T. Wada[4], Y. Okamoto[4, 5], K. Takenaka[4], Y. Yamakawa[5, 6], A. Yamakage[5, 6], T. Takahashi[1, 2, 3] and T. Sato[1, 2]

[1]*Department of Physics, Tohoku University, Sendai 980-8578, Japan*
[2]*WPI Research Center, Advanced Institute for Materials Research, Tohoku University, Sendai 980-8577, Japan*
[3]*Center for Spintronics Research Network, Tohoku University, Sendai 980-8577, Japan*
[4]*Department of Applied Physics, Nagoya University, Nagoya 464-8603, Japan*
[5]*Institute for Advanced Research, Nagoya University, Nagoya 464-8601, Japan*
[6]*Department of Physics, Nagoya University, Nagoya 464-8602, Japan*

Topological semimetals are recently attracting a considerable attention. In contrast to conventional semimetals with a finite band overlap between valence band (VB) and conduction band (CB), topological semimetals show the touching of the VB and CB at the discrete points (called Dirac/Weyl semimetals) or along a one-dimensional curve (line-node semimetals; LNSMs) in the bulk Brillouin zone. Such Dirac/Weyl-cone states are known to provide a platform to realize exotic physical properties. The existence of three-dimensional Dirac semimetals was first confirmed in Cd_3As_2 and Na_3Bi, where the VB and CB touch with each other at the point (Dirac point) protected by rotational symmetry of the crystal. Recent studies on noncentrosymmetric transition-metal monopnictides (TaAs family) have clarified pairs of bulk Weyl-cone bands and Fermi-arc surface states, supporting their Weyl-semimetallic nature. While Dirac/Weyl semimetals with point nodes have been intensively studied experimentally, the experimental studies of LNSMs with line nodes are relatively scarce despite many theoretical predictions.

Recently, it was theoretically proposed that noncentrosymmetric ternary pnictides CaAgX [X = P, As] are the candidate of LNSM and topological insulator [1]. These materials crystallize in the ZrNiAs-type structure [see Figs. 1(a) and 1(b)]. First-principles band-structure calculations have shown that, under negligible spin-orbit coupling, CaAgX displays a fairly simple band structure near the Fermi level (E_F) with a ring-like line node (nodal ring) surrounding the Γ point of bulk hexagonal Brillouin zone (BZ). In this study, we performed an angle-resolved photoemission spectroscopy (ARPES) study on CaAgAs. By utilizing low-energy bulk sensitive ARPES at BL-7U, we determined the VB structure near E_F and revealed the LNSM nature of CaAgAs [2].

Samples were cleaved in situ along the $(11\bar{2}0)$ crystal plane. This indicates that the cleaved plane is the k_y-k_z plane in the hexagonal bulk BZ. Figures 1(c) and 1(d) show the momentum distribution curves at various binding energies (E_B's) and the corresponding second-derivative intensity plot, respectively, measured at $T = 40$ K along a cut crossing the Γ point. One can recognize linearly-dispersive hole-like bands approaching E_F [see orange dashed lines in Fig. 1(d)]. The observed band dispersions are well reproduced by the band calculations and assigned as the lower branch of the Dirac-like energy bands. Through the detailed band mapping over three-dimensional BZ, we observed ring-shaped Fermi surface on the (0001) mirror plane. These observations strongly suggest that CaAgAs is characterized by the bulk Dirac-like band and ring-torus Fermi surface associated with the line node on the mirror plane, in line with the band calculations.

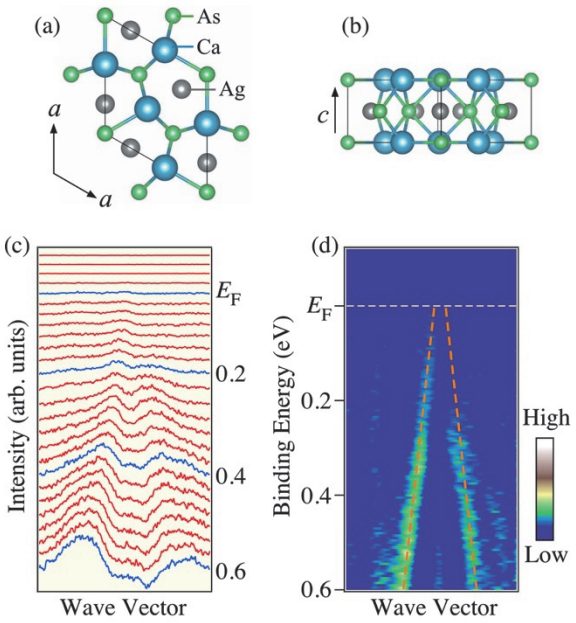

Fig. 1. (a) and (b) Two different views of crystal structure of CaAgAs. (c) Momentum distribution curves at various E_B's measured along a cut near the Γ point at $T = 40$ K with linearly-polarized 16 eV photons. (d) Second-derivative intensity of (c) plotted as a function of E_B and wave vector. Orange dashed lines are a guide for the eyes to trace the linear band dispersions.

[1] A. Yamakage *et al.*, J. Phys. Soc. Jpn. **85** (2016) 013708.
[2] D. Takane *et al.*, npj Quantum Materials **3** (2017) 1.

BL7U

Mott Insulating State in $Eu_2Ir_2O_7$ Revealed by ARPES

M. Nakayama[1], T. Kondo[1], Z. Tian[1], J. J. Ishikawa[1], M. Halim[1], C. Bareille[1], K. Kuroda[1], T. Tomita[1], S. Ideta[2], K. Tanaka[2], M. Matsunami[3], S. Kimura[4], L. Balents[5], S. Nakatsuji[1] and S. Shin[1]

[1]*ISSP, University of Tokyo, Kashiwa, Chiba 277-8581, Japan*
[2]*UVSOR Synchrotron Facility, Institute for Molecular Science, Okazaki 444-8585, Japan*
[3]*Toyota Technological Institute, Nagoya 468-8511, Japan*
[4]*Graduate School of Frontier Biosciences, Osaka University, Suita, Osaka 565-0871, Japan*
[5]*Kavli Institute for Theoretical Physics, Santa Barbara, California 93106, USA*

The 5*d* iridium oxides (iridates), having comparable scales for their kinetic energy, Coulomb interaction, and spin-orbit coupling, provide an excellent platform for studying new types of strongly correlated phenomena. Amongst them, the pyrochlore iridates ($Ln_2Ir_2O_7$, where *Ln* is a lanthanide), endowed with frustrated geometry and cubic symmetry, have a particularly fascinating phase diagram. $Pr_2Ir_2O_7$, with the largest *Ln* ion, is a metallic spin liquid and exhibits an anomalous Hall effect. For *Ln* ions with a smaller ionic radius, an antiferromagnetically ordered insulating phase appears at low temperature.

Theoretically, topological band structures have been ascribed to the $Ln_2Ir_2O_7$ series. The metallic phase is predicted to exhibit quadratically, dispersing conduction and valence bands touching at the Γ point close to the Fermi level (E_F). We have indeed identified this structure by angle-resolved photoemission spectroscopy (ARPES) in $Pr_2Ir_2O_7$ [1]. Theory predicts that such a quadratic Fermi node state may be converted into various topological states such as a topological insulator or a Weyl semimetal by appropriate symmetry breaking.

Antiferromagnetism in these materials is of the Ising type, consisting of an "all-in–all-out" (AIAO) configuration of Ir moments on alternating tetrahedra. This can be considered an "octupolar" spin order which breaks time-reversal but preserves cubic symmetry, and does not enlarge the unit cell. Early density functional studies predicted the magnetic state to be a Weyl semimetal, and general arguments imply that, if a quasiparticle picture applies at low energy in the antiferromagnetic phase, and the magnetic ordering is weak, it must exhibit Weyl points and cannot have a true gap. Nevertheless, optical and transport measurements indicate a gapped insulating ground state for $Nd_2Ir_2O_7$, despite its low antiferromagnetic–metal-insulator (MI) transition temperature $T_{MI} \approx 30$ K and proximity to metallic $Pr_2Ir_2O_7$. We have investigated the evolution of the electronic structure through the MI transition in $Nd_2Ir_2O_7$ by ARPES, and found a dramatic Slater to Mott crossover with reducing temperature [2].

We further investigated the electronic properties of $Eu_2Ir_2O_7$, an insulator with all-in all-out antiferromagnetic ordering. While the band dispersion deep below the Fermi level (~-1eV) is similar to that of the metallic $Pr_2Ir_2O_7$, the spectral weight at the Fermi level is completely diminished in $Eu_2Ir_2O_7$ (Fig.1). The gapped state lacking long-lived quasiparticles indicate that this material is a Mott insulator. We find a significant reduction of Mott gap with a little amount of carrier doping due to off-stoichiometry, and an anomalous filling of spectral weight at E_F across Neel temperature in the doped samples. These features imply that $Eu_2Ir_2O_7$ is situated near the border between the Mott- and Slater-insulating phases, suggesting a tunability by carrier doping to realize correlated topological states theoretically predicted.

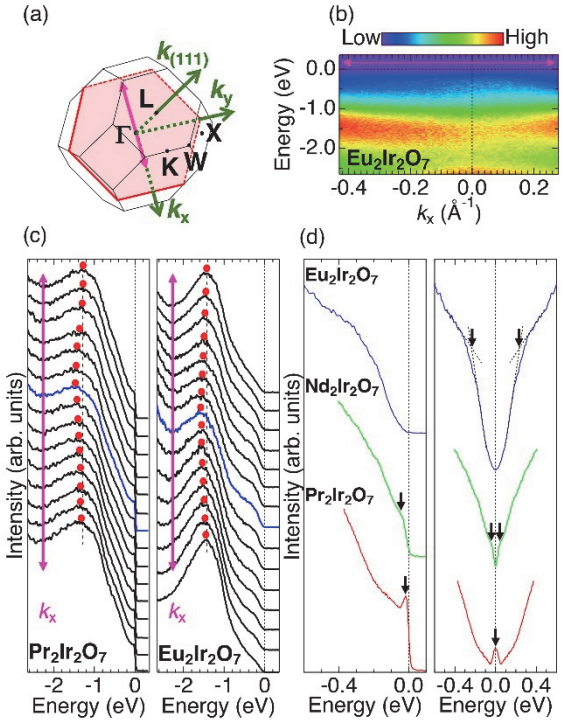

Fig. 1. (a) The Brillouin zone of $Eu_2Ir_2O_7$. (b) The ARPES dispersion map, measured along k_x crossing Γ. (c) EDCs of (b). The red points indicate peak positions. (d) Comparison of EDCs at the Γ point for three compounds.

[1] T. Kondo *et al.*, Nature communications **6** (2015) 10042.
[2] M. Nakayama *et al.*, Phys. Rev. Lett. **117** (2016) 056403.

BL7U

Superconducting Gap and Pseudogap in the Surface States of $PrFeAsO_{1-y}$ Observed by Angle-resolved Photoemission Spectroscopy

K. Hagiwara[1], M. Horio[1], K. Koshiishi[1], S. Nakata[1], C. Lin[1], M. Suzuki[1], M. Ishikado[2, 3, 4], S. Ishida[3], H. Eisaki[3], S. Shamoto[4], S. Ideta[5], K. Tanaka[5], T. Yoshida[6] and A. Fujimori[1]

[1]*Department of Physics, The University of Tokyo, Tokyo 113-0033, Japan*
[2]*Comprehensive Research Organization for Science and Society, Tokai 319-1106, Japan*
[3]*National Institute of Advanced Industrial Science and Technology, Tsukuba 305-8568, Japan*
[4]*Japan Atomic Energy Agency, Tokai, 319-1184, Japan*
[5]*UVSOR Synchrotron Facility, Institute for Molecular Science, Okazaki 444-8585, Japan*
[6]*Graduate School of Human and Environmental Studies, Kyoto University, Kyoto 606-8501, Japan*

In the 1111-type iron pnictides, superconductivity is realized by electron doping through substituting F for O or Co for Fe, or introducing oxygen deficiencies [1]. According to previous angle- resolved photoemission spectroscopy (ARPES) studies [2, 3], however, the 1111 compounds exhibit heavily hole-doped electronic structures for cleaved surfaces, which has been attributed to charge transfer due to the polar surfaces. In some ARPES studies, it has been reported that the heavily hole-doped surfaces are superconducting, but the nature of the superconductivity nor relationship between the surface electronic structure and the superconductivity has not been known yet. Therefore, more detailed knowledge about the superconducting gap at the surface is required.

In this work, we have performed ARPES studies on the 1111 compounds and have measured the temperature dependence of the energy gap in the surface states in order to study possible superconductivity at the surface of the 1111 system.

High-quality single crystals of the electron-doped superconductor $PrFeAsO_{1-y}$ (T_c = 16 K) were synthesized by the high pressure technique as described in Ref. [4]. ARPES measurements were performed at BL7U of UVSOR using linearly polarized light with the photon energy of 22.5 eV. A MBS A1 electron analyzer was used. The total energy resolution of ~ 10 meV. The crystals were cleaved *in situ* at T = 12 K. The measurements were carried out in an ultrahigh vacuum of ~ 10^{-10} Torr.

Figure 1 shows a Fermi surface (FS) mapping for the $PrFeAsO_{1-y}$ at T =12 K using s-polarization. One can clearly observe a large circular hole pocket and a small hole pocket around zone center, referred to as "Outer" and "Inner", respectively. This result is consistent with previous reports [2, 3]. Figure 2 shows the analysis of the energy gap on the "Outer" hole pocket, which originates from the surface. Panel (a) shows symmetrized energy distribution curves (EDCs) after the background subtracted at the Fermi wave vector (k_F) of the "Outer" hole pocket. The background spectra are defined by an orange line in Fig. 1. One can find an energy gap opening and a coherence peak at low temperatures. In order to quantify the energy gap, we have estimated gap size from the position where deviation from the normal-state EDCs starts indicated by triangles as shown in panel (a). We also estimated the gap area surrounded by the symmetrized EDC and the normal-state EDC. As shown in panel (c), the energy gap remains open above T_c, which may indicate a pseudogap opening. In the case of low temperature, one can observe coherence peaks, which may indicate a superconducting gap caused by proximity effect.

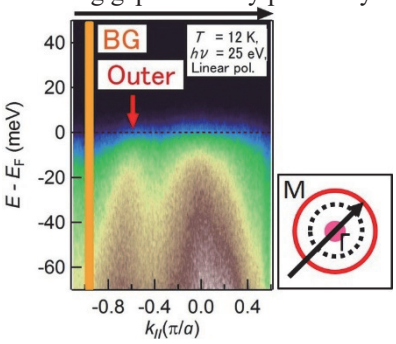

Fig. 1. *E-k* plot. Inset shows schematic FS.

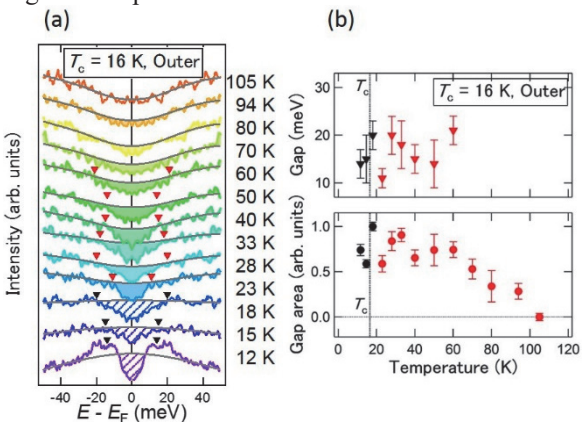

Fig. 2. Analysis of the energy gap at the "Outer" k_F. (a) Temperature dependence of the symmetrized EDCs. (b) Temperature dependence of the gap magnitude.

[1] Y. Kamihara, *et al.*, J. Am. Chem. Soc. **130** (2008) 3296.
[2] I. Nishi *et al.,* Phys. Rev. B **84** (2011) 014504.
[3] A.Charnukha *et al.,* Sci. Rep. **5** (2015) 10392.
[4] M. Ishikado *et al.,* Physica C **469** (2009) 901.

BL7U

Temperature Dependent Angle-resolved Photoemission Study of $(TMTCF)_2AsF_6$

T. Ito[1, 2], S. Ideta[3, 4], K. Tanaka[3, 4], S. Kimura[5, 6] and T. Nakamura[7]

[1]*Nagoya University Synchrotron radiation Research center (NUSR), Nagoya University, Nagoya 464-8603, Japan*

[2]*Graduate School of Engineering, Nagoya University, Nagoya 464-8603, Japan*

[3]*UVSOR Synchrotron Facility, Institute for Molecular Science, Okazaki 444-8585, Japan*

[4]*The Graduate University for Advanced Studies, Okazaki 444-8585, Japan*

[5]*Graduate School of Frontier Biosciences, Osaka University, Suita 565-0871, Japan*

[6]*Department of Physics, Osaka University, Toyonaka 560-0043, Japan*

[7]*Institute for Molecular Science, Okazaki 444-8585, Japan*

The Bechgaard salts $(TMTCF)_2X$ (C = S, Se; X = PF_6, AsF_6, etc.) belong to a family of quasi-one-dimensional (Q1D) organic conductors. These materials allow for a variety of ground states from antiferro-magnetism, a Peierl's-like spin density wave, to a superconducting state by tuning the chemical pressure with the combination of TMTSF/TMTTF and anion X [1]. Among these compounds, $(TMTTF)_2X$ system is especially important to elucidate the relation between the electronic structure and the origin of anomalous properties, because of its relatively high transition temperature from metallic to Mott localized (loc), charge ordered (CO), and antiferro-magnetic (AF) states [2]. In this study, we have performed temperature dependent angle-resolved photoemission spectroscopy (ARPES) on single-crystalline $(TMTCF)_2AsF_6$ to clarify the relation between the electric structure and the thermodynamic properties, especially the intrinsic temperature dependence originating in the phase transitions.

ARPES measurement were performed at UVSOR-III BL7U by utilizing the bulk-sensitive low photon energy (hν = 8 eV) as well as the micro focus beam (15×100 μm^2).

Figures 1 (a-d) and (e-h) show the temperature dependence of the band structure near the Fermi level (E_F) of $(TMTSF)_2AsF_6$ and $(TMTTF)_2AsF_6$, respectively. It is evident that the clear dispersive feature of TMTCF molecular orbital has been observed at T = 30 K (Figs. 1(a) and (e)) for both case. With increasing temperature, the dispersive TMTSF band on metallic $(TMTSF)_2AsF_6$ remain existing until T = 260 K (Fig. 1(d)). On the other hand, TMTTF features on $(TMTTF)_2AsF_6$ show anomalous temperature dependence. At CO state (T = 30 K), the electronic structure of $(TMTTF)_2AsF_6$ is dominated with the dispersive feature folded around k_x = 0.30 Å^{-1}. With increasing temperature at the loc. state, the top of dispersive feature gradually shifts to higher binding energy side while the spectral weight of non-dispersive broad feature around 1 - 1.5 eV increases as shown in Fig. 1 (j). Then the electronic structure at the metallic state is dominated with the localized feature on $(TMTTF)_2AsF_6$ in contrast to the dispersive feature on $(TMTSF)_2AsF_6$. We expect that the observed characteristic itinerant to localized transition of the TMTTF states play a dominant role in the CO-loc.-metal phase transition on $(TMTTF)_2AsF_6$.

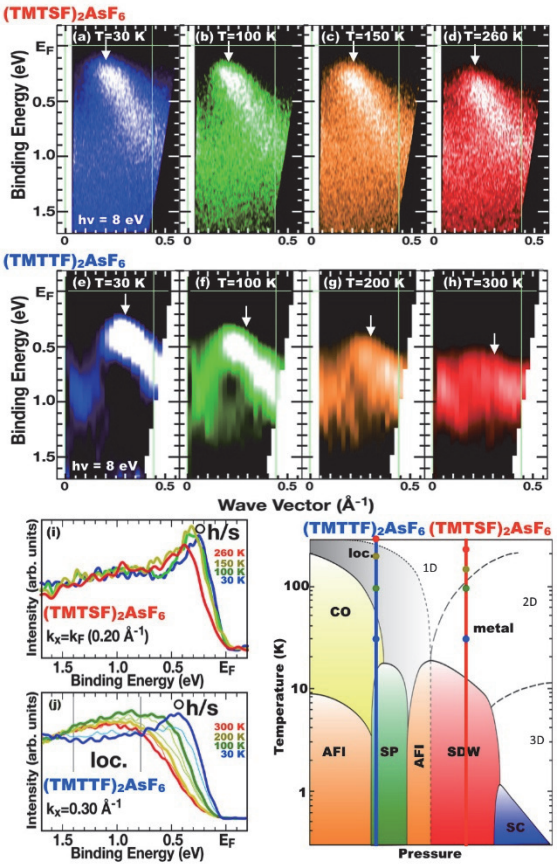

Fig. 1. Temperature dependent ARPES images and EDC spectra at k_x=0.20 Å^{-1} and 0.30 Å^{-1} of $(TMTSF)_2AsF_6$ (a-d and i) and $(TMTTF)_2AsF_6$ (e-h and j), respectively. Phase diagram of $(TMTCF)_2X$ [2] is also indicated.

[1] T. Ishiguro *et al.*, Organic Superconductors (Springer-Verlag, Berlin, 1998).

[2] E. Rose *et al.*, J. Phys.: Condens. Mat. **25** (2013) 014006.

BL7U

Low-Energy Heavy-Fermion Bands in $YbCdCu_4$ Observed by Angle-Resolved Photoemission Spectroscopy

H. Shiono[1], S. Ishihara[1], K. Mimura[1], H. Sato[2], E. F. Schwier[2], K. Shimada[2], M. Taniguchi[2], S. Ideta[3], K. Tanaka[3], T. Zhuang[4], K. T. Matsumoto[4], K. Hiraoka[4] and H. Anzai[1]

[1]*Graduate School of Engineering, Osaka Prefecture University, Sakai 599-8531, Japan*
[2]*Hiroshima Synchrotron Radiation Center, Hiroshima University, Higashi-Hiroshima 739-0046, Japan*
[3]*UVSOR Synchrotron Facility, Institute for Molecular Science, Okazaki 444-8585, Japan*
[4]*Graduate School of Science and Engineering, Ehime University, Matsuyama 790-8577, Japan*

In rare-earth compounds, the hybridization effect between conduction and localized-4*f* electrons (*c-f* hybridization) leads to the formation of heavy electrons, and it is characterized by a renormalized band structure near the Fermi level (E_F). According to the single-impurity Anderson model, the Yb^{2+} $4f_{7/2}$ peak of Yb compounds appears at the energy scales of the Kondo temperature T_K, which is a measure of the hybridization strength [1]. Hence, the electronic band structure near E_F provides important clues to heavy fermion state.

The Laves-phase structure $YbCdCu_4$ is known as a heavy fermion compound with the electronic specific heat coefficient $\gamma \sim 175$ mJ/K^{2}mol [2] and as a good reference for studies the first-order valence transition of $YbInCu_4$ [3]. To understand the heavy-fermion state in $YbCdCu_4$, it is essential to unveil the nature of the Yb 4*f* and conduction-band states.

Angle-resolved photoemission spectroscopy (ARPES) is a direct probe to measure the electronic excitation as functions of energy and momentum. Here, we report on a study of the hybridization effect in $YbCdCu_4$ based on ARPES data of the electronic band structure near E_F. The experiments were performed at BL7U of UVSOR and BL-1 of Hiroshima Synchrotron Radiation Center (HSRC).

Figure 1(a) shows ARPES spectra of $YbCdCu_4$ taken along the $\bar{\Gamma}$-$\bar{K}$ direction of the surface Brillouin zone. Two flat bands at $|\omega| \sim 0.02$ and 1.3 eV are assigned to the spin-orbit split Yb^{2+} $4f_{7/2}$ and $4f_{5/2}$ states, respectively. A dispersive band was observed over an energy range of $0.1 < |\omega| < 1.2$ eV. This conduction band intersects with the $4f_{7/2}$ state and reaches E_F, as seen from the peaks of momentum distribution curves in Fig. 1(b). Thus, Fermi surface of $YbCdCu_4$ at least consists of one hole band around the $\bar{\Gamma}$ point.

For quantification of the hybridization strength, we have measured the temperature dependence of the Yb^{2+} $4f_{7/2}$ state. A significant shift and an intensity enhancement in the $4f_{7/2}$ peak are observed, as shown by angle-integrated photoemission spectra in Fig. 1(c). We plotted the peak positions as a function of temperature in Fig. 1(d), which reveals a continuous decrease in the energy with decreasing temperature. The peak energies extrapolated to zero temperature is estimated to be ~ 26 meV and corresponds to $T_K \sim 300$ K, which is roughly consistent with T_K reported from the magnetic susceptibility measurements [2]. This consistency implies that the heavy-fermion state in $YbCdCu_4$ stems from the hybridization between the observed $4f_{7/2}$ and conduction bands. Further experiments in wide momentum ranges are needed to understand the evolutions of the heavy-fermion bands of $YbCdCu_4$.

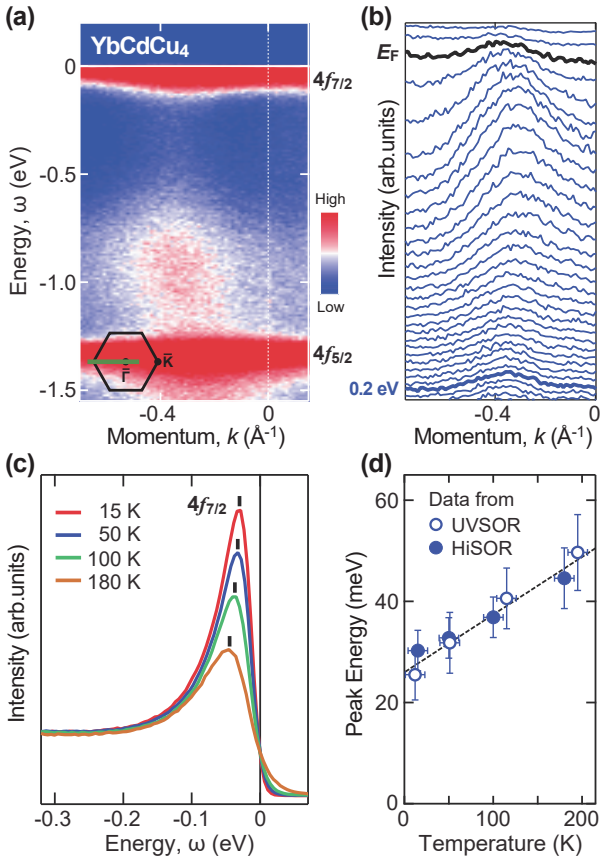

Fig. 1. (a) ARPES spectra of $YbCdCu_4$ taken along the $\bar{\Gamma}$-$\bar{K}$ direction at 15 K. The data were obtained at BL-1 of HSRC. (b) Momentum distribution curves near E_F. (c) Angle-integrated spectra at various temperatures. (d) Energy shift of the Yb^{2+} $4f_{7/2}$ peak in panel (c), together with the data from UVSOR.

[1] R. I. R. Blyth *et al.*, Phys. Rev. B **48** (1993) 9497.
[2] J. L. Sarrao *et al.*, Phys. Rev. B **59** (1999) 6857.
[3] I. Felner *et al.*, Phys. Rev. B **35** (1987) 6935.

BL7U

High-Resolution ARPES Study of FeSe Superconductor

G. Phan[1], K. Nakayama[1], H. Oinuma[1], T. Nakamura[1], D. Takane[1], Y. Nakata[1], T. Urata[2], Y. Tanabe[1], K. Tanigaki[1, 3], F. Nabeshima[4], M. Kawai[4], Y. Imai[1], A. Maeda[4], T. Takahashi[1, 3, 5] and T. Sato[1, 5]

[1]*Department of Physics, Tohoku University, Sendai 980-8578, Japan*
[2] *Department of Crystalline Material Science, Nagoya University, Nagoya 464-8603, Japan*
[3]*WPI Research Center, Advanced Institute for Materials Research, Tohoku University, Sendai 980-8577, Japan*
[4]*Deptment of Basic Science, The University of Tokyo, Tokyo 153-8902, Japan*
[5]*Center for Spintronics Research Network, Tohoku University, Sendai 980-8577, Japan*

Iron chalcogenides $FeSe_{1-x}Te_x$, the structurally simplest iron-based superconductors, are the target of intensive research because of rich physical properties such as superconductivity, antiferromagnetism, structural transition, and electronic nematicity. It was also reported that the physical properties of $FeSe_{1-x}Te_x$ show gigantic pressure effects. For instance, the superconducting transition temperature (T_c) of FeSe is dramatically enhanced from 8 K to 36 K by the application of high pressure. Elucidating the origin of such pressure effects would provide a key to understanding the mechanism of high-T_c superconductivity.

Recent advances in fabricating epitaxial thin films of $FeSe_{1-x}Te_x$ have opened a door to controlling the lattice parameters by tuning the lattice mismatch with substrate. This strain engineering has capability for manipulating various physical properties. For $FeSe_{1-x}Te_x$, compressive strain enhances the T_c up to 12 K in FeSe [1] and further to 23 K in $FeSe_{0.8}Te_{0.2}$ [2]. In addition, strain-induced drastic changes in the structural, magnetic, and nematic properties have been discovered [3]. These discoveries have provided a great opportunity for investigating the interplay between the physical properties and the lattice parameters at ambient pressure. In this study, we have performed high-resolution angle-resolved photoemission spectroscopy (ARPES) on compressive strained $FeSe_{1-x}Te_x$ thin films on CaF_2 substrate at BL-7U and compared their electronic structure with that of strain-free FeSe. We have revealed the evolution of electronic structure with epitaxial strain.

High-quality FeSe thin films were grown on CaF_2 substrate by pulsed laser deposition. The film thicknesses are approximately 300 monolayers. In Fig. 1, we show representative electronic structure measured in the normal state of bulk FeSe. One can recognize hole-like and electron-like band dispersions at the Brillouine-zone center (Γ point) and corner (M point), respectively, indicative of semimetallic nature of FeSe. When compressive strain is applied on CaF_2 substrate, hole-like and electron-like bands shift upward and downward, respectively. This observation indicates a strain-induced change in the semimetallic band overlap [4]. We have also determined the electronic structure of Te-substituted films on CaF_2 and found a marked change in the electronic structure compared with that in pristine FeSe. Our observations provide important insights into the interplay between T_c enhancement and lattice parameters.

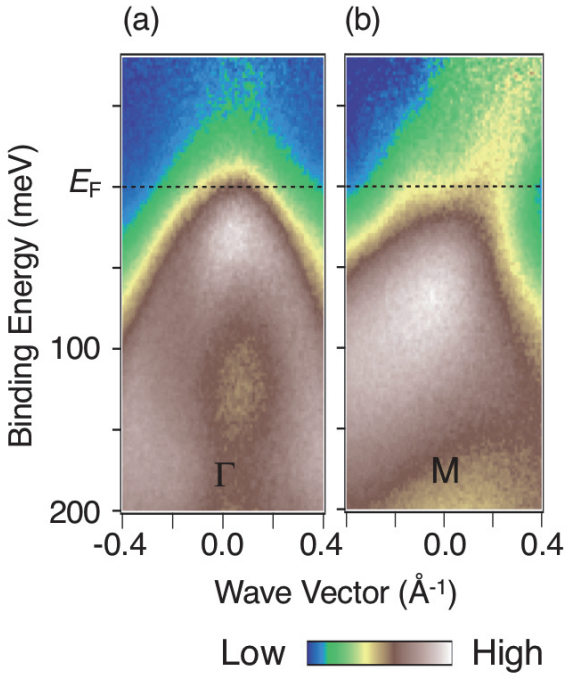

Fig. 1. (a) and (b) ARPES intensity plot around the Brillouin-zone center and corner, respectively, on FeSe at T = 280 K, obtained after dividing by the Fermi- Dirac function convoluted with the instrumental resolution. The data have been obtained with linearly- polarized 21-eV photons.

[1] F. Nabeshima *et al.*, Appl. Phys. Lett. **103** (2013) 172602.
[2] Y. Imai *et al.*, Proc. Natl. Acad. Sci. USA **112** (2015) 1937.
[3] Y. Imai *et al.*, Sci Rep. **7** (2017) 46653.
[4] G. Phan *et al.*, Phys. Rev. B **95** (2017) 224507.

BL7U

Electronic Structures of Methylanmmoniumlead Trihalides Single Crystals

S. Yamanaka[1], K. Tonami[1], S. Ideta[2], K. Tanaka[2], K. Yamada[3], H. Yoshida[4] and Y. Nakayama[1]

[1]*Department of Pure and Applied Chemistry, Tokyo University of Scienece, Noda, 278-8510, Japan*
[2]*UVSOR Synchrotron Facility, Institute for Molecular Science, Okazaki 444-8585, Japan*
[3] *College of Industrial Technology, Nihon University, Narashino 275-8575, Japan*
[4] *Graduate School of Engineering, Chiba University, Chiba 263-8522, Japan*

$CH_3NH_3PbX_3$ (X = Br, I) thin films are used as light absorption and charge separation materials of perovskite solar cells [1]. However, many structural defects (such as crystal grain boundaries) and impurities remain in polycrystalline thin films, which may cause problems in evaluating the precise electronic structure of the substances. In this study, we aimed to clarify the intrinsic electronic structures of $CH_3NH_3PbX_3$ by using single crystal samples.

$CH_3NH_3PbBr_3$ was produced from CH_3NH_3Br and $PbBr_2$ in *N, N*-dimethylformamide; $CH_3NH_3PbI_3$ was synthesized from CH_3NH_3I and PbI_2 in γ-butyrolactone. In either case, single crystal samples (typically as Figs. 1(a) and 1(b)) were prepared by inverse temperature crystallization methods [2, 3]. For the sake of obtaining the clean surface of the $CH_3NH_3PbX_3$ single crystals, cleavage of the crystal surface in vacuum was examined by breaking a ceramic post bounded on top of each sample. Ultraviolet photoelectron spectroscopy (UPS) measurements on the $CH_3NH_3PbX_3$ single crystals were conducted at BL7U of UVSOR. The excitation energy was set at 40 eV. In order to avoid charging of the sample during the measurements, the samples were irradiated with a laser beam (512 nm) at the same time.

Figure 2 (a) shows UPS spectra of a $CH_3NH_3PbBr_3$ single crystal before and after cleavage. It was confirmed that the peak intensity derived from Pb5d (binding energy (BE) around -20 eV) was enhanced and valence band structures (BE of -2 to -15 eV) were defined as a result of cleavage. This suggests that the clean surface is successfully obtained by cleavage in vacuum. Nevertheless, a new peak derived from metallic Pb (Pb^0) appeared at BE ~ -18 eV. This is plausibly due to damages in the $CH_3NH_3PbBr_3$ sample caused by irradiation with ultraviolet light during the measurements.

Figure 2 (b) shows UPS spectra of a $CH_3NH_3PbI_3$ single crystal before and after cleavage. Similarly to the $CH_3NH_3PbBr_3$ case, enhanced intensities of the Pb5d peaks suggest successful cleaning of the $CH_3NH_3PbI_3$ surface by cleavage in vacuum. Furthermore, in the case of $CH_3NH_3PbI_3$, it was confirmed that the peaks of Pb5d shifted by +0.20 eV, which suggests change in band bending. On the other hand, shift in the secondary electron cutoff measured with a separate equipment ("off-line ARPES" device) indicated that the vacuum level moves by 0.7 eV on the high energy side after cleavage in vacuum. These results suggest that impurities on $CH_3NH_3PbI_3$ single crystals induce a negative vacuum level shift of -0.5 eV and downward band bending of -0.2 eV. This implies the formation of a surface electric double layer due to the electrons being donated from the surface impurities to the $CH_3NH_3PbI_3$ side. In addition, it was revealed that the Pb^0 peak intensity was minor in comparison to the $CH_3NH_3PbBr_3$ case, suggesting that $CH_3NH_3PbI_3$ is more robust to the ultraviolet light.

This work was conducted as Joint-Studies-Programs [27-545 and 27-835] of IMS.

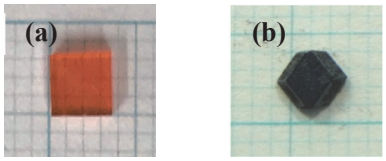

Fig. 1. Photographs of the (a) $CH_3NH_3PbBr_3$ and (b) $CH_3NH_3PbI_3$ single crystal samples.

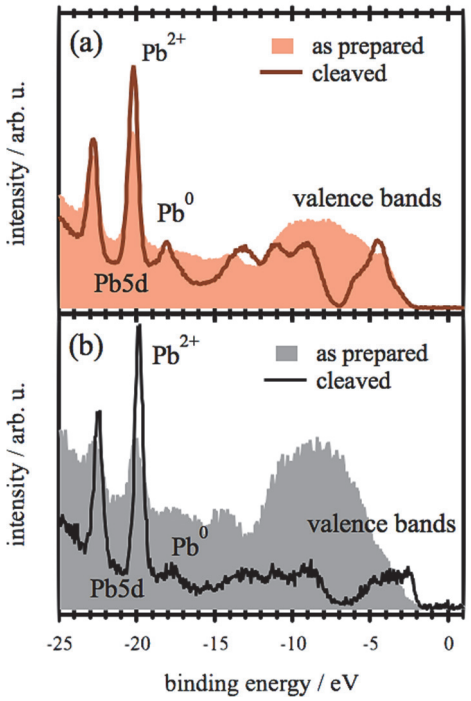

Fig. 2. UPS spectra of the (a) $CH_3NH_3PbBr_3$ and (b) $CH_3NH_3PbI_3$ single crystal samples before and after cleavage in vacuum.

[1] A. Kojima *et al.,* J. Am. Chem. Soc. **131** (2009) 6050.
[2] F. Zhang *et al.,* J. Mater. Chem. C. **5** (2017) 8431.
[3] H. Wei *et al.,* Nat. Mater. **16** (2017) 826.

BL7U

Superconducting Gap of Iron-Based Superconductor $Ba_{0.75}K_{0.25}Fe_2As_2$

S. Ideta[1, 2], M. Nakajima[3], N. Murai[4], R. Kajimoto[4] and K. Tanaka[1, 2]

[1]*UVSOR, Synchrotron Facility, Institute for Molecular Science, Okazaki, 444-8585, Japan*

[2] *The Graduate University for Advanced Studies (SOKENDAI), Okazaki, 444-8585, Japan*

[3]*Department of Physics, Graduate School of Science, Osaka University, Toyonaka, 560-0043, Japan*

[4] *Materials and Life Science Division, J-PARC Center, Japan Atomic Energy Agency, Tokai 319-1195, Japan*

Iron-based superconductors have a complex phase diagram with the antiferromagnetic (AFM) transition and the structural phase transition. Recently, nematicity, defined as broken rotational symmetry [a trigonal (C_4)-to-orthorhombic (C_2) structural transition], has shed light on the understanding of the mechanism on the iron-based superconductivity [1-4]. In hole-doped $BaFe_2As_2$ (Ba122) system, thermal expansion, specific heat, and neutron diffraction measurements of $Ba_{1-x}Na_xFe_2As_2$ and $Ba_{1-x}K_xFe_2As_2$ (K-Ba122) have shown the magnetic order without C_4 symmetry breaking [5, 6]. Besides, the superconductivity is suppressed between the superconducting (SC) and the C_4-magnetic phase. The mechanism of the suppressed superconductivity has been unclear yet, and it would give us a great interest to elucidate the hole-doped Ba122 superconductor.

Here, we have investigated the electronic structure of $Ba_{0.75}K_{0.25}Fe_2As_2$ focusing on the superconducting gaps using high energy resolution angle-resolved photoemission spectroscopy (ARPES). We found that the hole Fermi surfaces (FSs) showed the FS dependent SC gap, and the suppressed SC gap would be responsible for the low T_c in K-Ba122 with $x \sim 0.25$.

High-quality single crystals of $Ba_{0.75}K_{0.25}Fe_2As_2$ (T_c ~ 25 K) were grown by self-flux technique. ARPES experiments were carried out at BL7U of UVSOR-III Synchrotron using the linearly polarized light of hv = 18 eV-32 eV photons. Temperature was set at T = 12 K and 35 K and clean sample surfaces were obtained for the ARPES measurements by cleaving single crystals *in-situ* in an ultrahigh vacuum better than 6×10^{-9} Pa.

Figures 1(a1) and 1(a2) show the ARPES intensity plot as a function of energy and momentum taken at hv = 21 eV and 32 eV, corresponding to the Γ and Z points, respectively. We observe at least two hole bands for Γ and Z points, indicating that the degenerated inner bands (d_{yz}, d_{xz}) and outer (d_{xy}/d_z^2) bands. Taking into account the electronic structure of K-Ba122 ($x \sim 0.25$) in the k_z direction [7], we observed the SC gap at the Γ and Z points on the hole FSs. In Figs. 1(c1)-1(d2), energy distribution curve (EDC) at Fermi momentum (k_F) for inner (α) and outer (γ) hole bands are shown. EDCs are divided by the Fermi-Dirac function and the peak position corresponds to the SC gap shown by a gray circle. Here, we found that the energy gap is suppressed on the outer hole FS (γ) only for K-Ba122 ($x \sim 0.25$) compared with the nearly optimally doped K-Ba122 (x = 0.3).

The present study reveals that the SC gap on hole FSs shows finite nodeless gaps but is strongly suppressed in K-Ba122 ($x \sim 0.25$), and therefore, we propose that the suppressed outer hole FS reflects the suppressed T_c in this material.

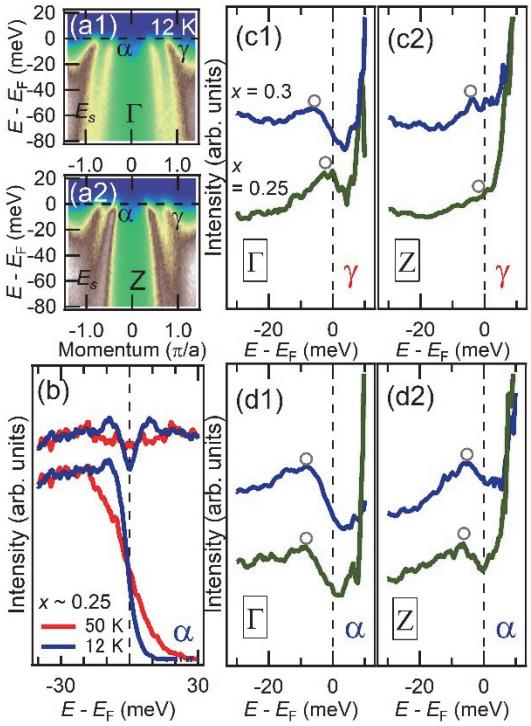

Fig. 1. (a1), (a2) Energy-momentum plots of the hole FSs at the Γ and Z points (T = 12 K) (b) Temperature dependence of ARPES spectrum. (c1)-(d2) EDCs of the α and γ bands at the k_F position divided by Fermi-Dirac (FD) distribution function for K-Ba122 ($x \sim 0.25$ and 0.3).

[1] R. M. Fernandes *et al.*, Nat. Phys. **10** (2014) 97.
[2] R. M. Fernandes *et al.*, Phys. Rev. Lett. **111** (2013) 127001.
[3] T. Shimojima *et al.*, Phys. Rev. B **90** (2014) 12111.
[4] Y. Ming *et al.*, PNAS **108** (2011) 6878-6883.
[5] L. Wang *et al.*, Phys. Rev. B **93** (2016) 014514.
[6] A. E. Böhmer *et al.*, Nat. Commun. **6** (2015) 7911.
[7] S. Ideta *et al.*, UVSOR Activity Report **44** (2016) 76.

BL7U

Temperature Dependence of Mott Gap in Ca_2RuO_4 Investigated by ARPES

D. Shibata[1], M. Kawamoto[1], K. Yamawaki[1], D. Ootsuki[1], C. Sow[2], Y. Maeno[2], F. Nakamura[3] and T. Yoshida[1]

[1]*Graduate School of Human and Environmental Studies, Kyoto University, Kyoto 606-8501, Japan*
[2]*Department of Physics, Graduate School of Science, Kyoto University, Kyoto 606-8502, Japan*
[3]*Kurume Institute of Technology, Fukuoka 830-0052, Japan*

A t_{2g}-electron system $Ca_{2-x}Sr_xRuO_4$ with a layered perovskite structure shows a rich phase diagram [1]. Sr_2RuO_4 is a leading candidate of a spin triplet superconductor. On the other hand, Ca_2RuO_4 is an antiferromagnetic insulator below T = 110 K and a paramagnetic insulator between T = 110 K and 357 K. Ca_2RuO_4 undergoes a metal to insulator (MI) transition at T_{MI} = 357 K accompanied by a fist-order structural phase transition. The RuO_4 octahedra shrink along the *c*-axis and d_{xy} orbital becomes dominant in the insulating phase [2]. The insulator to metal transition can be achieved not only by raising temperature, but also by chemical substitution, applying pressure and electric field. In this work, we studied temperature dependence of the Mott gap in Ca_2RuO_4 using angle-resolved photoemission spectroscopy (ARPES).

Figure 1 shows ARPES spectra of Ca_2RuO_4 taken with $h\nu$ = 23 eV. In order to determine the orbital character of the band structure near E_F, we measured the incident light polarization dependence of the spectra. The intensity at ~ -1.8 eV is enhanced with *p*-polarized light, indicating $d_{yz/zx}$ orbital character. On the other hand, the intensity at ~ -0.8 eV is enhanced in the *s*-polarized spectrum, indicating d_{xy} orbital character. The parabolic band structure from -0.8 eV to -2.5 eV can be assigned to d_{xy} orbital. These results are consistent with the previous ARPES study [3]. The DMFT calculation also indicates that the intensity at ~ −0.8 eV and at ~ −1.8 eV correspond to d_{xy} and $d_{yz/zx}$ orbital, respectively [3, 4].

Figure 2 (a) shows the angle-integrated photoemission spectra of Ca_2RuO_4 along Γ-S line. The gap size decreases with increasing temperature. To clarify the temperature evolution of the gap, we estimated the gap size by using linear extrapolation from the slope of spectra. The gap size is consistent with that estimated from the optical conductivity [5]. The suppression of the gap size may be caused by the elongation of *c*-axis. These results imply that the d_{xy} orbital plays a crucial role in the insulator to metal transition.

[1] S. Nakatsuji and Y. Maeno, Phys. Rev. Lett. **84** (2000) 2666.
[2] M. Braden *et al*., Phys. Rev. B **58** (1998) 847.
[3] D. Sutter *et al*., Nat. Comm. **8** (2017) 15176.
[4] G. Zhang *et al*., Phys. Rev. B **95** (2017) 075145.
[5] J. H. Jung *et al*., Phys. Rev. Lett. **91** (2003) 056403.

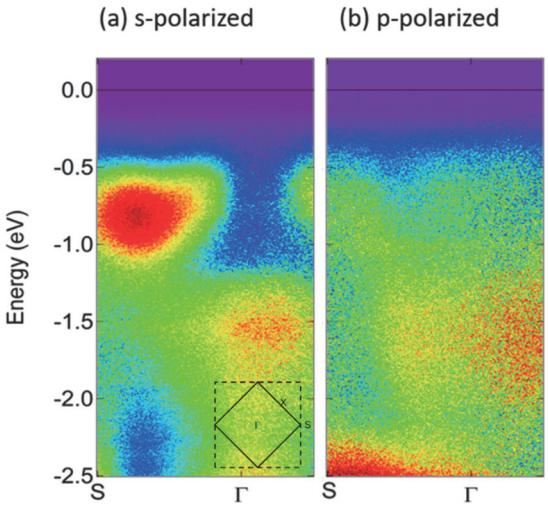

Fig. 1. ARPES spectra along Γ-S line taken at T = 170 K using (a) *s*- and (b) *p*-polarized light.

size decreases with increasing temperature.

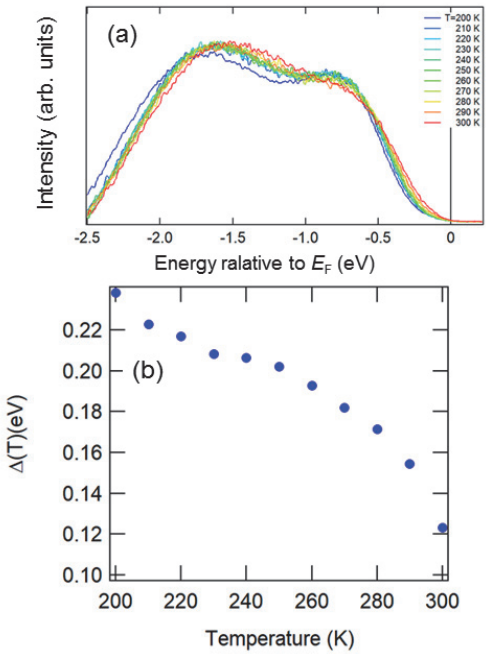

Fig. 2. Temperature dependence of gap structure. (a) Angle-integrated spectra along Γ-S line. (b) Gap size estimated from the spectra in panel (a).

BL7B

Analysis of Luminescence and Scintillation Processes of Organic–inorganic Perovskite-type Compounds Using VUV Excitation Light

N. Kawano[1], M. Koshimizu[2], G. Okada[3], Y. Fujimoto[2], N. Kawaguchi[3], T. Yanagida[3] and K. Asai[1]

[1]*Graduate School of Engineering Science, Akita University, Akita 010-8502, Japan*
[2]*Graduate School of Engineering, Tohoku University, Sendai 980-8579, Japan*
[3]*Graduate School of Materials Science, Nara Institute of Science and Technology, Ikoma 630-0192, Japan*

To develop a scintillator with excellent time resolution, we focused on the phenomena exhibited by confined excitons in nanoscale semiconductors. Among the compounds with a low-dimensional system, scintillation materials based on luminescence from organic–inorganic layered perovskite-type compounds are of particular interest. These hybrid materials have self-organized multiple quantum well structures. An inorganic quantum well exhibits luminescence of confined excitons, and its organic layer acts as a barrier of confinement structures. In the compounds, excitons confined in the inorganic layer have large binding energies and oscillator strengths due to the quantum confinement and the image charge effects.

We have demonstrated that the organic–inorganic layered perovskite-type compounds exhibit efficient scintillation due to exciton emission from the inorganic layer. Among them, $(C_6H_5C_2H_4NH_3)_2PbBr_4$ exhibits fast scintillation decay (~10 ns) and efficient luminescence that exceeds 10,000 photons per MeV under synchrotron X-ray (67.4 keV) [1, 2] and gamma-ray irradiation [3]. We reported that the excellent scintillation properties of $(C_6H_5C_2H_4NH_3)_2PbBr_4$ originate from the fast radiative rate of the excitons, which is caused by the lattice distortion in the inorganic layers verified with single- crystal structural analysis [4]. In addition to the effect on the crystal structure, the organic moieties in the organic layers would influence the scintillation properties via possible energy transfer from the organic layers to the inorganic layers. We have reported that the energy transfer slower than the time resolution of the measurement systems (100 ps) and have a negligible contribution to the scintillation properties of the compounds [5]. However, the component of energy transfer faster than the time resolution (100 ps) could have an influence on the scintillation properties of organic–inorganic layered perovskite-type compounds.

In this study, a crystal of $(C_6H_5C_2H_4NH_3)_2PbBr_4$ was fabricated by the poor-solvent diffusion method. Luminescence spectra and decay curves were measured under VUV irradiation at the UVSOR Synchrotron Facility (BL7B; Okazaki, Japan) to analyze the possible contribution of the energy transfer.

Table 1 summarizes the decay time constants and relative intensities (in parentheses) of photoluminescence decay at 410 nm with different excitation wavelengths. The rise time behavior observed in the luminescence decay curve showed no difference among the excitation wavelengths of 60–300 nm. The decay can primarily be attributed to radiative transition of the Wannier excitons in the inorganic layers. In addition, no excitation peak of benzene such as an intense peak at 180nm ($^1A_{1g}\rightarrow{}^1E_{1u}$) in the vacuum ultraviolet region was observed in the excitation spectra measured while monitoring the exciton emissions from the inorganic layer. These results indicate that the effect of energy transfer from the organic layer to the inorganic layer has negligible contribution to the luminescence properties of organic–inorganic layered perovskite-type compounds.

Table 1. Decay time constants and relative intensities (in parentheses) of photoluminescence decay at 410 nm with different excitation wavelengths.

Excitation Wavelength (nm)	First component (ns)	Second component (ns)
60	1.4 (95%)	14 (5%)
150	1.3 (94%)	21 (6%)
180	1.7 (92%)	19 (8%)
250	2.0 (91%)	15 (9%)
300	3.0 (91%)	18 (9%)

[1] S. Kishimoto, K. Shibuya, F. Nishikido, M. Koshimizu, R. Haruki and Y. Yoda, Appl. Phys. Lett., **93** (2008) 261901.
[2]N. Kawano, M. Koshimizu, A. Horiai, F. Nishikido, R. Haruki, S. Kishimoto, K. Shibuya, Y. Fujimoto, T. Yanagida and K. Asai, Jpn. J. Appl. Phys., **55** (2016) 110309.
[3]N. Kawano, M. Koshimizu, G. Okada, Y. Fujimoto, N. Kawaguchi, T. Yanagida and K. Asai, Sci. Rep. **7** (2017) 14754.
[4] N. Kawano, M. Koshimizu, Y. Sun, N. Yahaba, Y. Fujimoto, T. Yanagida and K. Asai, J. Phys. Chem. C, **118** (2014) 9101.
[5] N. Kawano, M. Koshimizu, Y. Sun, N. Yahaba, Y. Fujimoto, T. Yanagida and K. Asai, Jpn. J. Appl. Phys., **53** (2014) 02BC20.

BL7B

Anomalous Thermoelectric Response and Charge Dynamics of Pyrochlore $(Eu_{1-x}Ca_x)_2Ir_2O_7$

J. Fujioka[1, 2], R. Kaneko[1] , M. Masuko[1], K. Ueda[1] and Y. Tokura[1, 3]

[1]*Department of Applied Physics and Quantum-Phase Electronics Center (QPEC), University of Tokyo, Tokyo 113-8656, Japan*

[2]*PRESTO, Japan Science and Technology Agency, Kawaguchi 332-0012, Japan*

[3]*RIKEN Center for Emergent Matter Science (CEMS), Wako 351-0198, Japan*

The interplay between the relativistic spin-orbit interaction and electron correlation provides a fruitful field to research unconventional quantum phenomena such as the topological semimetal and Kitaev spin liquids. The pyrochlore-type iridates $R_2Ir_2O_7$ (R=rare earth elements) is one of candidate materials to study the Mott physics or magnetism of correlated Weyl electron. Wan *et al.* , proposed the possible emergence of antiferromagnetic Weyl semimetallic phase on the verge of Mott transition [1]. The giant negative magnetoresistivity and metallic edge state emerging at the antiferromagnetic domain walls of $Nd_2Ir_2O_7$ have been argued in terms of the magnetic field-induced topological transition and topological edge state of Weyl electrons [2, 3]. Moreover, even in the paramagnetic phase, possible non-Fermi liquid behavior due to the zero-gap semiconducting band or flat-band with long-lived spin moment have been proposed [4]. In this study, we have investigated the charge transport and charge dynamics of hole-doped $Eu_2Ir_2O_7$ to explore the novel non-Fermi liquid behavior.

Figure 1(a) shows the temperature dependence of resistivity for $Eu_2Ir_2O_7$ and its Ca-doped analogs $(Eu_{1-x}Ca_x)_2Ir_2O_7$. $Eu_2Ir_2O_7$ (x=0) exhibits insulating behavior below 300 K and the resistivity shows a kink upon the antiferromagnetic magnetic ordering at 123 K. In the hole doped systems, the resistivity shows a similar behavior and the kink is discernible for x=0.01, 0.02 and 0.03. On the other hand, for x=0.05 and 0.1, the kink is no longer discernible and paramagnetic metallic behavior subsists down to 2 K.

Figure 1(b) shows the Seebeck coefficient of metallic systems. With decreasing temperature, the Seebeck coefficient is enhanced and reaches 30 μV/K around 50 K for x=0.1. Similar behavior is also observed for x=0.05 and 0.2. Such a non-monotonic temperature dependence and relatively large value are not common among conventional correlated metals.

To explore the electronic structure in the paramagnetic metallic state, we show the optical conductivity spectra of $(Eu_{1-x}Ca_x)_2Ir_2O_7$ in Fig. 2. The charge gap with a magnitude of 0.1 eV is discernible for x=0. On the other hand, the gap is closed and a Drude response shows up for x=0.05 and 0.2. It should be noted that an absorption peak with narrow width is observed around 0.05 eV besides the broad continuum above 0.1 eV. Such an absorption band suggests the emergence of flat-band with enhanced density of state (DOS). Since the Seebeck coefficient is sensitive to the DOS, the appearance of flat-band with high-DOS may be related to the anomalous enhancement of Seebeck coefficient.

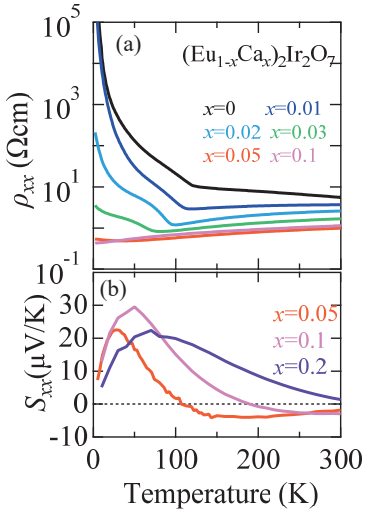

Fig. 1 Temperature dependence of (a) resistivity and (b) Seebeck coefficient.

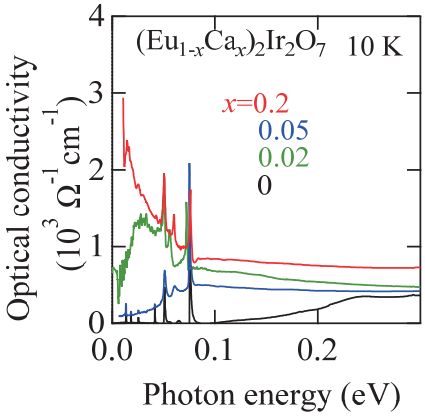

Fig. 2 Optical conductivity spectra at 10 K.

[1] X. Wan *et al.*, Phys. Rev. B **83** (2011) 205101.
[2]K. Ueda, *et al.*, Phys. Rev. Lett. **115** (2015) 056402.
[3] E. Y. Ma, *et al.*, Science **350** (2015) 538.
[4] H. Shinaoka *et al.*, Phys. Rev. Lett. **115** (2015) 156401.

BL7B

Study of Optical Absorption of Parasitic Transition Metal ions (Fe^{3+}, Cr^{3+}) at Low Temperature in Nonlinear Crystal YAl3(BO3)4 (YAB) in the 100 – 600 nm Range

E. Lafitte-Houssat[1, 2], A. Kausas[1], L. Zheng[1], H. Ishizuki[1], G. Aka[2] and T. Taira[1]
[1]*Laser Research Centre, Institute for Molecular Science, Okazaki 444-8585, Japan*
[2]*PSL Research University, Institute de Recherche de Chimie Paris IRCP, Chimie ParisTech, Paris 75005, France*

YAB crystals are very promising NLO material for UV applications, one of them being the fourth harmonic generation of Nd^{3+} based lasers at 266 nm . The UV cut-off wavelength is measured to be 170 nm , but Fe^{3+} and Cr^{3+} impurities in the crystals generally cause parasitic UV absorption. The conversion process of YAB crystals is then jeopardized in the deep UV. Low temperature transmittance spectra as function of polarization should allow us to clearly identify transition ions responsible for parasitic optical absorption in the UV range of interest. As absorption band intensities increase at low temperature, the characterization of the peaks should be eased. During our experiment at BL7B, we have studied the influence of temperature on optical transmission for YAB samples within 30 K-300 K temperature range.

Three samples were studied at 300 K to identify the transitions related to transition ions Fe^{3+} and Cr^{3+}, (Fig. 1(a)) in the range of 150 nm to 600 nm . For this scanning, YAB#1 had its Y axis perpendicular to the light polarization, while YAB#2 had its Y axis parallel to the light polarization. The axis for YAB#3 could not be determined. Two absorption bands can be identified around 240 nm and 280 nm . They may be attributed to charge transfer processes from oxygen to iron $O2p^5$-$Fe3d^6$: ($e^2t_2^4$, 240 nm) and ($e^3t_2^3$, 280 nm). For YAB#1, there is another absorption around 425 nm , that corresponds to a d-d transition of Cr^{3+} ($^4A_{2g} \rightarrow {}^4T_{2g}$), that usually occurs at 425 nm in Cr doped YAB crystals. However, the absence of that transition for the two other samples is not usual. It can be explained by different purities of the starting materials, or by the crucible used for YAB#1 crystal growth (one-month experiment). For the sample YAB#1, we can also notice that the cut-off wavelength is higher than for YAB#2 and YAB#3. This is most likely caused by the higher thickness of the sample. For the three samples, the cut-off wavelength is higher than 170 nm , which is caused by the optical absorption of the transition ions. Also, there is no absorption at 532 nm for all three samples, which confirms that YAB crystals are well suited for SHG from 532 nm to 266 nm .

At low temperature, as thermal motion is reduced, we should be able to better visualize transition ion absorptions. The results we obtained were not totally in accordance with that assumption. For all three samples, we could see that there were few overall differences when the temperature varies, even from 30 K to 300 K range.

The influence of the orientation of the crystal is much more visible and interesting. The results are shown in Fig.1(b) for the sample YAB#2, but they were the same for the other samples. For all the samples, the orientation has an effect in the range 225-350 nm . The absorption at 280 nm is weaker when the Y axis is parallel to light polarization. However, for the transition at 240 nm , it is more visible when the Y axis is parallel. As the absorption at 266 nm must be limited, the orientation of the crystal must be controlled to have the best performance in frequency conversion. For all the samples, the absorption around 266 nm is weaker when the Y axis is parallel to the polarization of the incoming light. It means that this orientation is to be preferred for FHG experiments with YAB crystals.

We have studied three YAB samples under UV polarized light and their transmission spectra. The parasitic absorption of transition ions Fe^{3+} and Cr^{3+} was confirmed. Charge transfer processes $O2p^5$-$Fe3d^6$ were identified around 240 nm and 280 nm , and d-d transitions of Cr^{3+} may be visible in one of the YAB samples. The influence of temperature and the orientation of the crystals was also investigated. The orientation of the crystals influences greatly the transmission profiles, especially for the charge transfer transitions. The scanning under low temperature did not deliver a better characterization but still confirmed the assumptions about parasitic absorptions.

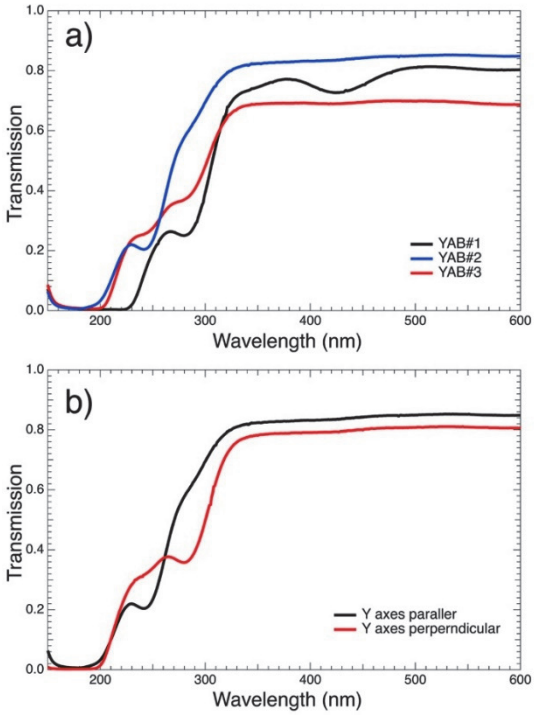

Fig. 2. Optical transmission spectra for YAB#1, YAB#2 and YAB#3 crystals (a) and comparison of crystal orientation for YAB#2 (b).

[1] Y. Wang and R.K. Li, Opt. Materials **32** (2010) 1313.

BL7B

Auger-Free Luminescence in K_2ZnCl_4 Crystals

A. Ohnishi and M. Kitaura
Faculty of Science, Yamagata University, Yamagata 990-8560, Japan

The Auger-free luminescence (AFL) is a peculiar type of intrinsic luminescence in ionic crystals in which the valence excitation through a nonradiative Auger process is forbidden. The AFL is characterized by a high quantum yield and a short lifetime of the order of ns. Therefore, it is very useful as the fast scintillator for high-energy physics, positron emission tomography and so on.

In previous works [1-4], we have studied optical properties of Cs_2ZnCl_4 and Rb_2ZnCl_4 molecular ionic crystals with the use of synchrotron radiation as a light source. We have observed AFL in these crystals. K_2ZnCl_4 is one of molecular ionic crystals and has the same crystal structure as Cs_2ZnCl_4 and Rb_2ZnCl_4 [5]. In this crystal, the outermost core level is supposed to be built up by Zn 3d states, because the K 3p state should be deeper-lying inner shells than the Zn 3d state in comparison with the binding energies of electrons between them. Therefore, it is expected that AFL due to interatomic p-d transitions between the Zn 3d outer-most core level and the Cl 3p valence band is observed in K_2ZnCl_4. In the present study, we have investigated the luminescence of K_2ZnCl_4 crystals under the outermost core excitation, in order to find the existence of AFL.

K_2ZnCl_4 crystals were prepared by evaporating a stoichiometric mixture of solutions of KCl and $ZnCl_2$. The reflection, emission and excitation spectra were measured at the BL7B of UVSOR.

As indicated by a red line in Fig. 1, sharp peaks at 7.3 and 7.9 eV were observed in the reflection spectrum measured for the cleaved surface of K_2ZnCl_4. The 7.3 and 7.9 eV peaks are assigned to the $n = 1$ and 2 exciton peaks due to the transition from the Cl 3*p* valence band to the conduction band, respectively. From the positions of the two peaks, the band gap energy (E_g) is estimated to be about 8.0 eV by assuming that the exciton energy levels are hydrogen-like.

From the result of X-ray photoelectron spectroscopy (XPS), it was clear that the outer-most core level in K_2ZnCl_4 is composed of the Zn 3d states. We estimated the energy difference (E_{VC}) between the top of the valence band and that of the outer-most core band by referring to the XPS spectrum. The value of E_{VC} was 6.5 eV. Since this value is smaller than that of E_g, the appearance of AFL due to the interatomic Cl 3p → Zn 3d transitions is expected for K_2ZnCl_4, when a core hole is created in the Zn 3d outer-most band by photo-excitation.

When K_2ZnCl_4 was excited at 10 K with 21.4 eV photons above the value of $E_g + E_{VC}$, three luminescence bands appeared at 5.9, 4.4 and 2.8 eV. The blue line in Fig. 1 shows the excitation spectrum for the 4.4 eV band. The excitation spectra for the 5.9 and 2.8 eV bands were practically the same as that for the 4.4 eV band. These bands are excited in the energy region above 14.4 eV. The photon energy of 14.4 eV is almost agreement with the energy sum of E_g and E_{VC}. Since this satisfies the condition for the occurrence of AFL, the three bands mentioned above are assigned to the AFL bands due to the radiative recombination of a valence electron and an outermost core hole.

Luminescence decay measurements were also performed using a time-correlated single-photon counting technique under the single bunch operation. It was proved that, at 10 K, the AFL bands are composed of a fast decay component with the lifetime of about 8 ns.

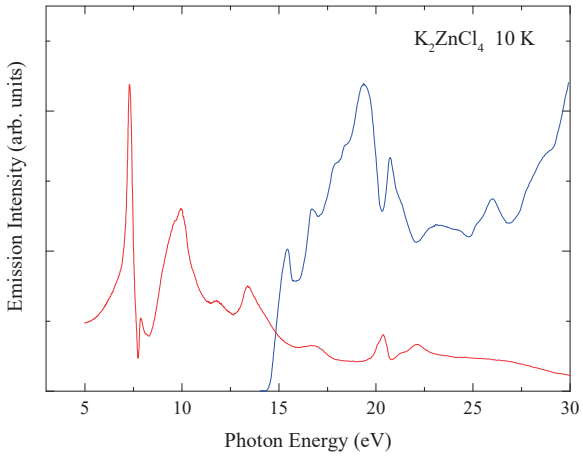

Fig. 1. Excitation spectrum (blue line) at 10 K for the 4.4 eV band in K_2ZnCl_4. For reference, reflection spectrum is also shown by a red line.

[1] A. Ohnishi, T. Otomo, M. Kitaura and M. Sasaki, J. Phys. Soc. Jpn. **72** (2003) 2400.
[2] A. Ohnishi, M. Saito, M. Kitaura, M. Itoh and M. Sasaki, J. Lumin. **132** (2012) 2639.
[3] A. Ohnishi, M. Kitaura, M. Itoh and M. Sasaki, J. Phys. Soc. Jpn. **81** (2012) 114704.
[4] M. Kitaura and A. Ohnishi, Kogaku **45** (2016) 175 (in Japanese).
[5] J. A. Mcginnery, Inorg. Chem. **13** (1974) 1057.

BL7B

Optical Property of Compound Fluoride Materials $Ca_xSr_{1-x}F_2$ at Low Temperature

K. Suzuki, R. Yamazaki, J. Otani and S. Ono
Nagoya Institute of Technology, Nagoya 466-8555, Japan

Vacuum ultraviolet (VUV) light source is used in various applications such as surface treatment, optical cleaning of semi-conductor substrates and sterilization. Accordingly, the detector for monitoring the light source is also required. Currently, many researchers developed VUV detectors based on oxide, nitride and diamond. However, the detectors require the filters for cutting off deep-UV when being used for monitoring of the light source. On the other hand, our group is proceeding to development of the VUV detectors using fluorides [1-3]. Some fluorides have extremely wider band gap than oxides and nitrides so that they transmit deep-UV region. Until now, we achieved filterless VUV detectors by applying such fluorides. And spectral response of the detectors varies according to band gap of the material. Therefore, we may realize the detectors possessing arbitrary response region by controlling band gap of the material. Here, we report on controlling band gap of compound fluoride materials $Ca_xSr_{1-x}F_2$ and the temperature dependence of the band gap of these materials.

$Ca_xSr_{1-x}F_2$ crystals were grown by Bridgman method and they were controlled composition ratio as $Ca_{0.85}Sr_{0.15}F_2$ and $Ca_{0.5}Sr_{0.5}F_2$. Absorption coefficient was calculated by measuring transmission spectrum of VUV region as shown in Fig.1. Herewith, band gaps of CaF_2, $Ca_{0.85}Sr_{0.15}F_2$, $Ca_{0.5}Sr_{0.5}F_2$ and SrF_2 were calculated as 10.24, 9.98, 9.83 and 9.73 eV at R.T., respectively. Therefore, the band gap of $Ca_xSr_{1-x}F_2$ is expanded by increasing composition ratio of CaF_2 in the crystals.

Additionally, the band gap at low temperature (50 - 300K) was obtained by cooling the samples with liquid helium. Solid lines in Fig.2 were calculated from Bose-Einstein type equation as given below

$$E(T) = E(0) - \frac{2a}{\exp\left(\frac{\Theta}{T}\right) - 1}$$

where $E(0)$ is band gap energy at 0 K, a is strength of exciton-phonon interaction, and Θ is average temperature of phonons. As a result of that, the band gaps of CaF_2, $Ca_{0.85}Sr_{0.15}F_2$, $Ca_{0.5}Sr_{0.5}F_2$ and SrF_2 at 0 K were estimated as 10.69, 10.46, 10.23 and 10.13 eV, respectively.

In summary, we found capable of controlling the band gap of $Ca_xSr_{1-x}F_2$ and evaluated the band gap of $Ca_xSr_{1-x}F_2$ at low temperature. The band gap was expanded by increasing composition ratio of CaF_2 in the crystals. Such result shows that we can control the spectral response of filterless VUV photoconductive detector using $Ca_xSr_{1-x}F_2$ crystals.

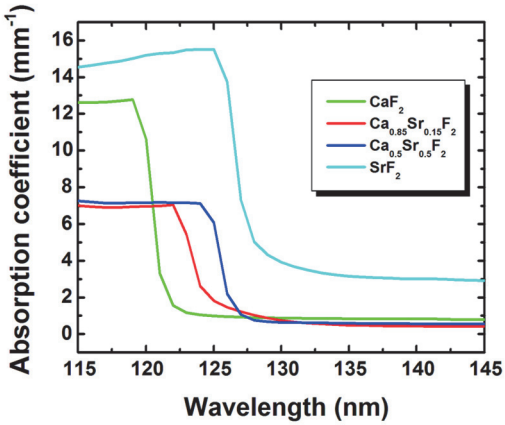

Fig. 1. Temperature characteristic of band gap.

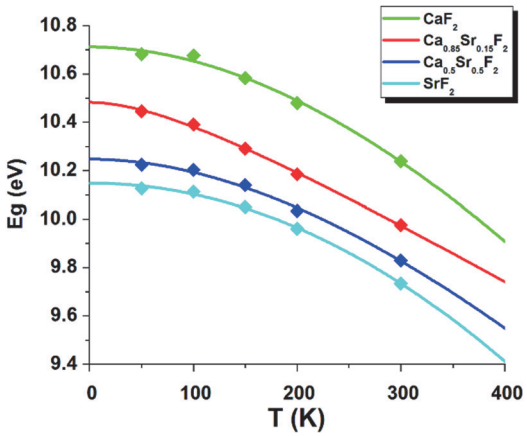

Fig. 2. Temperature characteristic of band gap.

[1] M. Ieda, T. Ishimaru, S. Ono, N. Kawaguchi, K. Fukuda, T. Suyama, Y. Yokota, T. Yanagida and A. Yoshikawa, Jpn. J. Appl. Phys. **51** (2012) 062202.
[2] T. Ishimaru, M. Ieda, S. Ono, Y. Yokota, T. Yanagida and A. Yoshikawa, Thin Solid Films **534** (2013) 12.
[3] M. Yanagihara, H. Ishikawa, S. Ono and H. Ohtake, Testing and Measurement: Techniques and Applications (2015) 151.

UVSOR User 2

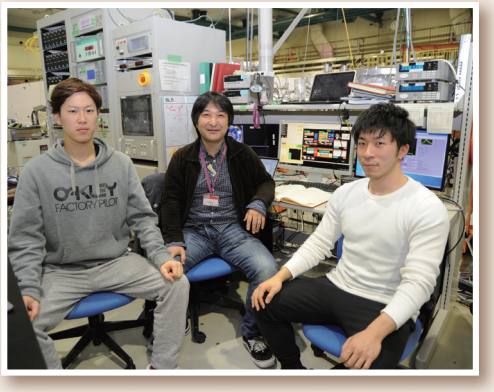

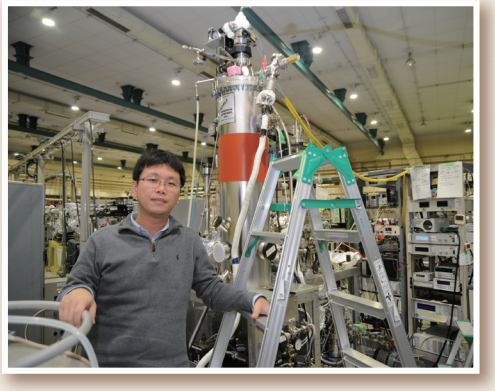

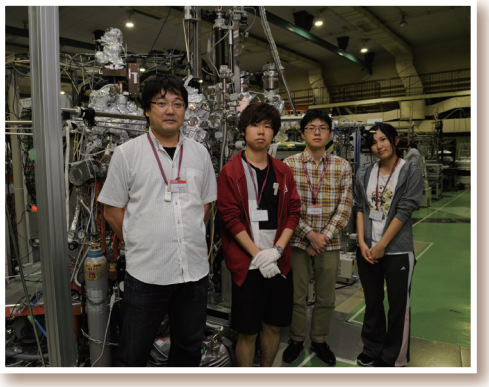

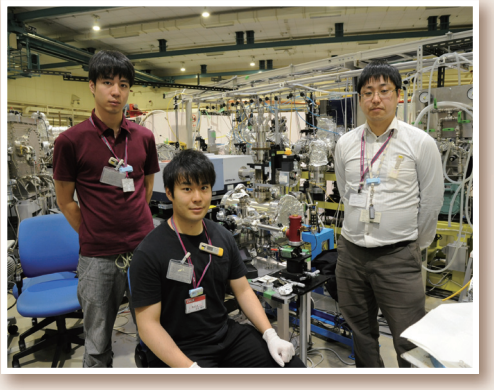

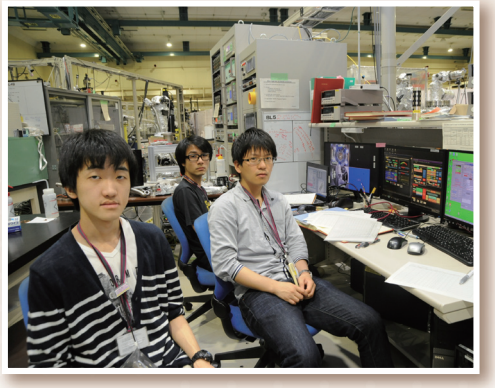

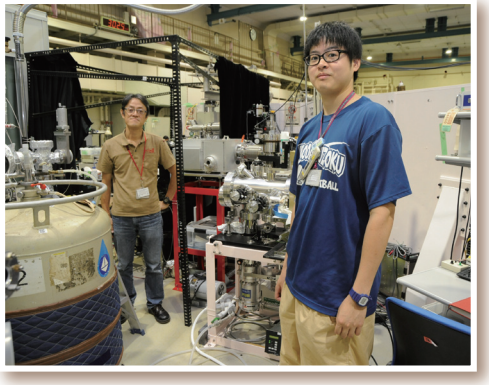

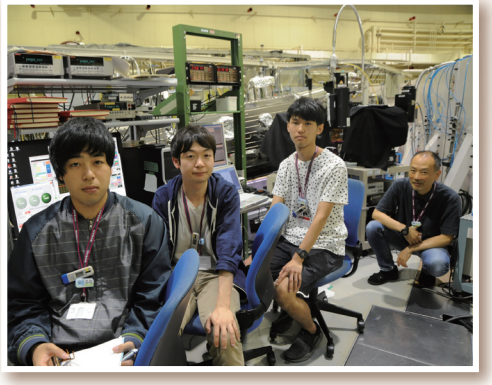

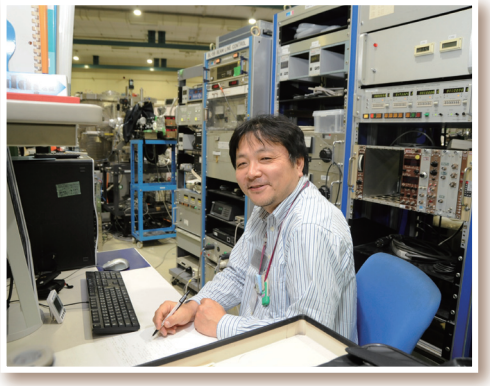

UVSOR User 3